University of Strathclyde
Department of Mechanical Engineering

Nonequilibrium boundary conditions for the Navier–Stokes–Fourier equations in hypersonic gas flow simulations

Nam Tuan Phuong Le

A thesis presented in fulfilment of the requirements
for the degree of Doctor of Philosophy

2010

Declaration of Author's Rights

This thesis is the result of the author's original research. It has been composed by the author and has not been previously submitted for examination which has led to the award of a degree.

Abstract

The simulation of nonequilibrium hypersonic gas flow is important for the aerodynamic design of space and re-entry vehicles. These flows are most successfully simulated by the Direct Simulation Monte Carlo method; however, the computational cost of this method is expensive in comparison to Computational Fluid Dynamics (CFD), which solves the Navier–Stokes–Fourier equations. This thesis investigates the slip/jump boundary conditions for use with the Navier–Stokes–Fourier equations applied to hypersonic aerodynamics. All slip/jump boundary conditions considered are implemented into a CFD solver in the OpenFOAM code for high speed viscous flows, named `rhoCentralFoam`. Simulations are carried out for sharp and blunt geometries, including the sharp-leading-edge flat plate, the sharp wedge, the circular cylinder and the blunt cone. The cases considered are studied for Mach number, Ma, ranging from 6 to 22, and for argon, nitrogen and air as working gases. In the present work, new slip/jump boundary conditions are proposed by inserting the Langmuir adsorption isotherm into the slip/jump Maxwell/Smoluchowski conditions. These new boundary conditions, the Maxwell/Smoluchowki conditions, and the second order slip/Smoluchowski conditions, are applied at the solid surfaces. The comparative results show that combining the Smoluchowski jump condition using a thermal accommodation coefficient $\sigma_T = 1.0$, a tangential momentum accommodation coefficient $\sigma_u = 0.7$ in the Maxwell slip condition, and the values of first-order $A_1 = 1.5$ and second-order $A_2 = 1.0$ coefficients in the second order slip condition, give a good prediction for the surface pressure distribution. Moreover, the new boundary conditions give better predictions for the surface pressures, compared with experimental data and the DSMC data published in the literature. This comprehensive and comparative investigation may lead to more accurate boundary conditions and subsequent aerodynamic drag predicitions for the design of future space vehicles.

Acknowledgements

I would like to express my gratitude to my supervisor Prof. Jason M. Reese and Dr. Christopher J. Greenshields for their support and guidance throughout this work.

I am indebted to Prof. Neville T. Baker for his proofreading and precious discussions.

Thanks are also due to Mr. Craig White for his helpful DSMC data in this thesis.

I would like to thank the Trustees of the James Weir Foundation for their financial support of this work through a James Weir Postgraduate Scholarship.

I would also like to thank the University of Strathclyde for financial support during my Ph.D programme through a University of Strathclyde Research Scholarship .

Contents

List of Figures

List of Tables

Nomenclature

Greek symbols

α	Fraction of occupied surface sites
β	An equilibrium constant
$\boldsymbol{\nabla}$	Gradient
$\boldsymbol{\tau}$	Shear stress tensor
ϵ	Gas density ratio across a normal shock
η	Number density of molecules
Γ	Diffusion coefficient
γ	Ratio of specific heats
Γ_n	Total number of molecules impinging on the surface
λ	Gas molecular mean free path
μ	Dynamic viscosity
ω	Temperature exponent
ω_f	Diffusive volumetric fluxes
ϕ	Variable (e.g. velocity or temperature)
ϕ_f	Volumetric flux
Φ_L	Limited value
Π	Stress tensor at the surface
ρ	Density
σ	Fraction coefficient
σ_T	Thermal accommodation coefficient

σ_u Tangential momentum accommodation coefficient

$\sum_{\mathrm{f}}$ Summation over cell faces

Θ Characteristic vibrational temperature

θ Weighting coefficient

$\boldsymbol{\Psi}$ General dependent tensor field

$\boldsymbol{\Psi}_{\mathrm{f}}$ General dependent tensor field at cell faces

$\boldsymbol{\Psi}_{\mathrm{P}}$ General dependent tensor field at cell centres

$\psi_{\mathrm{f}+}$ Volumetric fluxes in outward direction

$\psi_{\mathrm{f}-}$ Volumetric fluxes in inward direction

Latin symbols

$\bar{v}$ Mean molecular velocity

$\mathbf{I}$ Identity tensor

$\mathbf{n}$ Normal vector

$\mathbf{Q}$ Heat flux vector along the surface

$\mathbf{S}$ Transformation tensor

$\langle \mathbf{u} \rangle$ Bulk velocity

$\mathbf{u}$ Velocity

$\boldsymbol{q}$ Diffusive flux of heat

$\mathbf{d}$ Vector connecting the centroid of the owner cell to that of neighbouring cell

$\mathbf{F}$ Body force

$\mathbf{u}'$ Random velocity

A Area

a a coefficient specific to each boundary condition

A_1 Slip coefficient for the first order term

A_2 Slip coefficient for the second order term

a_i Coefficient

A_m	Mean area of a site
A_P	Constant of proportionality
A_S	Constant for Sutherland's law.
c	Speed of sound
$C(f)$	Collision integral term
c_p	Constant pressure specific heat
c_v	Constant volume specific heat
$c_{\mathrm{f}\pm}$	Speed of sound of the gas at the face in the outward and the inward direction
d	Molecular diameter
D_e	Heat of adsorption
E	Total energy
e	Internal energy
$f(\mathbf{r}, \mathbf{u}, t)$	Function of the position $\mathbf{r}$ and velocity $\mathbf{u}$ at time t
$f+$	Outward direction
$f-$	Inward direction
k	Thermal conductivity
k_B	Boltzmann's constant
K_L	A chemical equilibrium constant
Kn	Knudsen number
L	Characteristic length
l_c	Length of grading cells
M	Chemical name of the free gas molecules
m	Mass of a real molecule
Ma	Mach number
N	Number of DSMC molecules
N_A	Avogadro number

n_c	Number of grading cells
N_m	Number of molecules
P	Cell centroid
p	Pressure
p_{tw}	Pitot pressure
Pr	Prandtl number
Q	Molecular quantity
q	Heat flux
R	Specific gas constant
r	Ratio of successive gradients
R_c	Ratio of thickness between the last and first cells
r_c	Ratio of thickness between the one cell and the next
R_u	Universal gas constant
S	Cell surface
s	Exponent
S_v	A vacant surface
SM	An occupied surface
T	Gas temperature
T_S	Constant temperature
u_n	Velocity normal to the surface
u_p	Velocity parallel to the surface
u_s	Slip velocity
V	Cell volume
V_g	Fraction of gas components in volume
$\mathbf{\Delta}(Q)$	Moment of the collision integral terms
$\mathbf{S}_f$	Vector normal to the face surface

Super and Subscripts

0	Stagnation quantity
∞	Freestream condition
tr	Trace
T	Transpose
Cov	Covalent
j	Jump
ref	Reference
rot	Rotational
tra	Translational
vib	Vibrational
w	Surface

Chapter 1

Introduction and motivation

1.1 Introduction

On Thursday, 24 February 1949, the V-2/WAC multi-stage rocket was successfully launched in the United States with a velocity faster than five times the speed of sound (i.e. Mach number $Ma \geq 5$). It became the first object of human origin to achieve hypersonic flight [1]. Nowadays, hypersonic flight vehicles are used for both civilian and military applications, including both reconnaissance and surveillance. NASA is currently designing a new generation of space shuttles, known as hypersonic vehicles, to replace the earlier space shuttles [2].

The design of hypersonic vehicles requires accurate prediction of the surface properties in flight. These quantities are typically the surface temperature, the surface pressure and the shear stress. The surface pressure and the skin friction forces acting on the surface of the hypersonic vehicles are integrated to calculate the aerodynamic forces and the moment as lift, drag and pitching moments [3]. The peak surface temperatures or heat fluxes are integrated over time and mapped over the vehicle surface as part of the process to design the thermal protection system.

Hypersonic aerodynamics (or hypersonic gas flow) is different from the more conventional regimes of supersonic aerodynamics. This means the shape of hypersonic vehicles is different from the shape of supersonic vehicles. Vehicles flown at hypersonic speeds will be affected by high temperature gas [1]. This strongly influences the heat energy flux and the forces acting on the surface, such as the

pressure and the skin friction. Hypersonic gas flows are usually characterized by strong shocks, and both equilibrium and nonequilibrium gas chemistry [3].

Hypersonic vehicles will experience different gas flow regimes in the earth's atmosphere, because the gas density varies as a function of altitude. The vehicles will travel from a very rarefied atmosphere to a denser atmosphere i.e. from the free molecular regime, where individual molecule impacts on the surface are important, to the transition regime, where slip effects are important, and then to the continuum fluid regime [1]. At low altitudes, the gas density is relatively high in the aerodynamic flow around hypersonic vehicles. The basic parameter governing these different flow regimes is the *Knudsen number*, defined as the ratio of gas mean free path (i.e. the average distance a molecule moves between successive intermolecular collisions) to a characteristic length of the vehicle body.

The typical methods used to simulate hypersonic gas flows are the Direct Simulation MonteCarlo (DSMC) method and Computational Fluid Dynamics (CFD). The DSMC method has successfully simulated hypersonic gas flows in all the different regimes, but the computational effort is quite expensive. The CFD method, which solves the Navier-Stokes-Fourier equations with appropriate surface boundary conditions, may simulate successfully a hypersonic gas flow in the continuum regime, up to a Knudsen number of 0.1. The computational effort of CFD is much less than the DSMC method, especially for three dimensional flows.

This thesis will focus on the surface boundary conditions for the CFD method using the N–S–F equations, and low-enthalpy flows where chemical nonequilibrium is not important. The accuracy of the N–S–F simulations depends on that of the surface boundary conditions, and also the constitutive relations supplied, such as the viscosity-temperature relation, thermal conductivity and heat capacity. In the CFD method, it is not able that a computational mesh and a level of convergence which result in accurate surface pressure and shear stress values, does not necessarily guarantee accurate surface temperature and heat transfer values at the same time [4].

1.2 Survey of surface boundary conditions in rarefied gas flows

In this section, some research reported in references [5–13, 15–17] concerning slip velocity and temperature jump boundary conditions are reviewed. Their advantages and disadvantages are briefly discussed.

The first-order conventional slip condition was developed by Maxwell in 1890 for a flat plate, based on his earlier work on the theory of viscosity in gases [5]. Although it is not perfect, it is still the simplest and most useful description of the slip condition that we have. It is designed to work with the continuum governing equations in the CFD method, such as the N–S–F equations. The Maxwell slip condition is a simple form and is expressed by the normal gradient of velocity at the surface and a thermal creep term. The other first-order slip condition described by Shen *et al.* [12], was derived using the Chapman-Enskog solution of the Boltzmann equation under the relaxation time approximation (the Krook equation described in reference [14]). In this condition the slip velocity depends not only on the velocity gradient in the surface-normal direction but also on the pressure gradient in the flow direction. Moreover, a general slip condition for a solid surface in rarefied multi-component gas flows, reported by Zade *et al.* [11], was developed using the kinetic theory of gases. It can be simplified for particular problems, such as a single-component gas flow. An alternative slip condition developed by Gökçen *et al.* [7] aims a) to reduce to the classical Maxwell slip conditions as the continuum limit is approached, and b) yield the correct shear stress of free molecule flow in the limiting case of very large Knudsen numbers. In all these first-order slip conditions mentioned above, the accuracy of the simulation results is decided by a free parameter in the slip equation, namely the tangential momentum accommodation coefficient, which varies from 0 to 1.0. The tangential momentum accommodation, σ_u, determines the proportion of molecules reflected from the surface specularly $(1 - \sigma_u)$ or diffusely σ_u.

Second-order slip boundary conditions were developed for a planar surface [8, 15–17]. They include an additional second-order term of normal gradient of velocity. A similar problem to that of the first-order slip conditions is that the free coefficients of the first-order and second-order terms are still the subject of much discussion. The Maxwell–Burnett slip condition, reported by Lockerby *et*

al. [8], was proposed as a higher order boundary condition based on the conventional Maxwell equation and the constitutive relations derived by Burnett. This condition is formally second-order in space and stable in its solution. The Maxwell–Burnett slip condition gives good agreement for Poiseuille flow, and can also predict Sone's thermal stress slip flow, which cannot be captured by the conventional Maxwell slip condition [8]. In the Maxwell–Burnett slip condition, the free coefficient of the second order term depends on the Prandtl number of the gas.

The temperature jump condition was an early development by Smoluchowski [6], and was driven by the heat flux to the surface in the normal direction. A general temperature jump condition for rarefied multi-component gas flows is described by Zade *et al.* [11], based on the kinetic theory of gases, and can be simplified according to a particular problem such as a single-component gas flow. Gökçen *et al.* proposed a temperature jump condition a) to simplify the Smoluchowski jump condition, and b) to yield the correct heat transfer of free molecule flow in the limiting case of very large Knudsen numbers [7]. All these temperature jump conditions also depend on a free parameter, namely the thermal accommodation coefficient, which varies from 0 to 1.0, and decides the accuracy of the simulation results. The thermal accommodation coefficient is used to ascribe the temperatures of the receding molecules. Specularly reflected molecules recede from the surface with their original incident energy, and diffusely reflected molecules have their energies adjusted to those would arise in a mass of gas in equilibrium at the temperature of the surface.

Alternative slip velocity and temperature jump conditions which overcome the problem of free parameters in the conditions presented above were proposed by Myong and co-workers [9, 10]. These are the "Langmuir conditions" developed based on the Langmuir adsorption isotherm, and give good results for some microflow rarefied gas flows. However, the problem in applying these conditions is the choice of reference values of either the velocity or the temperature, depending on the particular case being considered. The reference values might be evaluated either a mean free path away from the surface or in the freestream.

In addition, the reader can refer to other slip velocity and temperature jump boundary conditions, which were developed for a) the higher order governing Burnett equations [18, 20], b) the Grad moment equations [19], and c) the Boltz-

mann governing equation [21].

1.3 Motivation and scope of the present work

In preliminary work it was found that applying the surface boundary conditions in solving the N-S-F equations gives rise to some problems that may have a major affect the accuracy of the simulation results. Considering the surface boundary conditions described above, the problems are a) the desired values of the free parameters of tangential momentum accommodation coefficient, thermal accommodation coefficient and the free coefficients in the second-order slip condition, and b) the reference values to be used in the Langmuir boundary conditions.

Comparing the Langmuir conditions with the Maxwell/Smoluchowski boundary conditions, it is seen that a) the adsorption of gas on a solid surface is ignored in developing the Maxwell/Smoluchowski boundary conditions, which is considered as a kind of diffuse reflection [22, 23], and b) the Langmuir boundary conditions only consider the adsorption of gas on to a solid surface, resulting in the choice of the reference values in the equations, while they lack the kinetic theory developed in the Maxwell/Smoluchowski conditions. For sharp-leading-edge geometries, surface boundary conditions in the CFD method are expected to agree reasonably well with experimental data, and to capture the increased nonequilibrium behaviour near the leading edge.

The scope of this thesis, which addresses the problems described above, is set out in detail below.

1. The tangential momentum accommodation coefficient and thermal accommodation coefficient of the Maxwell/Smoluchowski boundary conditions are numerically investigated to find good agreement with experimental data and independent DSMC data.

2. The Langmuir boundary conditions developed by Myong and co-workers [9, 10] are tested for the sharp-leading-edge flat plate case to assess their performance.

3. The free coefficients of the second order slip condition developed for a pla-

nar surface are investigated to find reasonable agreement with experimental and DSMC data. The results obtained are compared with the results of the conventional Maxwell slip condition to ascertain whether or not the second order slip condition is better than the conventional Maxwell slip condition in simulating hypersonic gas flows using the N–S–F equations.

4. New boundary conditions are proposed by inserting the Langmuir adsorption isotherm into the Maxwell/Smoluchowski condition equations, with the aim of achieving a more realistic physical model. The new boundary conditions address the lack of the adsorption of gas with in the Maxwell/Smoluchowski boundary conditions and the problem of the reference values required by the Langmuir boundary conditions. Due to high nonequilibrium conditions near leading edges, the new boundary conditions are expected to give good agreement with the experimental data for sharp-leading-edge geometries.

1.4 Outline of the thesis

Chapter 2 Background and theory for simulating hypersonic gas flow are introduced as a) a summary of kinetic theory of gases, b) various governing equations modelled hypersonic gas flows, and c) different simulation methods. The advantages and disadvantages of the two latter ones are briefly discussed. The viscosity–temperature relations used for all subsequent simulations are also presented in this chapter.

Chapter 3 Common boundary conditions are reviewed. They are a) the Maxwell/ Smoluchowski conditions, b) the second order slip condition, and c) the Langmuir conditions. The Langmuir conditions are tested for a laminar sharp-leading-edge flat plate case to assess their performance. New boundary conditions, named the "Langmuir–Maxwell" slip condition and the "Langmuir–Smoluchowski" jump condition, are proposed. The implementation numerically of slip/jump conditions into the OpenFOAM CFD solver is also presented.

Chapter 4 The surface boundary conditions presented in Chapter 2 are tested and validated for laminar sharp-leading-edge flat plate cases. Tests are done with different working gases, such as argon, nitrogen and air. The free parameters of the Maxwell/Smoluchowski conditions and the second-order slip condition are

numerically investigated to find their proper values in simulating hypersonic gas flows. The performance of the second-order slip condition is compared with that of the conventional Maxwell slip condition. The new boundary conditions are validated, and no-slip/jump tests are also carried out for the flat plate cases.

Chapter 5 This chapter records the results of simulations of rarefied hypersonic cross-flow past a circular cylinder. The desired values of the free parameters of the Maxwell/Smoluchowski conditions obtained in the previous chapter are tested for this case. The new boundary conditions also are validated for circular cylindrical geometries. The curvature effect of the slip conditions is investigated for the cylinder case, as well as no slip/jump tests.

Chapter 6 This chapter has the same structure as Chapter 5. Simulations of hypersonic gas flows about a wedge and a blunt cone are presented. The Maxwell/Smoluchowski conditions with the desired values of free parameters and the new boundary conditions are tested. The curvature effect of slip conditions and the no slip/jump tests also are also investigated for the wedge and the blunt cone cases. An analysis of the relative effect of thermal creep on satellite-on-a-chip is presented by an analytical solution.

Chapter 7 Conclusions from this work on the surface boundary conditions in simulating hypersonic gas flows. The contribution to the advancement of knowledge made by this work is presented and the future work suggested.

1.5 Presentations

The results of the present work were presented at 1) the Research Presentation Day, the University of Strathclyde, 2009, 2) the 3rd EUropean Conference AeroSpace Sciences (EUCASS), France, 2009, 3) The 22nd Scottish Fluid Mechanics Meeting, Scotland, 2009, and 4) the Research Presentation Day, the University of Strathclyde, 2010. The results were also published in the Proceedings of the 3rd EUropean Conference for AeroSpace Sciences, EUCASS2009-86, 2009.

Chapter 2

Simulation of hypersonic gas flows: Background and Theory

2.1 Introduction

The computational simulation of nonequilibrium hypersonic gas flows requires a knowledge of the kinetic theory of gases and an understanding of different simulation methods. This chapter will outline the concepts of equilibrium and nonequilibrium gas flows, and the Knudsen number, Kn, that characterizes the regimes of nonequilibrium flows. A basic brief summary of the kinetic theory of gases is presented, including the velocity, internal energy, the velocity distribution function and collision models. Various governing equations for nonequilibrium gas flows are also presented such as: the Boltzmann equation, the Chapman–Enskog expansion (producing the Euler equations, the Navier–Stokes–Fourier (N–S–F) equations and the Burnett equations), and the moment equations. Three simulation methods, the Direct Simulation Monte-Carlo (DSMC), Computational Fluid Dynamics (CFD), and the CFD-DSMC hybrid method are outlined. Hypersonic gas flows are most successfully simulated through DSMC, however the computational time is much longer than when using CFD, which solves the N–S–F equations. The viscosity–temperature relations used for all simulations in this thesis are also presented in this chapter.

2.2 Equilibrium and nonequilibrium gas flows

A gas in equilibrium will not change its molecular properties in time and space. This means that there are no gradients in the macroscopic properties such as velocity, temperature and mass density. A gas in equilibrium will also have a Maxwellian velocity distribution, f_0 [24, 25]:

$$f_0 = \left(\frac{m}{2\pi k_B T}\right)^{3/2} \exp\left[-\frac{m\mathbf{u}^2}{2k_B T}\right], \tag{2.1}$$

where m is the mass of a real molecule, k_B is Boltzmann's constant, T is the gas temperature and $\mathbf{u}$ is the molecular velocity.

In contrast, a gas in nonequilibrium will have strong gradients in the macroscopic properties. In hypersonic gas flows, the main causes of significant nonequilibrium may be high velocities, high temperatures and the low gas density. A velocity gradient in a viscous fluid will cause a transfer of momentum; a temperature gradient will transport heat energy. For a diatomic gas, thermal non-equilibrium occurs in internal energy modes, such as rotational and vibrational energy modes [1]. The transfer of momentum and energy is due to translational nonequilibrium and appears as the effect of viscosity and thermal conductivity. Mass transport is driven by species concentration gradients, but this is neglected for the simple single species gases studied here.

Translational nonequilibrium of a rarefied gas flow can be characterized by the Knudsen number, Kn, that is the ratio of the molecular mean free path, λ, to either the macroscopic characteristic length, L, or the length scale of a macroscopic gradient, $\phi/|d\phi/dl|$, of the flow:

$$Kn = \frac{\lambda}{L} \cong \frac{\lambda}{\phi}\left|\frac{d\phi}{dl}\right|, \tag{2.2}$$

where l represents a suitable spatial domain direction and ϕ is a quantity of interest, such as the gas density, pressure, velocity or temperature.

At low altitudes, the gas density is relatively high and Kn is small, and gas flows

[1] Chemical nonequilibrium will, however, not be presented in this thesis

may be simulated by solving the Euler ($Kn \leq 0.001$) or the N–S–F equations with no-slip boundary conditions ($0.001 \leq Kn \leq 0.01$). At high altitudes, the gas density is lower and the gas is rarefied. The mean free path, λ, is large resulting in Kn being large and the nonequilibrium behaviour being appreciable. There are fewer collisions between molecules in the flow around air vehicles. The lack of collisions means the N–S–F equations become inappropriate in rarefied regimes indicated by a large Knudsen number. An approach to improve the N–S–F equations in the range of $0.01 \leq Kn \leq 0.1$ is to use velocity slip and temperature jump boundary conditions. When Kn rises into the range $0.1 \leq Kn \leq 1$, this is called the transition-continuum regime: the N–S–F equations become inappropriate because the near-equilibrium fluid assumption for flows has broken down. A schematic of these regimes, and their solution methods, is shown in Figure 2.1.

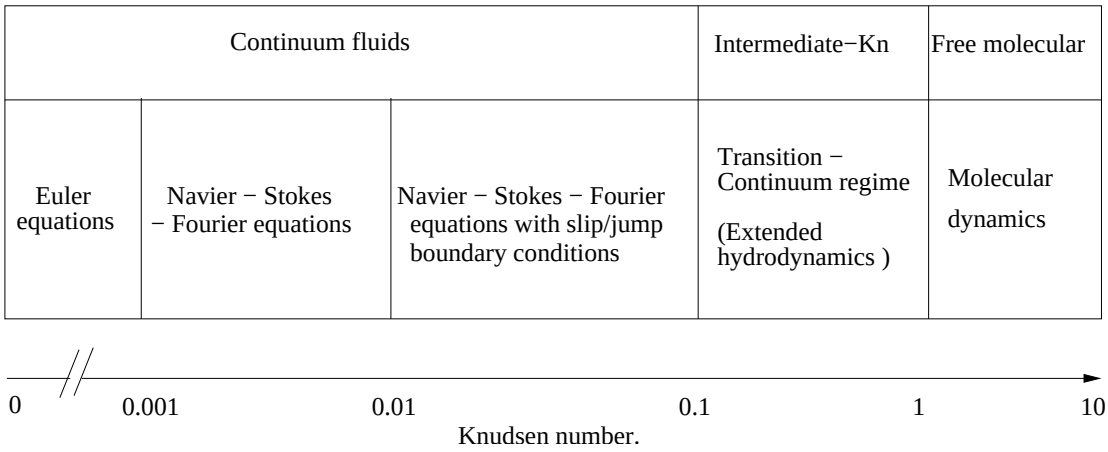

Figure 2.1: Schematic of flow regimes and fluid simulation models over the range of Knudsen numbers.

2.3 Kinetic theory of gases

In this section, a brief summary of relevant parts of the kinetic theory of gases is presented, with consideration for monatomic gases (such as argon) and diatomic gases (such as nitrogen). For more details of other gases, the reader is refered to the literature [24, 25].

In kinetic theory, a gas flow is considered on the molecular level and the molecules

are assumed to be very small relative to their spacing. The individual gas molecules (or particles) are considered to be in constant random motion, with binary collisions with other molecules and surfaces.

The individual molecules have physical properties, such as mass and energy, and these properties are assumed to depend essentially on the motion of molecules and not on the internal structure [22]. The individual molecule velocity, $\mathbf{u}$, can be divided into two components: random and average velocities, as follows [24, 26]:

$$\mathbf{u}^{'} = |\mathbf{u} - \langle \mathbf{u} \rangle|, \tag{2.3}$$

where $\mathbf{u}$' is the random velocity of the molecules, known as the thermal velocity, and $\langle \mathbf{u} \rangle$ is the average velocity of the molecules in the considered volume, known as the bulk velocity.

Each molecule can have several energy modes, such as a) translational energy, which is described by the random motion of molecules, b) rotational energy, due to the rotation of the atoms around an axis, and c) vibrational energy, due to the vibration of the atoms along the internuclear axis. Diatomic molecular gases consist of three energy modes while monatomic gases have only a translational energy mode.

The translational temperature (thermodynamic), T_{tra}, is a measure of the kinetic energy due to the random motion of gas molecules, and is computed as [24, 26]:

$$e_{tra} = \frac{1}{2} m \langle \mathbf{u} \rangle^2 = \frac{3}{2} k_B T_{tra}, \tag{2.4}$$

where e_{tra} is the average translational energy per molecule.

The rotational, T_{rot}, and vibrational, T_{vib}, temperatures are measures of the internal rotational and vibrational energy of a diatomic gas [24, 26]:

$$e_{rot} = k_B T_{rot}, \tag{2.5}$$

$$e_{vib} = \frac{k_B \Theta}{\exp(\Theta / T_{vib} - 1)}, \tag{2.6}$$

where e_{rot} and e_{vib} are the average rotational and vibrational energies per molecule, and Θ is the characteristic vibrational temperature.

The rotational and vibrational energy modes are activated through the processes of intermolecular collisions. At very low temperatures, the rotational and vibrational modes are frozen. By increasing the temperature they become excited at, e.g., above 4000K for nitrogen [1].

The velocity distribution function (VDF) is important in the kinetic theory of gases. The VDF is used for a probabilistic description of velocity and position of a single molecule. It is considered that there are N_m identical molecules in physical space. Each molecule can be represented by its velocity vector in space [26]. A volume element in velocity space is denoted by $d\mathbf{u}$. The VDF, $f(\mathbf{u})$, is then defined by [26]:

$$dN_m = N_m f(\mathbf{u})\, d\mathbf{u}, \tag{2.7}$$

where dN_m is the number of molecules.

The macroscopic properties presented by a molecular quantity, Q, can be obtained from this VDF. The relationship between the VDF and the average of any molecular quantity, Q, can be determined as given below [26].

The quantity, Q, is either a constant or a function of the molecular velocity and its average value is computed as:

$$\langle Q \rangle = \frac{1}{N_m} \int_{N_m} Q dN_m. \tag{2.8}$$

Substituting for dN_m from equation (2.7). The general relationship is obtained.

$$\langle Q \rangle = \int_{-\infty}^{\infty} Q f(\mathbf{u})\, d\mathbf{u}. \tag{2.9}$$

The collision or interaction of two or more molecules requires the orientation of

the individual molecules to be known. There are different models for these to analyze the collision mechanics. Two common models presented here are the Hard Sphere (HS) model, and the Variable Hard Sphere (VHS) model. The HS model assumes each gas molecule to be a perfectly elastic sphere with a fixed diameter, without any force acting on the molecules until two molecules come into contact. The HS model has the advantage of easily calculated collision mechanics because of the isotropic scattering in the centre of mass frame [26]. The disadvantage of the HS model is the fixed total collision cross-section. Experimental observations show that the total collision cross-section is dependent on the relative velocity between the molecules involved in the collisions. The relative velocity is dependent on temperature, so there is a temperature dependence on the collision cross-section and on the molecular diameter. It is important to reproduce this behavior to successfully model the temperature dependence of viscosity [26]. To overcome this problem, the VHS model is proposed with a molecular diameter that is a function of the relative velocity. The VHS model for a particular gas may be defined by the effective diameter of the molecule at a particular reference temperature. In the VHS model, the inverse power law model, with the total cross-section inversely proportional to the relative velocity, is chosen to match the experimental viscosity data [26].

The reader can refer to the literature for other collision models, such as the Variable Soft Sphere (VSS) model, the generalized hard sphere model and the Maxwell model given in reference [26].

2.4 The governing equations of gas flows

This section describes a summary of the various governing equations, which are used to model nonequilibrium gas flows. The advantages and disadvantages of each equation are briefly discussed.

2.4.1 The Boltzmann equation

The Boltzmann equation uses classical mechanics to describe velocity, position and state of a gas molecule in a flow at any given time [24] as:

$$\frac{\partial f}{\partial t} + \mathbf{u} \cdot \frac{\partial f}{\partial \mathbf{r}} + \mathbf{F} \cdot \frac{\partial f}{\partial \mathbf{u}} = C\left(f\right), \tag{2.10}$$

where the function $f(\mathbf{r}, \mathbf{u}, t)$ describes the number density of gas molecules with position $\mathbf{r}$ and velocity $\mathbf{u}$ at a certain time t under influence of a body force $\mathbf{F}$. The term $C(f)$ describes binary collisions.

The Boltzmann equation is valid for all regimes of a gas flow from the continuum to the rarefied regime. However, it is derived with assuming binary collisions, that will limit its validity to dilute gases. The main challenge in using the Boltzmann equation for simulating gas flow is the collision integral term, $C(f)$. In solving the Boltzmann equation, the collision integral term can be replaced by a simplified kinetic model of the collision processes in the flow as in the Bhatnagar-Gross-Krook model [27]. The idea of this model is that modified collision terms are constructed so that each collision conserves particle number, momentum, and energy; other characteristics such as persistence of velocities and angular dependence may be included and lead to irreversible behavior [27]. Linearizing the Boltzmann equation using the kinetic models can give accurate solutions for some fundamental cases, but it is rarely appropriate for a complex geometry or flow system.

2.4.2 The Chapman–Enskog expansion

The Chapman–Enskog (C–E) expansion obtains nonequilibrium distribution functions, f, of gas molecules as a perturbation of the local Maxwellian distribution function, f_0, using a series expansion. The C–E expansion is written in terms of Kn [2] as:

$$f = f_0 \left(1 + a_1 \left(Kn\right) + a_2 \left(Kn^2\right) + ...\right), \tag{2.11}$$

where the coefficients a_i are functions of density, velocity and temperature. The most important success of the C–E expansion is that it allows for computation of transport coefficients for macroscopic laws from the microscopic details of the gas. This expansion shows that viscosity and heat conductivity depend only on temperature and not on density. The temperature dependence is linked to the interaction potential between the molecules [19].

The C–E expansion produces the Euler equations in zeroth-order of Kn, which are inviscid constitutive relations. It also produces the viscous N–S–F equations, the Burnett equations and the Super-Burnett equations in the first, the second

and the third order of Kn, respectively. The two latter models are also known as the "higher-order models" and include more complex constitutive expressions for stress and heat flux [28]. Unfortunately, the higher order equations are numerically unstable [19].

2.4.3 Moment equations

Moment equations (or equations of transfer) are obtained by multiplying the Boltzmann equation by a molecular moment quantity Q and are written [26] as:

$$\frac{\partial Q}{\partial t} + \frac{\partial \left(\mathbf{u}Q\right)}{\partial \mathbf{r}} + \mathbf{F} \cdot \frac{\partial Q}{\partial \mathbf{u}} = \mathbf{\Delta}\left(Q\right), \tag{2.12}$$

where $\mathbf{\Delta}(Q)$ is the moment of the collision integral terms.

When a complete set of moments is considered, that is, if the moments are based on a complete functional space, the description of the gas through moments is equivalent to the description through the phase density. [19]

From the general moment equation (2.12), if five moments are considered as the moments of density, three components of velocity and temperature then this method is equivalent to the Euler equations from the C–E expansion. If thirteen moments are considered as the moments of density, momentum density, energy density, stress and heat flux then we have Grad's 13 moment method. Grad's 26 moment method is derived from the 26 moments. These moment methods are numerically stable, but produce unphysical discontinuous shocks for high Mach numbers because of its hyperbolic structure. The discontinuity appears when the flow speed is above the fastest signal speed of the equations. For 13 moments this is at Ma = 1.65, but for higher moment number the critical velocity grows [19].

Struchtrup [19] combined Grad's 13 moment method with the C–E expansion to produce the Regularized 13 moment equations, which avoids the problem mentioned above of the Grad moment methods.

2.4.4 The Navier–Stokes–Fourier equations

The N–S–F equations can be derived from the C–E solution of the Boltzmann equation at first order in Kn. The N–S–F equations are typically used to describe gas flows in the continuum fluid regime. They are valid with no-slip boundary conditions in the range $0.001 \leq Kn \leq 0.01$, and valid with the slip and temperature jump boundary conditions in the range $0.01 \leq Kn \leq 0.1$. These equations, neglecting body forces, can be expressed [1] as:

Conservation of mass

$$\frac{\partial \rho}{\partial t} + \boldsymbol{\nabla} \cdot [\mathbf{u}\rho] = 0, \tag{2.13}$$

Conservation of momentum

$$\frac{\partial (\rho \mathbf{u})}{\partial t} + \boldsymbol{\nabla} \cdot [\mathbf{u} (\rho \mathbf{u})] + \boldsymbol{\nabla} p + \boldsymbol{\nabla} \cdot \boldsymbol{\tau} = 0, \tag{2.14}$$

Conservation of total energy

$$\frac{\partial (\rho E)}{\partial t} + \boldsymbol{\nabla} \cdot [\mathbf{u}(\rho E)] + \boldsymbol{\nabla} \cdot [\mathbf{u} p] + \boldsymbol{\nabla} \cdot (\boldsymbol{\tau} \cdot \mathbf{u}) + \boldsymbol{\nabla} \cdot \boldsymbol{q} = 0, \tag{2.15}$$

where ρ is the mass density; p is the pressure; the total energy $E = e + |\mathbf{u}^2| /2$, with e the internal energy per unit mass, which includes the translational, rotational and vibrational energy; $\boldsymbol{q}$ is the diffusive flux of heat; $\boldsymbol{\tau}$ is the shear stress tensor. For inviscid flows, $\boldsymbol{\tau} = 0$ and $\boldsymbol{q} = 0$, then equations (2.13, 2.14, 2.15) reduce to the Euler equations.

For viscous flows, the stress tensor can be represented by Newton's law [1]:

$$\boldsymbol{\tau} = -\mu \mathrm{dev} \left(\boldsymbol{\nabla} \mathbf{u} + (\boldsymbol{\nabla} \mathbf{u})^{\mathrm{T}} \right), \tag{2.16}$$

where μ is the dynamic viscosity, and the superscript T denotes the transpose.

The diffusive flux is represented by Fourier's law [1]:

$$\boldsymbol{q} = -k \boldsymbol{\nabla} T, \tag{2.17}$$

where k is the thermal conductivity. A calorically perfect gas is considered for all simulations in the present study, so $p = \rho RT$ and $e = c_v T = (\gamma - 1) RT$, where c_v is the constant volume specific heat; R is the specific gas constant and γ is the ratio of specific heats at constant pressure.

2.5 Simulation methods

In this section, simulation methods are described for modelling nonequilibrium gas flows, i.e. the Direct Simulation Monte Carlo method (DSMC), the Computational Fluid Dynamics method and the hybrid method.

2.5.1 The direct simulation Monte Carlo method

The DSMC method was originally proposed by Bird [26] and is a statistical approach. It is considered to be the most accurate method for the computation of rarefied gas flows in all regimes. The DSMC method is also regarded as a numerical method for solving the Boltzmann equation, rather than solving it directly [26]. Instead of simulating each real molecule in a gas flow, the DSMC method employs a large number of DSMC molecules to represent real gas behavior. Each DSMC molecule is assumed to be representative of a fixed number of real molecules and has a specific position, velocity and internal energy (including rotational and vibrational). The intermolecular collisions and molecule surface collisions are calculated using probabilistic theory. The collision models are commonly used in the DSMC method such as the HS model, the VHS model and the VSS model.

In the DSMC method, the physical space is divided initially into finite size cells that are populated by DSMC molecules. The number of DSMC molecules is much smaller than the number of real molecules. The DSMC molecules move with different microscopic velocities for a short time, and then DSMC molecules that reside in the same space cell are allowed to interact. For the interaction, molecule pairs are picked randomly, and then undergo collisions where the collision parameter is chosen from statistical models. After the collisions are performed, the molecules undergo the next short period of free flight with new velocities [19]. Surface collisions are taken into account through the surface boundary conditions presented in the next chapter. A typical DSMC flowchart is shown in Figure 2.2.

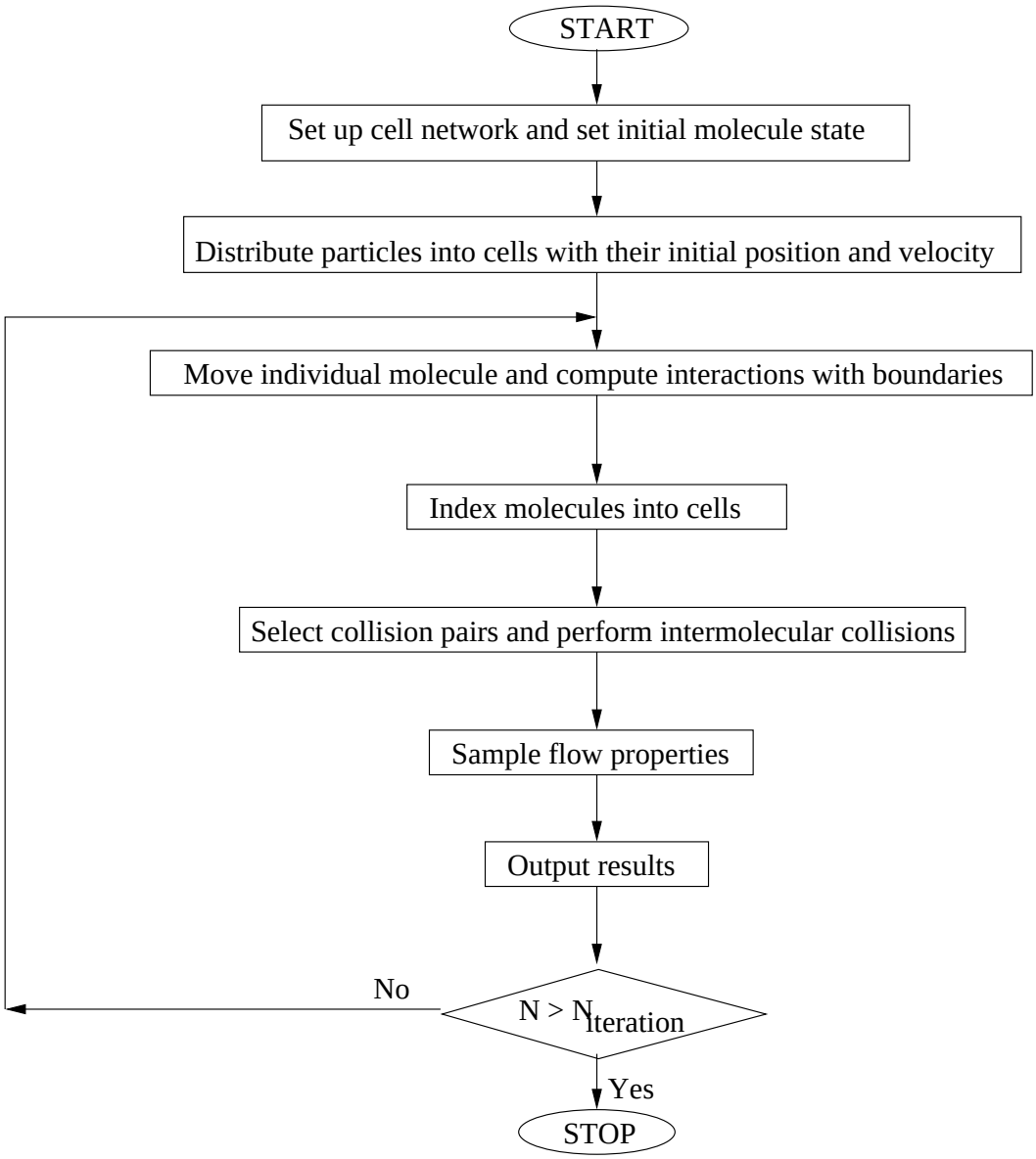

Figure 2.2: A typical DSMC flowchart [29]. N is the number of DSMC molecules.

The DSMC method is very powerful and can model complex nonequilibrium flows and chemical reactions. However, it has the limitations that a) the collisions are chosen based on the molecules in each cell, resulting in a cell size dependence on local mean free path, b) each cell needs to contain sufficient molecules in order to preserve collision statistics, and c) the time step must be chosen so that molecules only traverse a fraction of the average cell length per time step [29].

The DSMC method has two types of errors described as a) statistical errors due to the nature of the method, and b) a deterministic error, that depends on the selection of numerical parameters such as the time step, cell volume and the number of DSMC molecules. Increasing the latter will significantly reduce this error, but the computational time will increase. The computational effort of the DSMC method is expensive and requires greater computational facilities.

2.5.2 The computational fluid dynamics method

Typically, the governing equations solved by the CFD method are based on the assumptions that the fluid is a continuum, that the perfect gas law applies, and the only forces are due to pressure, viscous effects and body forces. It is possible for the CFD method to accurately predict the aerodynamic environment for conventional air vehicles (including surface pressures and forces), but is severely limited in accurately predicting the aerothermodynamic environment of hypersonic vehicles that have high-enthalpy flows, surface catalycity, jet/airflow interaction [3]. In the CFD method, the governing equations are often numerically solved by the finite volume (FV) method. A variety of numerical algorithms have also been developed to deal with the shocks at hypersonic velocity.

In this thesis, the N–S–F equations are numerically solved with the high-resolution central scheme described by Greenshields *et al.* [30]. The results in [30] indicate that this central scheme is competitive with the best method previously published, and is simple and well-suited to a collocated, polyhedral FV framework. The FV discretisation and this central scheme are described in [30] and the most important aspects outlined below.

The FV method discretizes the differential equations in the N–S–F equations, on meshes containing polyhedral cells with an arbitrary number of faces, each with an arbitrary number of vertices. The spatial domain is therefore divided into a number of control volumes, or cells. There is no alignment of the mesh with the co-ordinate system and the number of neighbouring cells can vary from cell to cell. The cell connectivity is that a cell face is either internal and intersects two cells only or comprises an external boundary and belongs to a single cell only. Each face is assigned by an owner cell and a neighbour cell. The face area vector $\mathbf{S}_f$ is a vector normal to the face surface pointing out of the owner cell, whose

magnitude is that of the area of the face, as seen in Figure 2.3. In this collocated system, all dependent variables and the material properties are stored at each cell centroid, 'P' in Figure 2.3. The vector $\mathbf{d}$ connects the centroid of the owner cell P to that of the neighbouring cell N, and the vector $\mathbf{d}_{fN}$ connects the centre of the face to the centroid of the cell N [30].

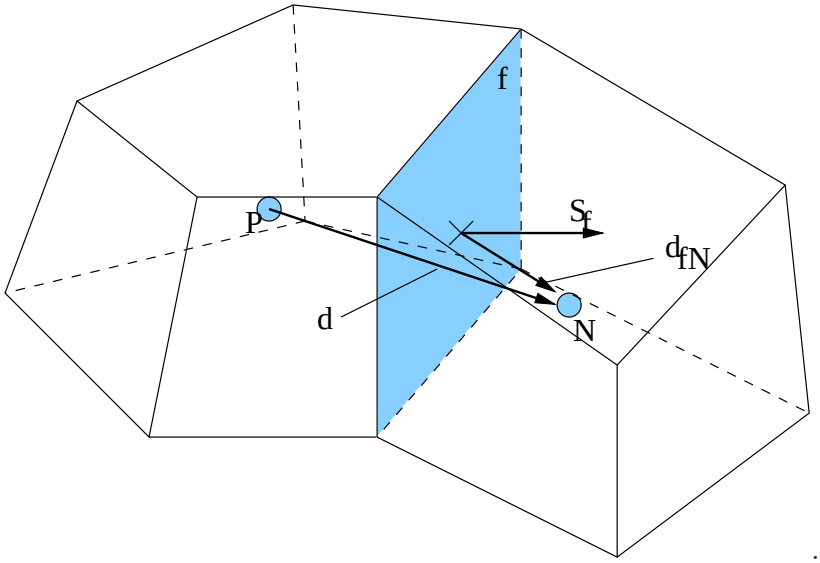

Figure 2.3: Finite volume discretisation [30].

The FV method solves the flow differential equations within an integral over a fixed cell volume V. Divergence and gradient terms are then converted to integrals over the cell surface S using a generalised form of Gauss's theorem. The integration requires fluxes at cell faces, evaluated by interpolation of cell centre values to the faces. For polyhedra with an arbitrary number of faces, it is desirable that the interpolation to a given face is between owner and neighbour cells only, otherwise it becomes complex. The second order semi-discrete, non-staggered schemes of Kurganov and Tadmor (KT) [31] and Kurganov, Noelle and Petrova (KNP) [32] permit this. Below, we outline discretisation of a general dependent tensor field $\mathbf{\Psi}$ of any rank by interpolating the values $\mathbf{\Psi}_\mathrm{P}$ at cell centres to values $\mathbf{\Psi}_\mathrm{f}$ interpolated to cell faces [30].

The *convective terms* in equations (2.13, 2.14, 2.15) i.e. $\nabla\cdot\left[\mathbf{u}\rho\right], \nabla\cdot\left[\mathbf{u}\left(\rho\mathbf{u}\right)\right]$, $\nabla\cdot\left[\mathbf{u}\left(\rho E\right)\right]$, and $\nabla\cdot\left[\mathbf{u}p\right]$ are treated as a critical aspect of central schemes. Each

is integrated over a control volume and linearized as follows [30]:

$$\int_V \boldsymbol{\nabla}\cdot[\mathbf{u}\boldsymbol{\Psi}]\,dV = \int_S dS\cdot[\mathbf{u}\boldsymbol{\Psi}] \approx \sum_{\mathrm{f}} \mathbf{S}_{\mathrm{f}}\cdot\mathbf{u}_{\mathrm{f}}\boldsymbol{\Psi}_{\mathrm{f}} = \sum_{\mathrm{f}} \phi_{\mathrm{f}}\boldsymbol{\Psi}_{\mathrm{f}}, \tag{2.18}$$

where $\sum_{\mathrm{f}}$ denotes a summation over cell faces and $\phi_{\mathrm{f}} = \mathbf{S}_{\mathrm{f}}\cdot\mathbf{u}_{\mathrm{f}}$ is the volumetric flux (i.e. the volume of fluid flowing through the face per second).

For compressible flows, fluid properties are not only transported by the flow but also by the propagation of waves. This requires the flux interpolation to be stabilized, based on transport that can occur in any direction. The KT and KNP methods are applied to do this in their original form. The interpolation procedure is divided into directions corresponding to flow outward and inward of the face owner cell. These directions are denoted as f+, coinciding with the direction $+S_{\mathrm{f}}$ and f– coinciding with $-S_{\mathrm{f}}$. The discretisation is then as follows [30]:

$$\sum_{\mathrm{f}} \phi_{\mathrm{f}}\boldsymbol{\Psi}_{\mathrm{f}} = \sum_{\mathrm{f}} \left[\theta\phi_{\mathrm{f}+}\boldsymbol{\Psi}_{\mathrm{f}+} + (1-\theta)\,\phi_{\mathrm{f}-}\boldsymbol{\Psi}_{\mathrm{f}-} + \omega_{\mathrm{f}}\left(\boldsymbol{\Psi}_{\mathrm{f}-} - \boldsymbol{\Psi}_{\mathrm{f}+}\right)\right], \tag{2.19}$$

The first two terms on the right hand side of equation (2.19) are flux evaluations in the f+ and f– directions, respectively. The third term is strictly only required in cases where the convection term is part of a substantive derivative, $\nabla\cdot[\mathbf{u}\,(\rho\mathbf{u})]$ in equation (2.14), for which $\partial(\rho\mathbf{u})/\partial t$ completes the substantive derivative of $\rho\mathbf{u}$. It is an additional diffusion term using a volumetric flux ω_{f} based on the maximum speed of propagation of any discontinuity that may exist at a face between values interpolated in the f+ and f– directions [30].

In the KT method, the f+ and f– contributions are weighted equally so that the weighting coefficient $\theta = 0.5$, hence its description as a *central* scheme. The KNP method calculates θ based on one-side local speeds of propagation. The weighting is then biased in the upwind direction, hence these schemes are called *central-upwind*. Volumetric fluxes associated with local speeds of propagation can be calculated as follows [30]:

$$\begin{aligned} \psi_{\mathrm{f}+} &= \max\left(c_{\mathrm{f}+}\left|\mathbf{S}_{\mathrm{f}}\right| + \phi_{\mathrm{f}+}, c_{\mathrm{f}-}\left|\mathbf{S}_{\mathrm{f}}\right| + \phi_{\mathrm{f}-}, 0\right); \\ \psi_{\mathrm{f}-} &= \max\left(c_{\mathrm{f}+}\left|\mathbf{S}_{\mathrm{f}}\right| - \phi_{\mathrm{f}+}, c_{\mathrm{f}-}\left|\mathbf{S}_{\mathrm{f}}\right| - \phi_{\mathrm{f}-}, 0\right). \end{aligned} \tag{2.20}$$

Here, $c_{\mathrm{f}\pm} = \sqrt{\gamma R T_{\mathrm{f}\pm}}$ are the speeds of sound of the gas at the face, outward and inward of the owner cell. The weighting factor is:

$$\theta = \begin{cases} \frac{1}{2} & \text{for the KT method;} \\ \frac{\psi_{\mathrm{f}+}}{\psi_{\mathrm{f}+} + \psi_{\mathrm{f}-}} & \text{for the KNP method.} \end{cases} \tag{2.21}$$

The diffusive volumetric flux is calculated according to:

$$\omega_{\mathrm{f}} = \begin{cases} \theta \max\left(\psi_{\mathrm{f}+}, \psi_{\mathrm{f}-}\right) & \text{for the KT method;} \\ \theta\left(1-\theta\right)\left(\psi_{\mathrm{f}+} + \psi_{\mathrm{f}-}\right) & \text{for the KNP method.} \end{cases} \tag{2.22}$$

The method involves f+ and f– face interpolations of a number of variables $(T, \rho, ...)$ from values at neighbouring cell centres. The interpolation procedure uses a limiter to switch between low and high order schemes based on a flux limiter function $\vartheta(r)$, where r represents the ratio of successive gradients of the interpolated variable, constrained to $r \geq 0$. On a polyhedral mesh, r can be described as follows for the f+ direction [30]:

$$r = 2\frac{\mathbf{d} \cdot \left(\boldsymbol{\nabla}\boldsymbol{\Psi}\right)_{\mathrm{P}}}{\left(\boldsymbol{\nabla}_{\boldsymbol{d}}\boldsymbol{\Psi}\right)_{\mathrm{f}}} - 1, \left(\text{ scalar } \boldsymbol{\Psi}\right), \tag{2.23}$$

where $\left(\boldsymbol{\nabla}\boldsymbol{\Psi}\right)_{\mathrm{P}}$ is the full gradient calculated at the owner cell P with linear interpolation and $\left(\boldsymbol{\nabla}_{\boldsymbol{d}}\boldsymbol{\Psi}\right)_{\mathrm{f}} = \boldsymbol{\Psi}_{\mathrm{N}} - \boldsymbol{\Psi}_{\mathrm{P}}$ is the gradient component normal to the face, scaled by $|\mathbf{d}|$.

The f+ and f– interpolation are based on limiting standard first order upwind and second order linear interpolations. The chosen limiters are total variation diminishing and symmetric, for which $\vartheta(r)/r = \vartheta(1/r)$, namely Minmod [33] and van Leer [34], whose limiter functions are $\vartheta(r) = \max[0, \min(1, r)]$ and $\vartheta(r) = (r + |r|)/(1 + r)$, respectively. Then, the f+ interpolation of $\boldsymbol{\Psi}$ is simply computed as [30]:

$$\boldsymbol{\Psi}_{\mathrm{f}+} = \left(1 - g_{\mathrm{f}+}\right)\boldsymbol{\Psi}_{\mathrm{P}} + g_{\mathrm{f}+}\boldsymbol{\Psi}_{\mathrm{N}}. \tag{2.24}$$

where $g_{\mathrm{f}} = \vartheta(1-\omega_{\mathrm{f}})$, $0 \leq \vartheta \leq 2$. It is seen that $\vartheta = 0$ gives upwind interpolation, $\vartheta = 1$ gives linear interpolation and $\vartheta = 2$ gives downwind interpolation.

The *gradient terms* present in the N–S–F equations are $\boldsymbol{\nabla} p$ in equation (2.14) and are usually integrated over a control volume and discretised as follows: [30]

$$\int_V \boldsymbol{\nabla}\boldsymbol{\Psi} dV = \int_S dS\boldsymbol{\Psi} \approx \sum_{\mathrm{f}} \mathbf{S}_{\mathrm{f}}\boldsymbol{\Psi}_{\mathrm{f}}, \tag{2.25}$$

The KT and KNP methods divide the interpolation procedure into f+ and f- directions according to:

$$\sum_{\mathrm{f}} \mathbf{S}_{\mathrm{f}}\boldsymbol{\Psi}_{\mathrm{f}} = \sum_{\mathrm{f}} \left[\theta \mathbf{S}_{\mathrm{f}}\boldsymbol{\Psi}_{\mathrm{f+}} + (1-\theta)\, \mathbf{S}_{\mathrm{f}}\boldsymbol{\Psi}_{\mathrm{f\text{-}}}\right], \tag{2.26}$$

where f+ and f- interpolation uses the limiter described above.

For completeness, the *Laplacian terms* are initially discretised with diffusion coefficient Γ for polyhedral meshes as follows [30]:

$$\int_V \boldsymbol{\nabla}\boldsymbol{\cdot}\left(\Gamma\boldsymbol{\nabla}\boldsymbol{\Psi}\right) dV = \int_S dS \cdot \left(\Gamma\boldsymbol{\nabla}\boldsymbol{\Psi}\right) \approx \sum_{\mathrm{f}} \Gamma_{\mathrm{f}}\mathbf{S}_{\mathrm{f}} \cdot \left(\boldsymbol{\nabla}\boldsymbol{\Psi}_{\mathrm{f}}\right). \tag{2.27}$$

The Γ_{f} is interpolated linearly from cell centre values. For the general case where a face is non-orthogonal (i.e. $\mathbf{S}_{\mathrm{f}}$ is not parallel to $\mathbf{d}$), the evaluation of $\mathbf{S}_{\mathrm{f}} \cdot \left(\boldsymbol{\nabla}\boldsymbol{\Psi}\right)_{\mathrm{f}}$ is divided into an orthogonal component in terms of neighbour and owner cell values and a non-orthogonal component in terms of a full gradient, calculated at cell centres and itself interpolated to the face [30]:

$$\mathbf{S}_{\mathrm{f}} \cdot \left(\boldsymbol{\nabla}\boldsymbol{\Psi}\right)_{\mathrm{f}} = \underbrace{A\left(\boldsymbol{\Psi}_{\mathrm{N}} - \boldsymbol{\Psi}_{\mathrm{P}}\right)}_{orthogonal} + \underbrace{\mathbf{a}\boldsymbol{\cdot}\left(\boldsymbol{\nabla}\boldsymbol{\Psi}\right)_{\mathrm{f}}}_{non-orthogonal}, \tag{2.28}$$

where $A = |\mathbf{S}_{\mathrm{f}}|^2/(\mathbf{S}_{\mathrm{f}} \cdot \mathbf{d})$ and $\mathbf{a} = \mathbf{S}_f - A\mathbf{d}$

The N–S–F equations are implemented and solved numerically in OpenFOAM [35] as the solver `rhoCentralFoam` for simulating high speed viscous flows. OpenFOAM is a open source CFD toolbox, written in C++. All solvers developed within OpenFOAM are, by default, 3-dimensional, but can be used for 1- or 2-dimensional problems by the application of particular boundary conditions lying on the plane of directions of no interest.

2.5.3 The hybrid method

The DSMC method simulates successfully hypersonic gas flows in all regimes but with high computational cost. In the transition-continuum regime ($0.1 \leq Kn \leq 1$), the N–S–F equations become inappropriate. Thus, either CFD or the DSMC method on its own fails to provide both a comprehensive and numerically-efficient computational modelling capability across all regimes. A natural solution to this problem is to develop a hybrid CFD–DSMC method [36, 74].

The accuracy of a hybrid CFD–DSMC method relies on the proper positioning of the CFD–DSMC interfaces. The interfaces must lie in near-equilibrium regions where solutions of the N–S–F equations will introduce minimal error. Typically, molecule and continuum regions are determined by evaluating a continuum breakdown parameter in the flow field. In [36,74], the hybrid method uses the Knudsen number defined with the length scale of a macroscopic gradient in equation (2.2) as a continuum breakdown parameter.

In regions of the flow field where $Kn \leq 0.05$, the discrepancy between a CFD and DSMC solution can be less than 5%. Thus, these regions could be solved using a continuum approach. The hybrid method begins with a CFD solution of the entire flow field and then uses equation (2.2) to decompose the domain into CFD and DSMC regions. State-based coupling can be used to transfer information between molecular and continuum regions. After evaluation of the breakdown parameter, the molecular region is extended by a few extra cells into the continuum domain to create an overlap region. The overlap regions help to improve the accuracy of the DSMC fluxes. One row of CFD and two rows of DSMC boundary cells are initialized, and then the DSMC and CFD domains are coupled by transferring information across the interfaces. With state-based coupling, this involves updating the boundary conditions of each solver. In this way, information transfer into both the molecular and continuum solvers is handled through existing boundary procedures already used by both solvers. The DSMC boundary cells are continually filled with molecules consistent with the flow properties in the corresponding CFD cells. As molecules in the DSMC domain interact and their distributions evolve in time, the hybrid also tracks the macroscopic variation in each DSMC cell. These averaged DSMC properties are then used to update boundary conditions for the CFD solver [74].

The hybrid method is able to reproduce successfully the results of the DSMC simulations at a smaller computational effort [74]. However, it faces difficult challenges in identifying a reliable continuum breakdown parameter for switching from one scheme to the other, and the matching condition at the interface between the two domains [36]. Moreover, the high computational expense of DSMC still dominates the hybrid technique, and simulating flows around realistic geometries remains practically intractable [75].

2.6 The viscosity-temperature relation

The viscosity-temperature relation is important in the continuum-fluid modelling of hypersonic gas flows. For gases, the viscosity increases with increasing temperature. This thesis focuses on the Power and the Sutherland Laws describing the viscosity-temperature relationship in simulations.

The Power Law is simple, and expressed as:

$$\mu = A_P T^s, \tag{2.29}$$

where A_P (Pa.s K^s) is a constant of proportionality. The accuracy of the Power Law depends on the exponent s over the range of temperature, T. The value s is suitably chosen to satisfy experimental data. For argon, $s = 0.68$ over the temperature range, T, from 80 to 2000 K, and $s = 0.76$ at temperatures, T, up to 15000 K [37]. Values of s for helium and xenon can also be found in [37].

Sutherland's Law is more complicated than the Power Law. It adds a weak attractive component to the intermolecular force, which is more realistic. Sutherland's Law is expressed as:

$$\mu = A_S \frac{T^{1.5}}{T + T_S}, \tag{2.30}$$

where A_S and T_S are constants. This law is valid only if the attractive component to the intermolecular force is small. So Sutherland's Law does not fit the experimental data well for gases like hydrogen and helium, in which the Power Law is a better fit over the temperature range, T, from 20 to 500 K [1]. However,

Sutherland's Law is accurate for air over a range of several thousand degrees and is certainly appropriate for hypersonic viscous-flow calculations [1]. The values A_S and T_S for different gases in the range of gas temperature, T, from 58 to 1000 K are given in Table 2.1 taken from references [38–41].

Table 2.1: Value of A_S and T_S in Sutherland's Law, equation (2.30)

Gas	A_S (Pa.s K$^{-1/2}$)	T_S (K)
Air	1.46×10^{-6}	110.4
Nitrogen	1.41×10^{-6}	111
Oxygen	1.69×10^{-6}	127
Argon	1.93×10^{-6}	142

Whichever model for viscosity is adopted, the coefficient of thermal conductivity may be determined from the formula:

$$k = \frac{c_p \mu}{Pr}, \tag{2.31}$$

where the Prandtl number, Pr, is assumed to be constant and c_p is the constant pressure specific heat.

2.7 Summary

In this chapter, relevant kinetic theory of gases, different fluid governing equations and different simulation methods for modelling nonequilibrium gas flows were reviewed. The advantages and disadvantages of these equations and methods were briefly described. It is clear that modelling nonequilibrium gas flow is both challenging and, using traditional approaches, computational intensive. One of the major challenges, whatever the simulation method adopted, is choosing the correct surface boundary conditions. These are critical to obtaining good simulated results, and will be discussed in detail in the next chapter. To develop a realistic model, it is necessary to understand the physics and chemistry of interfacial phenomena.

In the present work, we focus on the surface boundary conditions in CFD, which solves the N–S–F equations. The simulation results of CFD are compared with DSMC and experimental data given in literature.

Chapter 3

Nonequilibrium boundary conditions

3.1 Introduction

Surface slip/jump boundary conditions are important for calculating the slip velocity, surface temperature and surface pressure for re-entry vehicles designs. In the CFD method, such boundary conditions should increase the maximum Knudsen number from 0.01 to 0.1 for accurate N–S–F solutions. The accuracy of the full-field computational results depends on the surface boundary conditions applied. The appropriate treatment of the boundary conditions is critical when comparing DSMC or experimental data to the CFD results.

In this chapter, the common slip velocity conditions and temperature jump conditions are revisited. These are the Maxwell slip [5] condition, the Smoluchowski jump [6] condition and the second-order slip condition [16]. The latter slip condition is developed following kinetic theory applied to rarefied gas micro-flows in planar surface geometries. The second-order temperature jump in [76] only appears to produce solutions in conjunction with high-order BGK-Burnett constitutive equations for hypersonic gas flows. Alternative slip/jump conditions, such as the Langmuir boundary conditions, are based on the adsorption isotherm given in [9, 10], and are also reviewed below. Simple tests of all these conditions are done for a laminar sharp-leading-edge flat plate case to investigate how they perform in hypersonic gas flows.

New slip/jump conditions are also proposed by combining the kinetic theory of gases with the Langmuir adsorption isotherm.

3.2 Gas–Surface interactions

When a gas molecule collides with a surface, it is reflected at a specific angle, velocity and temperature. If the molecule is reflected elastically, with an incoming angle equal to the receding angle, and with an unchanged momentum and energy, then this collision is known as a specular interaction [23]. This corresponds to smooth and adiabatic surfaces. The surface shear stress and heat transfer are zero in this case.

On the other hand, if the molecule is reflected inelastically, with an incoming angle unequal to the receding angle, and with a changed momentum and energy, then this collision is known as a diffuse interaction [23]. This corresponds to a rough surface held at constant temperature. The surface shear stress and heat transfer are not zero in this case.

In fact, the molecules collide with the surface in both specular and diffuse interactions. The accommodation coefficient is the fraction of incoming molecules that are reflected diffusely.

Moreover, if the molecules collide with a surface they may a) either stick permanently or b) remain at the surface long enough to reach thermal equilibrium, then leaving the surface. The latter case is known as "trapping". If the molecules stick on the surface held at constant temperature, this case is the adsorption isotherm [47]. The fraction of molecules that stick on the surface can be determined by the Langmuir adsorption isotherm. These may be considered as diffuse interactions [22, 23, 47]. In the present work, the solid surfaces are assumed to be isothermal.

3.3 Nonequilibrium surface boundary conditions

3.3.1 Surface boundary conditions in the CFD method

Most nonequilibrium slip/jump boundary conditions can be expressed in the form:

$$\phi + a\nabla_{\mathbf{n}} \left(\mathbf{S} \cdot \phi \right) = \Phi_L, \tag{3.1}$$

where ϕ is the variable of interest, e.g. velocity or temperature; with bold type denoting a vector or tensor quantity; $\nabla_{\mathbf{n}} \equiv \mathbf{n} \cdot \nabla$ is the component of the gradient normal to the boundary surface, with $\mathbf{n}$ being the unit normal vector defined as positive in the direction pointing out of the flow domain; a is a coefficient specific to each boundary condition and Φ_L is the limiting value in the case of no slip/jump, e.g. the surface velocity or temperature. The tensor $\mathbf{S} = \mathbf{I} - \mathbf{nn}$, where $\mathbf{I}$ is the identity tensor, removes normal components of any non-scalar field, e.g. velocity, so that slip only occurs in the direction tangential to the surface. The normal gradient can be expressed numerically as:

$$\nabla_{\mathbf{n}} \phi = C_{\Delta} \left(\phi - \phi_{\mathrm{i}} \right), \tag{3.2}$$

where the subscript 'i' denotes a value in the numerical cell adjacent to the boundary face of the solid surface, and $C_{\Delta} = 1/|\mathbf{d}_B|$, with $\mathbf{d}_B$ the distance from the numerical cell centre to the boundary face centre of the solid surface.

In the present work, all nonequilibrium boundary conditions will be expressed in the form of the general equation (3.1) above.

Slip velocity

In gas-surface interactions, the gas molecules can be grouped into two streams: approaching and receding. The viscous drag on the surface is due to the difference between the tangential momentum of the approaching stream and that carried away by the receding stream. The tangential momentum of the gas molecules is responsible for the shear stress, $\boldsymbol{\tau}$. Maxwell makes the assumption that the approaching gas molecules and the receding gas molecules have equal influence on the total shear stress at the surface:

$$\left[\frac{1}{2} \boldsymbol{\tau} \right]_{approaching} + \left[\frac{1}{2} \boldsymbol{\tau} \right]_{receding} = \left[\boldsymbol{\tau} \right]_{total}. \tag{3.3}$$

The stream of molecules receding from the surface is assumed to be equivalent to a simple effusive flow. A typical effusive velocity distribution will be that of a flow of individual molecules through a small hole in a planar surface with diameter of the order of the mean free path. The total number of molecules that impinge on the surface may be expressed in terms of the mean molecular velocity, $\bar{v}$, and the number density of molecules in the flow, η as [23]:

$$\Gamma_n = \frac{1}{4}\eta\bar{v}. \tag{3.4}$$

This number of molecules leaving the surface must be added to the momentum due to the slip velocity, $\mathbf{u}$, to produce the receding stream's contribution to the total shear stress at the surface. The observation of a slip velocity shows that some tangential momentum is retained by the gas at the surface. To determine the slip velocity while conserving momentum, Maxwell introduces the tangential momentum accommodation coefficient, σ_u. Incorporating density $\rho = \eta m$, equation (3.3) becomes:

$$\sigma_u \left[\frac{1}{2}\boldsymbol{\tau} + \frac{1}{4}\rho\bar{v}\mathbf{u}\right] = \boldsymbol{\tau}, \tag{3.5}$$

which can be re-arranged as,

$$\mathbf{u} = 2\left(\frac{2-\sigma_u}{\sigma_u}\right)\frac{\boldsymbol{\tau}}{\rho\bar{v}}. \tag{3.6}$$

Substituting the mean molecular velocity, $\bar{v}$, from a Maxwellian equilibrium distribution [23], gives

$$\bar{v} = 2\sqrt{(2RT/\pi)}. \tag{3.7}$$

The definition of the mean free path depends on collision models such as VHS, HS, and VSS models. The definition of λ from the HS model is commonly used for CFD in simulating hypersonic gas flows, and calculated in terms of macroscopic quantities as [23],

$$\lambda = \frac{\mu}{\rho}\sqrt{\frac{\pi}{2RT}}. \tag{3.8}$$

This definition of λ is used for all the CFD simulations in this thesis. From equations (3.6), (3.7) and (3.8), the most common form of the Maxwell slip boundary

condition in rarefied gas flows is obtained [5]:

$$\mathbf{u} = \left(\frac{2-\sigma_u}{\sigma_u}\right)\frac{\lambda\boldsymbol{\tau}}{\mu}. \tag{3.9}$$

The tangential momentum accommodation coefficient determines the proportion of molecules reflected from the surface specularly (equal to $1-\sigma_u$) or diffusely (equal to σ_u), and $0 \leq \sigma_u \leq 1$.

This formulation neglects the thermal creep, a process whereby a temperature gradient tangential to the surface generates additional slip flow in the direction of increasing temperature. The gas would then slide over a surface from colder to hotter regions (see also Section 6.7). Maxwell's general equation for use in three-dimensional geometries, including thermal creep, can be written in tensor form as follows:

$$\mathbf{u} = \left(\frac{2-\sigma_u}{\sigma_u}\right)\frac{\lambda\boldsymbol{\tau}}{\mu} - \frac{3}{4}\frac{Pr(\gamma-1)}{\gamma p}\boldsymbol{q} + \mathbf{u}_{\mathrm{w}}, \tag{3.10}$$

where $\mathbf{u}_{\mathrm{w}}$ is the surface velocity; the tangential shear stress is $\boldsymbol{\tau} = -\mathbf{S}\cdot(\mathbf{n}\cdot\boldsymbol{\Pi})$ and the heat flux is $\mathbf{q} = \mathbf{Q}\cdot\mathbf{S}$ at the surface; $\boldsymbol{\Pi}$ is the stress tensor at the surface; $\mathbf{Q}$ is the heat flux vector along the surface; p is the gas pressure at the surface.

Equation (3.10) can be expressed in the general form of equation (3.1) by substituting $\boldsymbol{\tau} = -\mathbf{S}\cdot(\mathbf{n}\cdot\boldsymbol{\Pi})$ and $\boldsymbol{\Pi} = \mu\nabla\mathbf{u}+\boldsymbol{\Pi}_{mc}$, with $\boldsymbol{\Pi}_{mc} = \mu(\nabla\mathbf{u})^{\mathrm{T}} - (2/3)\mathbf{I}\mathrm{tr}(\nabla\mathbf{u})$ into equation (3.10), where the superscript T denotes the transpose, and tr denotes the trace. Noting that $\mathbf{S}\cdot\nabla_{\mathbf{n}}\phi \equiv \nabla_{\mathbf{n}}(\mathbf{S}\cdot\phi)$, equation (3.10) then becomes:

$$\mathbf{u} + \left(\frac{2-\sigma_u}{\sigma_u}\right)\lambda\nabla_{\mathbf{n}}(\mathbf{S}\cdot\mathbf{u}) = \mathbf{u}_{\mathrm{w}} - \left(\frac{2-\sigma_u}{\sigma_u}\right)\frac{\lambda}{\mu}\mathbf{S}\cdot(\mathbf{n}\cdot\boldsymbol{\Pi}_{mc}) - \frac{3}{4}\frac{\mu}{\rho}\frac{\mathbf{S}\cdot\nabla T}{T}. \tag{3.11}$$

The right hand side of equation (3.11) contains 3 terms that are associated with (in order): the surface velocity, the so-called curvature effect [8], and thermal creep.

The second order velocity slip boundary condition for planar surfaces [16] can be expressed as follows:

$$\mathbf{u} + A_1\lambda\nabla_{\mathbf{n}}(\mathbf{S}\cdot\mathbf{u}) + A_2\lambda^2\nabla^2_{\mathbf{n}}(\mathbf{S}\cdot\mathbf{u}) = \mathbf{u}_{\mathrm{w}}, \tag{3.12}$$

where A_1 and A_2 are slip coefficients for the first and second order terms respectively. Their values are proposed either from theory or from experiment and are still the subject of much discussion. Equation (3.12) can be expressed in the general form of equation (3.1) by substituting $\nabla_{\mathbf{n}}\mathbf{u} = C_{\Delta}(\mathbf{u} - \mathbf{u}_{\mathrm{i}})$ into equation (3.12):

$$\mathbf{u} + (A_1\lambda + A_2\lambda^2 C_{\triangle})\nabla_{\mathbf{n}}(\mathbf{S}\cdot\mathbf{u}) = \mathbf{u}_{\mathrm{w}} + A_2\lambda^2 C_{\Delta}\nabla_{\mathbf{n}}(\mathbf{S}\cdot\mathbf{u})_{\mathrm{i}}. \tag{3.13}$$

Both the above slip conditions are "fictitious slip" conditions at the surface. When the Navier-Stokes-Fourier equations are used with a fictitious slip condition at the surface, the prediction of the velocity in the Knudsen layer is not accurate by linear constitutive relations. The Knudsen layer is a near-surface region approximately one to two mean free paths in thickness where local thermodynamic equilibrium is not maintained. However, the fictitious slip condition does capture the velocity outside the Knudsen layer, as seen in Figure 3.1.

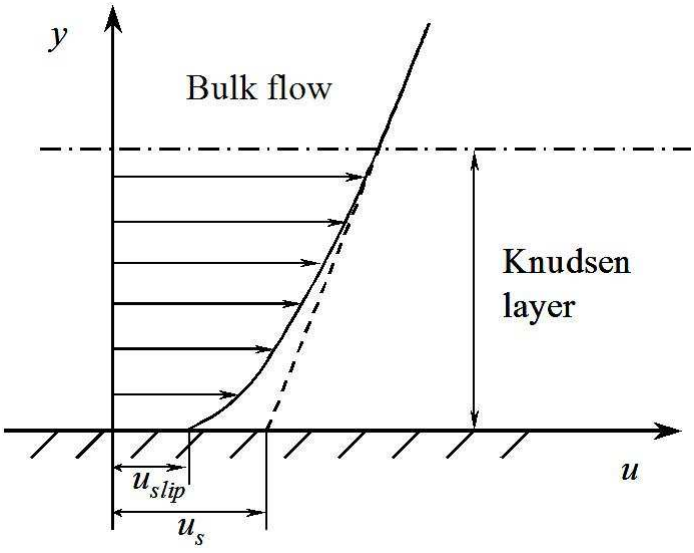

Figure 3.1: The dash line presents the velocity profile using the N-S-F equations with a "fictitious slip' velocity u_s, and the solid line corresponds to the actual velocity profile.

Temperature jump

Experimental observations show that the temperature of a rarefied gas at a surface is not equal to the surface temperature, T_w. This difference is called the "temper-

ature jump" and is driven by the heat flux normal to the surface. By analogy with Maxwell's arguments for the slip velocity, the energy of approaching molecules impinging on a unit area of surface is responsible for the heat conducted through the surface. Smoluchowski assumes that the approaching stream of molecules conducts the same level of heat and does dissipative work as that within the region of gas some distance away from the boundary. The approaching and receding streams contribute to half of the conduction of heat. Similar to the derivation of slip velocity, to determine the temperature jump while conserving the energy, a thermal accommodation coefficient, σ_T, is introduced (with $0 \leq \sigma_T \leq 1$) [23]. Perfect energy exchange between the gas and the solid surface corresponds to $\sigma_T = 1$, and no energy exchange to $\sigma_T = 0$. Therefore we have:

$$-[k\nabla_{\mathbf{n}}T]_{total} = \sigma_T(-[\frac{1}{2}k\nabla_{\mathbf{n}}T]_{approaching} + [\frac{1}{2}k\nabla_{\mathbf{n}}T]_{receding}), \tag{3.14}$$

The internal energy of the molecules will be normally $e = c_v T$ per unit mass. The translatory energy of molecules colliding with unit area of boundary is 4/3 times as great as the mean translatory energy of molecules in equilibrium at the same temperature [23]. The energy of colliding molecules is then higher by a factor $(\gamma + 1)/2$ corresponding to an energy $(c_v + R/2)T$. The mass of the molecules colliding with unit area of boundary is $\rho\bar{v}/4$, so the intergal energy per unit area is $\rho\bar{v}(\gamma + 1)e/8$. The conduction of heat of the receding stream is a difference between the internal energy of the gas e and that of the surface e_w and is calculated [23]:

$$[\frac{1}{2}k\nabla_{\mathbf{n}}T]_{receding} = \frac{1}{8}\rho\bar{v}(\gamma + 1)(e - e_w), \tag{3.15}$$

which is re-arranged by replacing $\rho\bar{v} = 2\mu/\lambda$, $e = c_v T$ and $e_w = c_v T_w$ as,

$$[\frac{1}{2}k\nabla_{\mathbf{n}}T]_{receding} = \frac{1}{4}\frac{\mu}{\lambda}(\gamma + 1)c_v(T - T_w). \tag{3.16}$$

Inserting equation (3.16) into equation (3.14) gives the Smoluchowski temperature jump in rarefied gas flows, which in the form of equation (3.1) is [6, 23],

$$T + \frac{2 - \sigma_T}{\sigma_T}\frac{2\gamma}{(\gamma + 1)\,Pr}\lambda\nabla_{\mathbf{n}}T = T_{\mathrm{w}}. \tag{3.17}$$

Langmuir boundary conditions

Adsorption is the process by which free gas molecules attach to a surface. The gas molecule that adsorbs is the "adsorbate" and the surface is the "adsorbent". Adsorption is usually described through isotherms, that is, the amount of adsorbate on the adsorbent as a function of its pressure at constant temperature.

The Langmuir adsorption isotherm model proposed for gases adsorbed on the surface described in references [9,10,42–45] is based on the following assumptions:

- adsorption cannot proceed beyond monolayer coverage of the surface.
- all surface sites are equivalent and can accommodate one adsorbed atom.
- there are no interactions between the occupied sites.

The adsorption isotherm process between the gas molecules and the surface is shown in Figure 3.2. Here M is the chemical name of the free gas molecules, S_v is

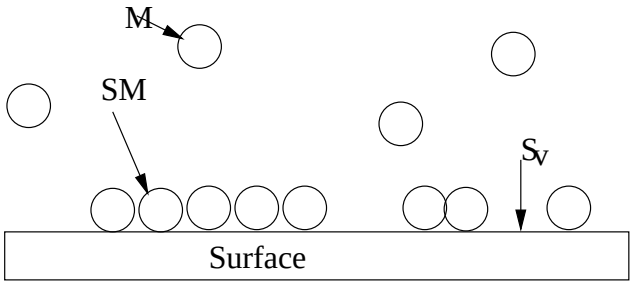

Figure 3.2: Schematic of the Langmuir adsorption isotherm model.

a vacant surface sites (adsorbent) and SM is an occupied surface site (adsorbate). The gas-surface interaction process can be regarded as a chemical reaction [42]:

$$S_v + M \rightleftarrows SM. \tag{3.18}$$

A chemical equilibrium constant K_L for this chemical reaction depends on the M, S_v, and SM and is determined by:

$$K_L = \frac{SM}{S_v M}. \tag{3.19}$$

If α is the fraction of coverage (occupied surface sites) ($0 \leq \alpha \leq 1$), [SM] is proportional to α, $[S_v]$ is proportional to the number of vacant sites $(1 - \alpha)$, and

[M] is proportional to the pressure of the gas, p. This fraction α can be calculated for different gases as follows:

For a monatomic gas:

$$\alpha = \frac{\beta p}{1 + \beta p}, \tag{3.20}$$

where β is defined below.

For a diatomic gas, a molecule approaching the surface may be adsorbed on the surface only if two particular elementary sites are vacant. The chance of one of these sites being vacant is $(1-\alpha)$ and the chance that both sites will be vacant is $(1-\alpha)^2$. Thus the rate of condensation is proportional to $(1-\alpha)^2$. Evaporation only occurs when adsorbed atoms are in adjacent sites. The chance that an atom shall be in a given site is α and therefore the chance that atoms will be in adjacent sites is equal to α^2. Thus the rate of evaporation of molecules from the surface is proportional to α^2. From this reasoning, the following adsorption isotherm for a diatomic gas can be found [10, 45]:

$$\alpha = \frac{\sqrt{\beta p}}{1 + \sqrt{\beta p}}, \tag{3.21}$$

For a gas mixture, consisting of two gas components, for example, nitrogen and oxygen, with V_g denoting the volume fraction of the components (i.e. $V_{gN_2} + V_{gO_2} = 1$), then the fraction α can be expressed [10, 45]:

$$\alpha = V_{gN_2} \frac{\sqrt{\beta_{N_2} p}}{1 + \sqrt{\beta_{N_2} p}} + V_{gO_2} \frac{\sqrt{\beta_{O_2} p}}{1 + \sqrt{\beta_{O_2} p}}, \tag{3.22}$$

where β is an equilibrium constant relating to the surface temperature, given by:

$$\beta = \frac{K_L}{R_u T_w}, \tag{3.23}$$

where R_u is the universal gas constant (J/kmol K) and K_L is [10, 42]:

$$K_L = A_m \lambda \exp\left(\frac{D_e}{R_u T_w}\right), \tag{3.24}$$

so that

$$\beta = \frac{A_m \lambda}{R_u T_w} \exp\left(\frac{D_e}{R_u T_w}\right), \tag{3.25}$$

where A_m is the mean area of a site (m^2/mol) and is either measured or calculated approximately by $N_A \pi d^2/4$ for gases [10, 45], with d the molecular diameter and N_A the Avogadro number; D_e is the measured value of the heat of adsorption (J/mol): for argon and nitrogen gases $D_e = 5255$ (J/mol) given in references [9, 42, 45].

With α determined, the boundary values for temperature and velocity are calculated as [9, 10, 42]:

$$\phi = \alpha\phi_w + (1 - \alpha)\,\phi_g, \tag{3.26}$$

or

$$\phi + \frac{(1 - \alpha)}{\alpha}\,(\phi - \phi_g) = \phi_w, \tag{3.27}$$

where ϕ can represent either $\mathbf{u}$ or T. The subscript g represents either a reference value or a local value adjacent to the surface (i.e. at a mean free path's distance from the surface). Depending on a particular case, the reference value may be either a freestream value or a outflow value to obtain accurate results. Thus, this is not a general way to derive the Langmuir boundary conditions. Moreover, the Langmuir conditions developed with the reference value using the N–S–F equations did not give good results in simulating hypersonic gas flows in [77]. So, the Langmuir boundary conditions are expressed with a local adjacent value. If ϕ_g is the value of ϕ a mean free path away in the direction normal to the surface, then $\phi - \phi_g \approx \lambda \nabla_{\mathbf{n}} \phi$. The Langmuir model is then:

$$\phi + \lambda \frac{(1 - \alpha)}{\alpha} \nabla_{\mathbf{n}} \phi = \phi_w. \tag{3.28}$$

Expressed this way, the Langmuir boundary conditions have the same form as the Smoluchowski jump condition, and the Maxwell boundary condition without the thermal creep term and the curvature effect, but with $(2 - \sigma_u)/\sigma_u$ and $(2 - \sigma_T)/\sigma_T$ in equations (3.11) and (3.17), respectively replaced by $(1 - \alpha)/\alpha$. The coefficient for the Langmuir boundary condition is calculated from equation (3.25), which depends on the values of A_m and D_e, whereas σ_u and σ_T are the only free parameters in the Maxwell/Smoluchowski conditions.

3.3.2 Surface boundary condtions in the DSMC method

The surface boundary conditions in the DSMC method simulate gas-surface interactions: DSMC molecules are adsorbed by the surface and then re-emitted. There are two general types of interactions: specular and diffuse, as presented in Section 3.2.

In fact, DSMC molecules collide with the surface and experience both specular and diffuse interactions. The accommodation coefficients represent the fraction of incoming DSMC molecules that are reflected diffusely and the remainder are reflected specularly [50–52]. Velocity slip and the temperature jump (including translational, rotational and vibrational temperature jumps) in [50–52] are calculated using Bird's DSMC implementation [26]. There is no difference between the DSMC and real molecule velocity, and the mass of a real molecule m is used for calculating slip/jump quantities [78]. When accommodation coefficients are equal to 1,

$$u_s = \frac{\sum\left(\left(m/u_n\right)u_p\right)}{\sum\left(m/u_n\right)} - u_w, \tag{3.29}$$

$$T_{tra,j} = \frac{1}{3R}\frac{\sum\left(\left(m/\left|u_n\right|\right)\left(\left|\left|u\right|\right|\right)\right) - \sum\left(m/\left|u_n\right|\right)u_s^2}{\sum\left(1/\left|u_n\right|\right)} - T_{tra,w}, \tag{3.30}$$

$$T_{rot,j} = \frac{1}{R}\frac{\sum\left(e_{rot}/u_n\right)}{\sum\left(1/\left|u_n\right|\right)} - T_{rot,w}, \tag{3.31}$$

$$T_{vib,j} = \frac{\Theta}{ln\left(\frac{R\Theta}{E_{vib}}+1\right)} - T_{vib,w}, \quad E_{vib} = \frac{\sum\left(e_{vib}/\left|u_n\right|\right)}{\sum 1/\left|u_n\right|}, \tag{3.32}$$

where u_n is the velocity normal to the surface; u_p is the velocity parallel to the surface; $||u||$ is the velocity magnitude; $T_{tra,j}, T_{rot,j}$ and $T_{vib,j}$ are the translational, rotational and vibrational temperature jumps, respectively; and $T_{tra,w}, T_{rot,w}$ and $T_{vib,w}$ are the translational, rotational and vibrational surface temperature, respectively.

The u_n and u_p in the equations are taken prior to and after the collision with the

surface, and the summations include pre- and post-collision molecules.

The viscosity and thermal conductivity are calculated in [50–52] according to a power law viscosity/temperature relationship, through the equations:

$$\mu = \mu_{ref} \left(\frac{T}{T_{ref}} \right)^{\omega}, \tag{3.33}$$

where

$$\mu_{ref} = \frac{15\sqrt{\pi m k_B T_{ref}}}{2\pi\, d_{ref}^2\, (5 - 2\omega)\, (7 - 2\omega)}, \tag{3.34}$$

where ω is the temperature exponent; d_{ref} is the reference diameter of a real molecule; and T_{ref} is the reference temperature.

3.4 Testing the boundary conditions

In this section, the Maxwell slip, the second-order slip, the Smoluchowski jump with various coefficients σ_u, σ_T, A_1 and A_2, and the Langmuir slip/jump conditions are tested for a laminar flat plate flow that is a simple test case. Experimental data is available from Becker [46] with an uncertainty of $\pm 1\%$. The freestream flow conditions of test case are $\lambda_\infty = 0.23$ mm, $p_\infty = 3.73$ Pa, $T_\infty = 64.5$ K, $u_\infty = 1893.7$ m/s, $T_w = 292$ K, and argon as the working gas. The Langmuir models are tested with the covalent and the Van der Waals diameters of a molecule. The covalent diameter is a measure of the size of the molecule which forms part of a covalent bond, while the Van der Waals diameter of a molecule is the diameter of an imaginary hard sphere. The rectangular mesh with the cell size $\Delta x = \Delta y = 0.1\lambda_\infty$ is used for simulations. The viscosity is calculated by the Sutherland law with the values $A_s = 1.93\times\ 10^{-6}$, and $T_s = 142$ K from Table (2.1) for equation (2.30). The results of simulations are compared with the experimental data in Figures 3.3 and 3.4.

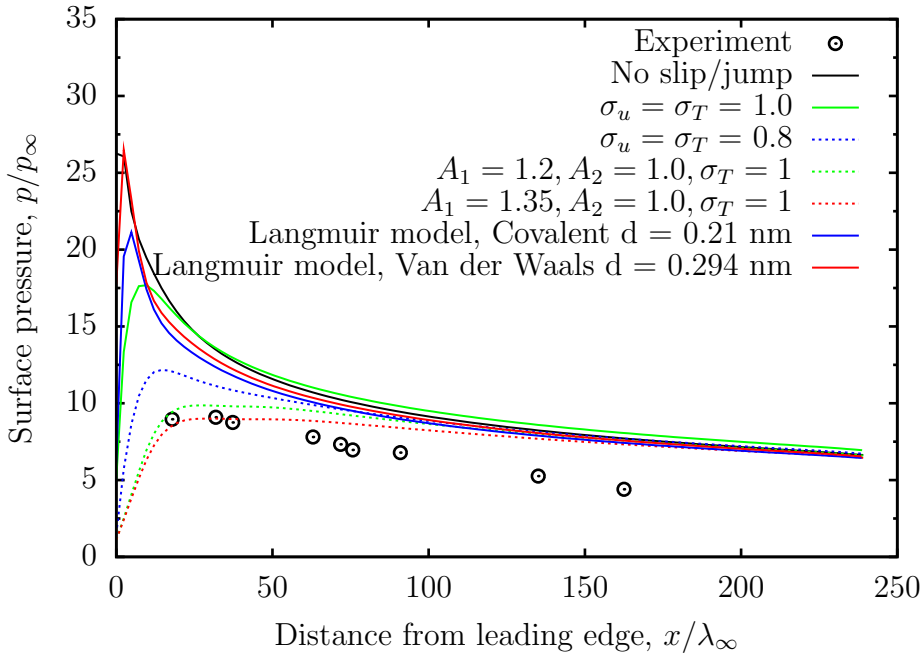

Figure 3.3: Becker's case [46] with various boundary conditions, the surface pressure distribution along the flat plate.

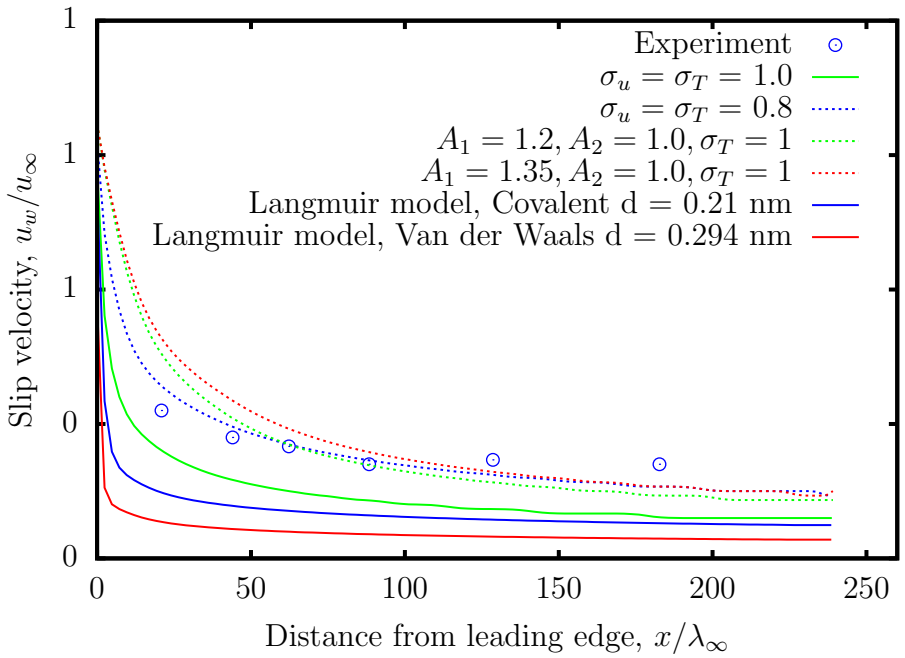

Figure 3.4: Becker's case [46] with various boundary conditions, the slip velocity along the flat plate.

From the results obtained, the values σ_u, σ_T, A_1 and A_2 very sensitively affect the surface pressure and the slip velocity. They decide the accuracy of the simulation results. The results of the Langmuir models did not give as good agreement with the experimental data as the Maxwell/Smoluchowski models or the second order/Smoluchowski models, as they overpredict the surface pressure, and underpredict the slip velocity. The no-slip/jump test also overpredicts the surface pressure. It is seen that the covalent diameter gives better results than the Van der Waals diameter in the Langmuir models, however.

3.5 New surface boundary conditions for CFD

The surface boundary conditions used in the above tests depend on free parameters σ_u, σ_T, A_1 and A_2. In calculating the slip/jump, the Langmuir conditions only consider the molecules adsorbed on the surface and ignore diffuse reflection at the surface. The adsorption of molecules on a surface is classified as a kind of diffuse reflection [22, 23]. In the Maxwell slip conditions, specular reflection of molecules is given indirectly by tangential momentum accommodation coefficient and does not affect the slip velocity. New boundary conditions are developed after obtaining the desired values of σ_u, σ_T, A_1 and A_2 in the present work. Our earlier simulation results in [79] proposed the value $\sigma_T = 1.0$ in the Smoluchowski jump condition for simulating hypersonic gas flows.

The above observation suggests that, only diffuse reflection and perfect energy exchange are taken into account for developing modified slip/jump conditions (i.e. $\sigma_u = \sigma_T = 1.0$), in which the molecules adsorbed at the surface are considered as diffusely reflected. The molecules adsorbed that are determined by the fraction α, only contribute to the part of the total fluid shear stress at the surface due to the approaching molecules (i.e. $\boldsymbol{\tau}_{receding}$ due to the molecules adsorbed is zero) [47]. The temperature of these emitted molecules is equal to the surface temperature ($T = T_w$). So following equations (3.3), (3.14) and (3.16), with the fraction $(1 - \alpha)$ added to the terms involving receding molecules, gives.

$$\left[\frac{1}{2}\boldsymbol{\tau}\right]_{approaching} + \left[\frac{1}{2}(1-\alpha)\boldsymbol{\tau}\right]_{receding} = [\boldsymbol{\tau}]_{total}\,, \tag{3.35}$$

and

$$-[k\nabla_{\mathbf{n}}T]_{total} = (-[\frac{1}{2}k\nabla_{\mathbf{n}}T]_{approaching} + [\frac{1}{2}(1-\alpha)k\nabla_{\mathbf{n}}T]_{receding}). \tag{3.36}$$

Following the algebraic manipulations similar to those employed on the Maxwell/ Smoluchowski conditions, the new slip boundary condition in the form of equation (3.1) is obtained as follows:

$$\mathbf{u} + \left(\frac{1}{1-\alpha}\right)\lambda\nabla_{\mathbf{n}}(\mathbf{S}\cdot\mathbf{u}) = \mathbf{u}_{\mathrm{w}} - \left(\frac{1}{1-\alpha}\right)\frac{\lambda}{\mu}\mathbf{S}\cdot(\mathbf{n}\cdot\mathbf{\Pi}_{mc}) - \frac{3}{4}\frac{\mu}{\rho}\frac{\mathbf{S}\cdot\nabla T}{T}. \tag{3.37}$$

The right hand side of this new slip condition, named the "Langmuir-Maxwell slip condition", also contains 3 terms that are associated with (in order): the surface velocity, the so-called curvature effect [8], and thermal creep. The new temperature jump condition may also be expressed in the form of equation (3.1), and named the "Langmuir-Smoluchowski jump condition":

$$T + \frac{1}{1-\alpha}\frac{2\gamma}{(\gamma+1)\,Pr}\lambda\nabla_{\mathbf{n}}T = T_{\mathrm{w}}. \tag{3.38}$$

In the present work, we only consider physical adsorption, which implies that gases have no chemical interaction with a surface. The gases will be adsorbed by the solid surface as a result of purely physical forces [48]. Therefore, the value of heat of adsorption, De, is small and falls within the range from 0.1 to 10 kcal/mol [10, 45] that leads to a small value of α. This guarantees that the coefficient $(1-\alpha)$ does not become close to zero in these new surface boundary conditions.

From equations (3.11, 3.13, 3.17, 3.28, 3.37, 3.38), the specific coefficients a for the different models for velocity slip and temperature jump in the form of general equation (3.1) are collated in Table 3.1. The Langmuir-Maxwell/Langmuir-Smoluchowski conditions are called the "new Boundary Conditions" (BCs) in the following chapters.

Table 3.1: Coefficient a in equation (3.1) for various slip/jump boundary conditions

Velocity slip	Temperature jump	Coefficient a
–	Smoluchowski	$\lambda((2-\sigma_T)/\sigma_T)(2\gamma/((\gamma+1)Pr))$
Maxwell	–	$\lambda(2-\sigma_u)/\sigma_u$
Langmuir	Langmuir	$\lambda(1-\alpha)/\alpha$
Second-order	–	$A_1\lambda + A_2\lambda^2 C_\Delta$
Langmuir-Maxwell	–	$\lambda/(1-\alpha)$
–	Langmuir-Smoluchowski	$(\lambda/(1-\alpha))(2\gamma/((\gamma+1)Pr))$

3.6 Numerical implementation of boundary conditions

The open source CFD software, OpenFOAM [35], is used in the present work. It uses finite volume (FV) numerics to solve systems of partial differential equations ascribed on any 3-dimensional unstructured mesh of polygonal cells. The FV discretisation is based on Gaussian integration and so uses values and normal gradients of fields at cell faces. If the face belongs to a boundary, the face value and gradient required by the discretisation procedure, must be obtained from the boundary condition. Various fundamental types of boundary conditions are implemented in OpenFOAM, including one called "partial slip"; that is a mixture of a fixed value, or Dirichlet, condition and a zero gradient condition (i.e. a Neumann condition where the normal gradient is zero). The "mixing" is controlled by a fraction coefficient σ ($0 \leq \sigma \leq 1$) where $\sigma = 0$ for the zero gradient condition and $\sigma = 1$ for a fixed value condition. A reference value is also required that is assigned to the fraction of the boundary condition that is a fixed value.

For the case of scalar fields, this OpenFOAM boundary condition can be used as the basis for any slip/jump boundary condition described by equation (3.1), by setting [49]

$$\sigma = 1 - \frac{aC_\Delta}{1 + aC_\Delta}, \tag{3.39}$$

and setting the value Φ_L to be the reference value for the fixed value component. For the case of vector fields, the standard partial slip condition was modified to include the tensor $\mathbf{S}$, so that only the tangential components of the field are "slipped". In either case, the fraction values, σ, for the boundary conditions considered are simply determined by equation (3.39) with the values of a from

Table 3.1. In the present work, the Langmuir models, the second order slip condition and the new slip/jump conditions were originally implemented into the solver `rhoCentralFoam` in OpenFOAM for simulating high speed viscous flows.

3.7 Conclusions

In this chapter, a summary of the common slip/jump boundary conditions based on the kinetic theory of gases and the Langmuir adsorption isotherm was presented. The results of the simple test in Section 3.4 show that a) there are difficulties in choosing the correct values of the free parameters σ_u, σ_T, A_1, and A_2 and b) the covalent diameter should be used in the Langmuir models in hypersonic gas flows. New surface boundary conditions have been proposed by inserting the Langmuir adsorption isotherm into the Maxwell/Smoluchowski equations. Their validation, and the desired values of free parameters σ_u, σ_T, A_1 and A_2, will be considered in the following chapters. It is seen that the DSMC translational temperature jump only depends on the components of velocity while the CFD temperature jump depends on the normal gradient of the temperature.

Chapter 4

Simulations of flow over a sharp-leading-edge flat plate

4.1 Introduction

Rarefied hypersonic flow over a flat plate with a sharp leading edge has been the subject of several experimental and theoretical investigations in past years. The results of experiments carried out very near the leading edge have generated much interest in the problem. At the leading edge, the frequency of collisions with the flat plate dominates the frequency of collisions between molecules. When the gas passes over the flat plate, there are initially very few collisions with it and the behaviour is free-molecular. Following more collisions, the gas flow behaviour is more transitional and reaches equilibrium further along the plate.

This chapter presents two-dimensional CFD simulations of rarefied hypersonic flow over a sharp-leading-edge flat plate at zero angle of attack, which are compared with experiments [46, 53–57] and DSMC data [60] over a Mach number range $Ma = 6$ to 22. Under low density conditions, both pressure and heat transfer data indicate large rarefied flow effects, with both a slip velocity and a temperature jump at the flat plate surface. Values of the accommodation coefficients (σ_u and σ_T) in the Maxwell velocity slip and Smoluchowski temperature jump boundary conditions were investigated in the range [0 – 1] to find good agreement with experimental and DSMC data. Moreover, the second-order slip condition is also investigated to obtain the desired values of first (A_1) and second (A_2) order coefficients. Due to limited experimental values of the heat adsorption

(D_e) in literature, the new slip/jump conditions (Langmuir-Maxwell/Langmuir-Smoluchowski) are tested for argon and nitrogen working gases in the flat plate cases given in [46, 53, 56]. From the results obtained, the covalent diameters of argon gas, $d_{Cov} = 0.21$ nm [58], and nitrogen gas, $d_{Cov} = 0.142$ nm [58], are used for calculations using the new boundary conditions.

4.2 Experimental arrangements and data

4.2.1 Experimental arrangements

In general, the experimental arrangements described in [46, 53–57] consist of: a) an apparatus for producing the flow under the desired test conditions, such as a heat stagnation chamber and a conical nozzle, b) measuring equipment such as pressure transducers, heat transfer gauges, thermocouples, optical lenses and electron beam gun, c) data acquisition equipment such as a spectrometer, PC and monochromator, and d) other equipment such as coolant pipes and pumps. These are shown schematically in Figure 4.1.

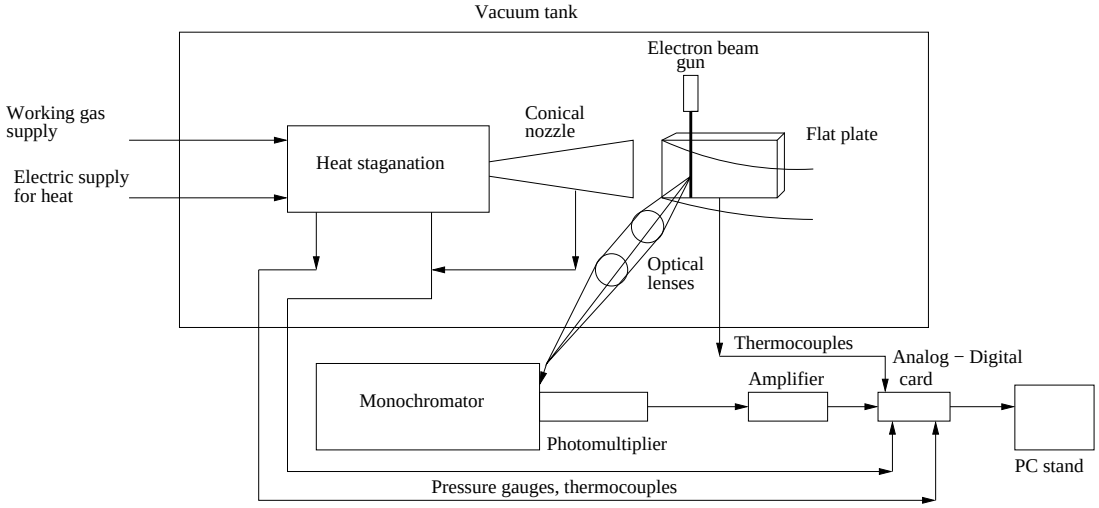

Figure 4.1: Schematic of experimental setup [57].

The flow conditions used in the experiments described in [46, 53–57], such as freestream temperature, T_∞, freestream pressure, p_∞ and freestream mean free path, λ_∞, are shown in Table 4.1. The experiment [53] was carried out for two different surface temperatures.

Table 4.1: Comparison of experimental flow conditions

	Ma	T_∞ (K)	p_∞ (Pa)	λ_∞(mm)	T_w (K)	Gas
Becker [46]	12.7	64.5	3.73	0.23	292	Argon
Metcalf *et al.* [53]	6.1	83.4	2.97	0.35	77	Nitrogen
Metcalf *et al.* [53]	6.1	83.4	2.97	0.35	294	Nitrogen
Vidal *et al.* [54]	22.0	41	0.51	0.83	308	Air
Becker *et al.* [55]	10.2	138	2.67	1.0	300	Air
Lengrand *et al.* [56]	20.2	13.32	0.068	2.35	290	Nitrogen
Tsuboi *et al.* [57]	4.89	116	2.12	0.86	290	Nitrogen

A low density wind tunnel was constructed for use in the experiments [46,53–57]. The heat stagnation (reservoir) chamber, the conical nozzle, optical lenses, the flat plate and electron beam gun are mounted in the wind tunnel. The working gas is driven into heat stagnation by the heat supply, which will produce a stagnation temperature T_0 and pressure p_0. These are measured in the heat stagnation chamber by a pressure gauge and thermocouple. Their values are chosen to ensure that any thermochemical non-equilibrium effects in the nozzle expansion are small, and to prevent liquefaction. A conical nozzle is connected to the stagnation chamber at the throat of the nozzle and the freestream flow issues at the exit of the conical nozzle, as seen in Figure 4.1. It is possible to change the area ratio of the throat to nozzle exit to take account of the thick boundary layer. The hypersonic flow through the conical nozzle is isentropic. The relationship of flow variables such as temperature, pressure and density between the heat stagnation chamber (T_0, p_0, ρ_0) and the exit of the conical nozzle (or freestream conditions T_∞, p_∞, ρ_∞) are expressed by isentropic expansion relations as follows:

Pressure

$$\frac{p_0}{p_\infty} = \left(1 + \frac{(\gamma - 1)}{2} M_\infty^2\right)^{(\gamma/\gamma - 1)}, \tag{4.1}$$

Density

$$\frac{\rho_0}{\rho_\infty} = \left(1 + \frac{\gamma - 1}{2} M_\infty^2\right)^{-1/\gamma - 1}, \tag{4.2}$$

Temperature

$$\frac{T_0}{T_\infty} = \left(1 + \left(\frac{\gamma - 1}{2} M_\infty^2\right)\right), \tag{4.3}$$

$$Ma = \frac{||u||}{c}, \tag{4.4}$$

where Ma is the Mach number and c is the speed of sound.

As described in references [46, 53–57] the flat plate is made of brass or copper with a length varying from 55 to 308 mm, while the sharp leading edge angle varies from 10 to 30 degrees. The thickness at the leading edge is less than 0.01 mm to ensure the flow field is not disturbed by shock detachment at the leading edge. The flat plate is mounted on the centreline of the wind tunnel, just behind the exit of the conical nozzle.

The electron beam gun and optical lenses are connected to each other in the wind tunnel. The light signal of the fluorescence created by the electron beam gun passes through optical lenses and is recorded by the spectrometer and photo-multiplier located outside the wind tunnel, and this optical data is stored in the PC. The electron beam gun is perpendicular to the flow direction and parallel with the flat plate (Figure 4.1). The gun and optical lenses can be fixed or movable in the wind tunnel. If fixed, as in [53], then the heat stagnation chamber, the conical nozzle and the flat plate move together; otherwise, if the electron beam gun and optical lenses move, then the chamber, nozzle and flat plate are fixed in the wind tunnel. Coolant pipes maintain the flat-plate wall temperature T_w presented in Table (4.1) by water-cooling in [46, 53–57]. The working gas is driven into the heat stagnation chamber and passed through the conical nozzle. At the conical nozzle exit, the working gas at freestream conditions travels across the flat plate.

4.2.2 Measurements

The density of gas in the flow is determined from the intensity of fluorescence of the working gas under the influence of electrons in the diagnostic beam. The beam travels across the flow, parallel to the plane of the plate, or otherwise the flat plate moves if the beam is fixed. By measuring the intensity of fluorescence at points along the beam, the local density can be determined because the intensity of fluorescence measured is almost proportional to the local density of the gas [46, 53–57].

The surface pressures can be measured using inductive pressure transducers connected to small holes (pressure orifices) with diameters of 0.5 to 1 mm drilled

into the flat plate surface and located along the longitudinal symmetry axis of the flat plate. In these transducers, a change in pressure produces a movement that changes the inductance of an electrical circuit. The variation is due to the displacement of a diaphragm inserted between two cavities of transducers. One cavity is connected to the pressure orifices on the flat plate surface, the other one is connected to a reference vacuum. The error of the measuring equipment is given in reference [46] as $\pm 1\%$.

In the experiments described by Metcalf *et al.* [53], capacitative pressure transducers were used, which have a thin diaphragm, usually metal, as one plate of a capacitor. The diaphragm is exposed to the process pressure on one side and to a reference pressure on the other. Changes in pressure cause it to deflect and change the capacitance. The inductance and capacitance variation can be monitored by electric signals at the transducer outputs.

In the experiment reported by Vidal *et al.* [54], piezoelectric pressure transducers with flush diaphragms drive a modified lead-zirconium-titanate crystal. The transducers have a dummy mass loading a second crystal to provide acceleration compensation. The transducers are connected through a short cable to a miniaturized cathode follower installed within the flat plate. When pressure is applied to the crystal, it is elastically deformed. This deformation results in a flow of electric charge. The resulting electric signal can be measured as an indication of the pressure which is applied to the crystal. The output signals of the transducers are recorded by a source follower. The pressure transducers usually generate output signals in the millivolt range. These are often then amplified to the volt level and recorded by the data acquisition system.

The surface temperature is measured by a series of thermocouples inserted just below the surface and located along the longitudinal axis of the flat plate. The output signals of the thermocouples are amplified and recorded by the data acquisition system.

The gas molecule rotational temperature in Tsuboi and Matsumoto's experiment [57] is measured by using the electron beam fluorescence method, with an uncertainty between 1 and 2%. When an electron beam is passed through the working gas, a molecule in an initial electronic state is excited to an ionized gas

molecule, caused by an inelastic collision with an electron. Emission of a photon from this inelastic collision state brings the molecule back to an ionized gas molecule at the ground state. The fluorescence in the R branch of the band spectrum is measured by the monochromator and the rotational temperature deduced through a calculation presented in [57].

The surface slip velocity is inferred by the measured surface pressure, p_w, and extrapolating the pitot pressure to the surface, p_{tw}. The Pitot pressure is the sum of dynamic and static pressures. The Pitot tubes faces the gas flow and the pitot pressure is fed into it, known as total head pressure or impact pressure. From the equations of state, continuity and momentum, the slip velocity, u_s, is calculated in [55] by:

$$u_s = \left(p_{tw} / \left(\rho_w \left(1 - \epsilon_w/2 + p_w/\rho_w {u_s}^2\right)\right)\right)^{1/2}, \tag{4.5}$$

wher ρ_w is the gas density at the surface and ϵ_w is the density ratio across a normal shock.

4.3 Direct simulation Monte-Carlo simulations

Due to the lack of direct experimental data for either slip velocity or surface temperature in the work of Becker [46] or the Metcalf *et al.* case $T_w = 294$ K [53], DSMC simulations have been run in OpenFOAM by White [60] to enable comparison fully with the CFD simulation results using new boundary conditions.

A regular rectangular mesh is used in the DSMC simulations. The cell size is determined by the mean free path. A cell size approximately $\lambda_\infty/3$ is used in the DSMC simulations [60]. The surface boundary conditions presented in Section 3.3.2 are applied with accommodation coefficients equal to 1. The variable hard sphere (VHS) model is used in the DSMC calculation with the parameters taken from [61] as follows:

Table 4.2: The VHS model parameters [61].

Species	Diameter (m)	ω	T_{ref} (K)	μ_{ref} (Nsm^{-2})
Argon	4.17×10^{-10}	0.81	273	2.117×10^{-5}
Nitrogen	4.17×10^{-10}	0.74	273	1.650×10^{-5}

The mean free path in the DSMC simulations of the flat plate cases is calculated in [61] as:

$$\lambda = \frac{2\mu}{15}(7-2\omega)(5-2\omega)\frac{\sqrt{2\pi RT}}{\rho}, \tag{4.6}$$

with a viscosity $\mu = T^{\omega}$ [26].

4.4 Choice of data

The experimental results given in [46, 53–55] show that the surface pressures reach a peak value near the leading edge and then decrease steadily along the flat plate, whereas in Lengrand *et al.*'s experiment [56], the surface pressures reach a peak value near the leading edge and then plateau. Tsuboi and Matsumoto's experiment [57] presents good data for translational and rotational temperatures for the surface-normal distances at different locations along the flat plate. The present work focuses on surface pressure, slip velocity and temperature jump data in order to test surface boundary conditions, therefore Tsuboi and Matsumoto's data are not used. The experimental data of surface pressures in Becker's, Metcalf *et al.*'s, Vidal *et al.*'s, Becker and Boylan's, and Lengrand *et al.*'s cases [46,53–56] are presented in Figure 4.2.

Six sets of experimental data from [46, 53–56] are selected for our simulations. The experimental data consists of the pressure, temperature jump and slip velocity. The flow conditions in these experiments are presented in Table 4.1. The experimental data for the temperature jump and slip velocity of the selected cases will be shown in the following sections.

The DSMC data in [60] are used for comparing with the CFD results in the Becker case [46] and the Metcalf *et al.* [53] case $T_w = 294$K.

4.5 Case setup

4.5.1 Boundary conditions

Various nonequilibrium boundary conditions are applied on the surface of the flat plate for the flow variables (T, $\mathbf{u}$). The boundary condition for the pressure p at the flat plate is zero normal gradient. This condition satisfies the equation

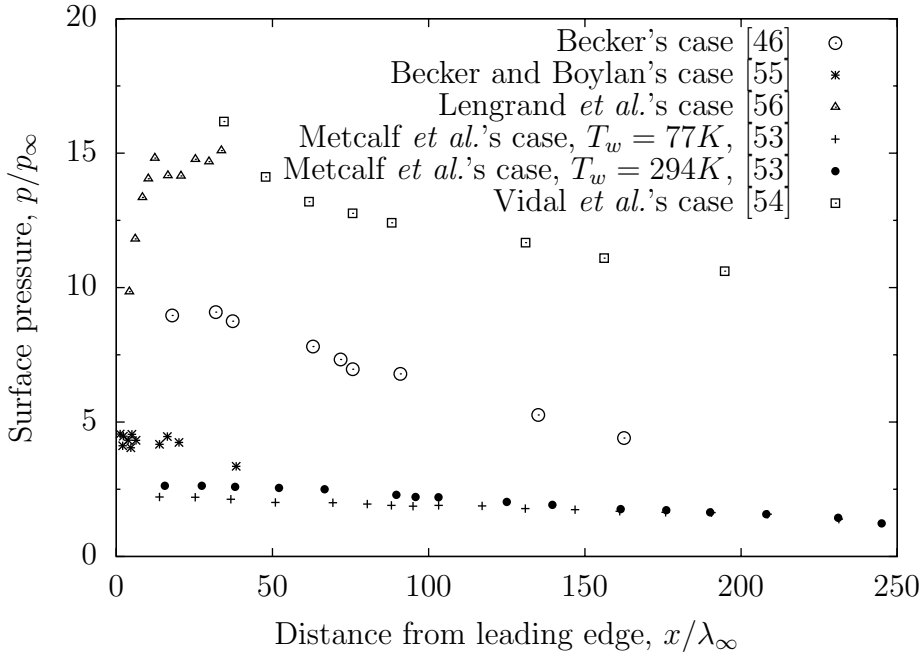

Figure 4.2: Surface pressure distribution along the flat plate, experimental data.

(2.14) in normal direction at steady state. At the inflow boundary, the freestream conditions were maintained throughout the computational process. At the top boundary and the outflow boundary, fluid is allowed to leave the computing region. This condition specifies that the normal gradients of the flow variables (p, T, $\mathbf{u}$) vanish at these boundaries. At the bottom boundary in front of the flat plate, a symmetry boundary condition is applied to all flow variables. A schematic diagram of the boundary conditions applied in the flat plate cases is shown in Figure 4.3.

4.5.2 Mesh

In the flat plate simulations, the computational results are sensitive to the numerical mesh sizes near the leading edge. A fine mesh is required at the leading edge to compute the flow field accurately. A typical mesh for a flat plate simulation is regular rectangular.

Four different meshes were employed to achieve mesh independence of the simulation results. A mesh study was conducted for all flat plate cases. Here, the results of Metcalf *et al.*'s case [53] are presented as an illustration. Four different mesh sizes are used with the grid spacing points in the x direction, Δx, and in

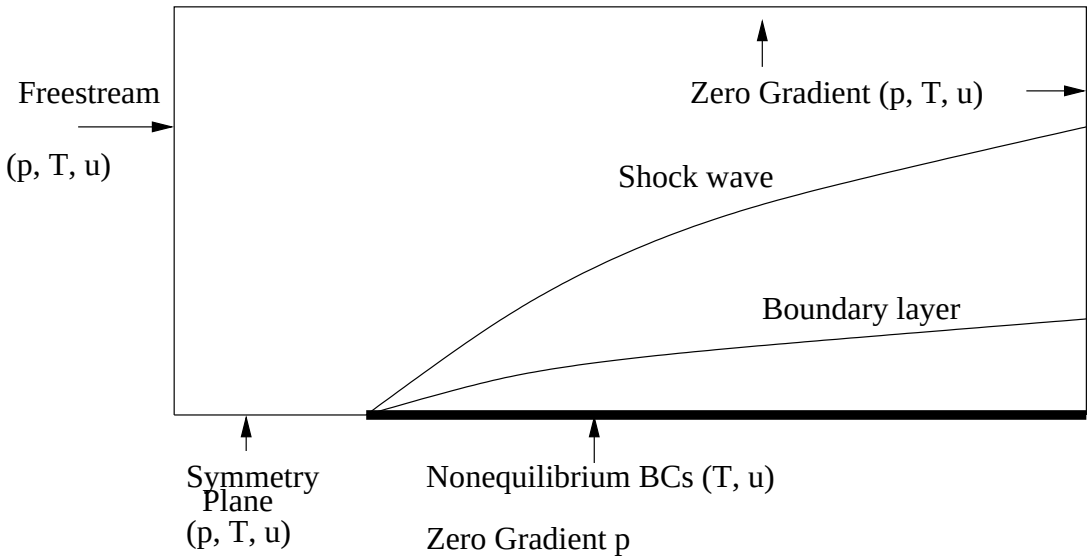

Figure 4.3: Numerical case setup for the flat plate problem.

the y direction, Δy, of the order of a freestream mean free path ($\lambda_\infty = 0.35$ mm). The computational meshes are listed in Table 4.3.

Table 4.3: Mesh sizes tested to obtain converged solutions.

Mesh	Δx (mm)	Δy (mm)
1	$1.7\lambda_\infty$	$3.6\lambda_\infty$
2	$0.9\lambda_\infty$	$1.8\lambda_\infty$
3	$0.6\lambda_\infty$	$1.2\lambda_\infty$
4	$0.4\lambda_\infty$	$0.9\lambda_\infty$

It is seen in Figure 4.4 that the surface pressure distributions are different for each of these four mesh sizes, especially near the leading edge $x/\lambda_\infty \leq 80$. The final mesh was selected on the basis of 5% difference of the peak value of surface pressure. The resolution distance from the plate tip versus cell size for the converged solution is shown in Figure 4.5. This distance shows that the flow has to pass through about 50 boundary faces to reach the spatial convergence.

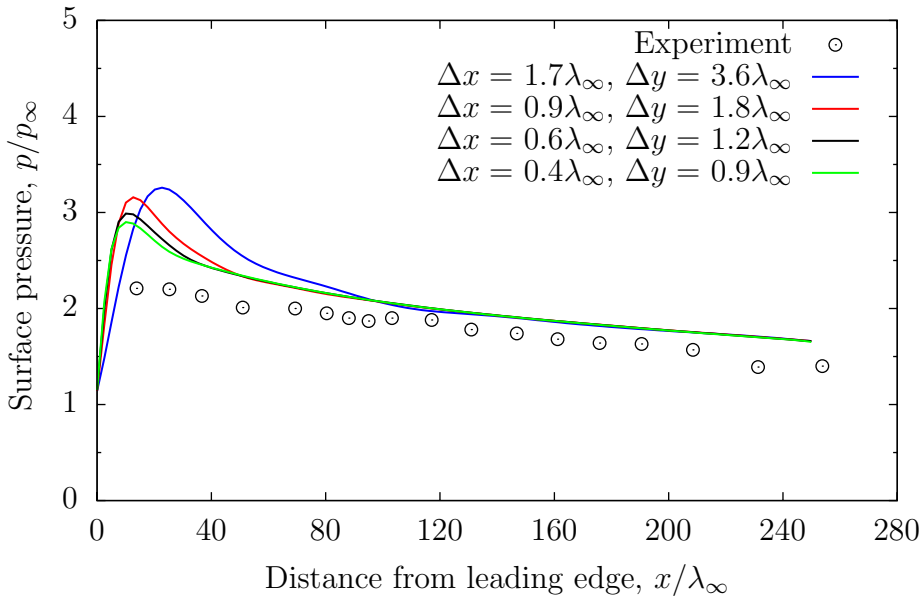

Figure 4.4: The surface pressure distribution along the flat plate for different mesh spacings Δx and Δy.

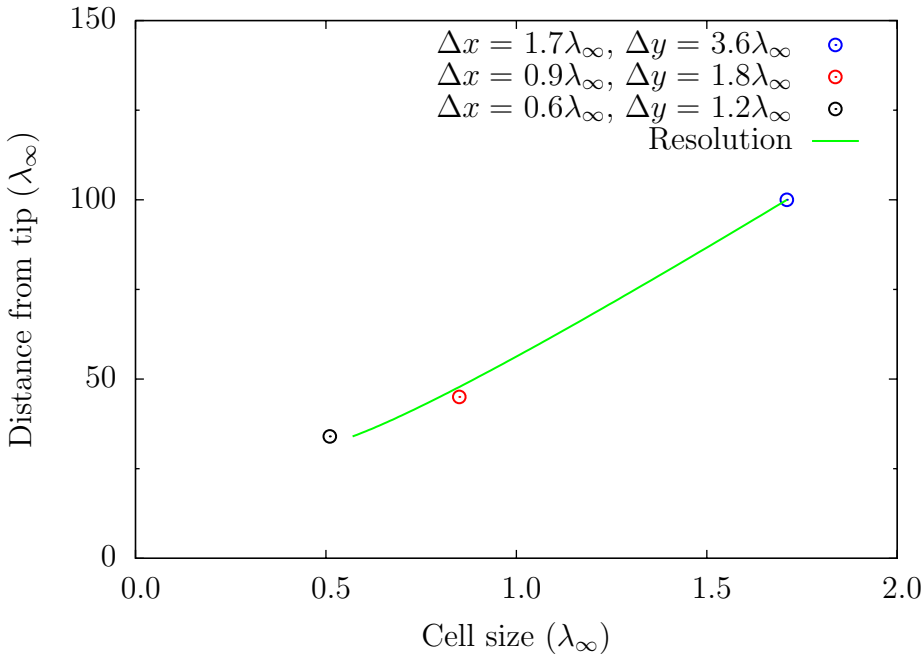

Figure 4.5: Resolution of mesh sensitivity.

A convergence solution indicates the appropriate mesh size is Δx =0.4λ_∞ and Δy =0.9λ_∞. Similar investigations are done for the other cases to find the final mesh for the convergence solution. The final mesh sizes of the cases are shown in Table 4.4.

Table 4.4: Final mesh sizes required to obtain converged solutions.

	Δx (mm)	Δy (mm)
Becker [46]	$0.1\lambda_\infty$	$0.1\lambda_\infty$
Metcalf *et al.* [53]	$0.4\lambda_\infty$	$0.9\lambda_\infty$
Vidal *et al.* [54]	$0.5\lambda_\infty$	$1.3\lambda_\infty$
Becker and Boylan [55]	$0.05\lambda_\infty$	$0.1\lambda_\infty$
Lengrand *et al.* [56]	$0.1\lambda_\infty$	$0.1\lambda_\infty$

4.5.3 Transport properties

Dynamic viscosity is calculated by Sutherland's law for all simulations of the flat plate cases. The coefficient of thermal conductivity is then computed from the standard equation (2.31). A calorically perfect gas is considered for all simulations of the flat plate cases. The values A_S, T_S needed for equation (2.30), R, γ and Pr for all flat plate cases are given in Tables 4.5 and 4.6.

Table 4.5: Coefficients of transport properties R, γ and Pr [24].

	R ($m^2s^{-2}K^{-1}$)	γ	Pr	Gas
Becker [46]	208.1	1.67	0.67	Argon
Metcalf *et al.* [53]	296.8	1.40	0.71	Nitrogen
Vidal *at al.* [54]	287.0	1.40	0.74	Air
Becker and Boylan [55]	287.0	1.40	0.74	Air
Lengrand *et al.* [56]	296.8	1.40	0.71	Nitrogen

Table 4.6: Coefficients of A_S, T_S needed for equation (2.30) from Table 2.1.

	A_S (Pa.s $K^{-1/2}$)	T_S (K)
Becker [46]	1.93×10^{-6}	142
Metcalf *et al.* [53]	1.41×10^{-6}	111
Vidal *at al.* [54]	1.46×10^{-6}	110.4
Becker and Boylan [55]	1.46×10^{-6}	110.4
Lengrand *et al.* [56]	1.41×10^{-6}	111

4.6 Computational results and comparison

In the flat plate case, we might choose L to be the length of the flat plate in calculating Kn, but its length has no effect on the slip near the tip. The flat plate case is in fact a simple test case for boundary conditions with Kn calculated through $x/\lambda = \mathrm{Kn}^{-1}$. In the figures below the CFD simulation, DSMC, and experimental results are plotted against $x/\lambda_\infty = \mathrm{Kn}^{-1}$.

Various coefficients (σ_u, σ_T, A_1 and A_2) were tested to obtain their desired values for reproducing hypersonic gas flows over the flat plate. A study of various coefficients was conducted for all the flat plate cases. Here, the results of Metcalf *et al.*'s case [53] are presented as an illustration.

4.6.1 Metcalf *et al.*'s case (a), $T_w = 77$ K [53]

Simulations were run with $\sigma_u = \sigma_T = 1.0$, 0.8 and 0.7, and also different accommodation coefficient values $\sigma_u = 0.7$ and $\sigma_T = 1.0$ in the Maxwell/Smoluchowski conditions. For surface pressure, the values $\sigma_u = 0.7$ and $\sigma_T = 1.0$ give reasonable agreement with experimental data for $x/\lambda_\infty \geq 15$ (i.e. $Kn \leq 0.067$), as seen in Figure 4.6. For surface gas temperature, the values $\sigma_u = \sigma_T = 0.8$ give good agreement with experimental data for $x/\lambda_\infty \geq 50$ (i.e. $Kn \leq 0.02$), the values $\sigma_u = 0.7$ and $\sigma_T = 1.0$ give good agreement with experimental data at the leading-edge of the flat plate for $x/\lambda_\infty \leq 50$ (i.e. $Kn \geq 0.02$), as shown in Figure 4.7.

For the slip velocity, it is seen that the reduction of the values σ_u and σ_T will increase the slip velocity, as seen in Figure 4.8. In the simulation for the case with $\sigma_u = \sigma_T = 0.7$ and the case with $\sigma_u = 0.7$ and $\sigma_T = 1.0$, the slip velocity is nearly constant with different values σ_T.

From testing the Maxwell/Smoluchowski conditions, the value $\sigma_T = 1.0$ gives good results with experimental data of surface pressure. Therefore, this value will be retained for testing the second order slip condition to find the desired values of coefficients A_1 and A_2. As seen in Figure 4.9, no slip/jump boundary conditions overpredict the surface pressure. Various values of the coefficients A_1 and A_2 were tested. The values $A_1 = 1.5$ and $A_2 = 1.0$ give good agreement with experimental data of surface pressure and surface gas temperature at the tip of

the flat plate, as seen in Figure 4.10. The computational results of slip velocity with various values A_1 and A_2 are shown in Figure 4.11. When the value of either A_1 or A_2 increases, then the slip velocity will increase. The no slip/jump test overpredicts surface pressure. In this test, the gas temperature at the surface is equal to $T_w = 77$ K along the flat plate, as seen in Figure 4.10.

The values $\sigma_u = 0.7$ and $\sigma_T = 1.0$ in the Maxwell/Smoluchowski conditions and the values $A_1 = 1.5$, $A_2 = 1.0$ and $\sigma_T = 1.0$ in the second order slip/Smoluchowski conditions give good agreement with experimental data of surface pressure and surface temperature. It should, however, be noted that none of the boundary conditions tested here, with whatever values of the parameters, gives a good full-field prediction of both the pressure and temperature along the plate. These desired values will be tested now for other flat plate cases to ascertain whether or not they also perform well. The results are presented in the next sections.

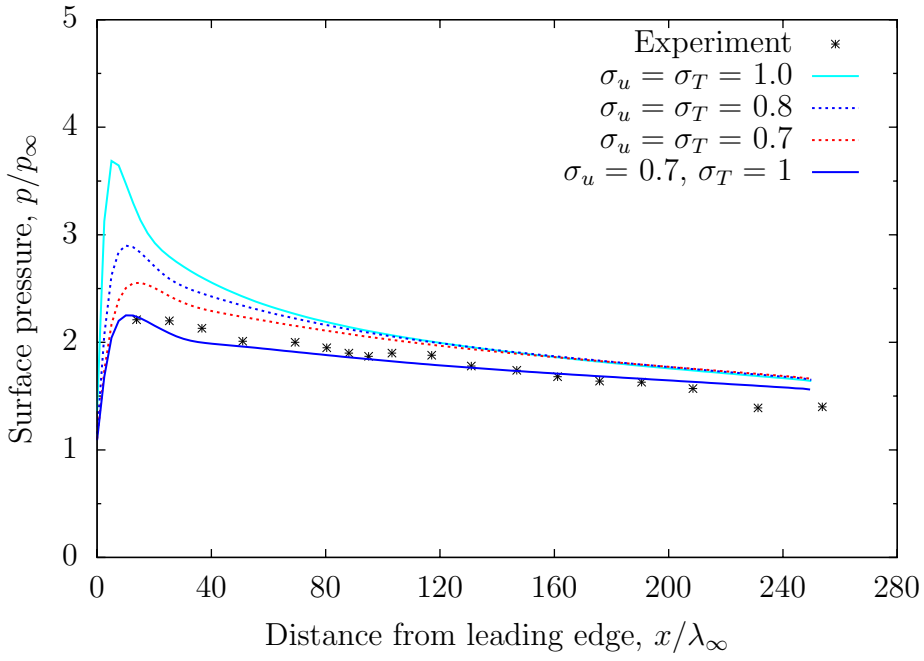

Figure 4.6: Metcalf *et al.*'s case [53] with Maxwell/Smoluchowski boundary conditions, the surface pressure distribution along the flat plate.

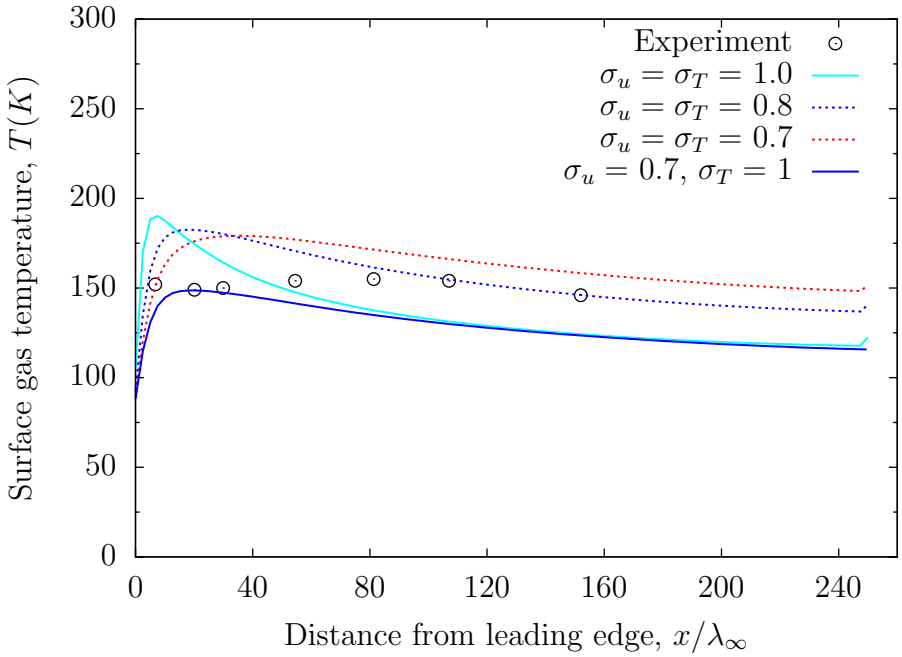

Figure 4.7: Metcalf *et al.*'s case [53] with Maxwell/Smoluchowski boundary conditions, the surface gas temperature along the flat plate.

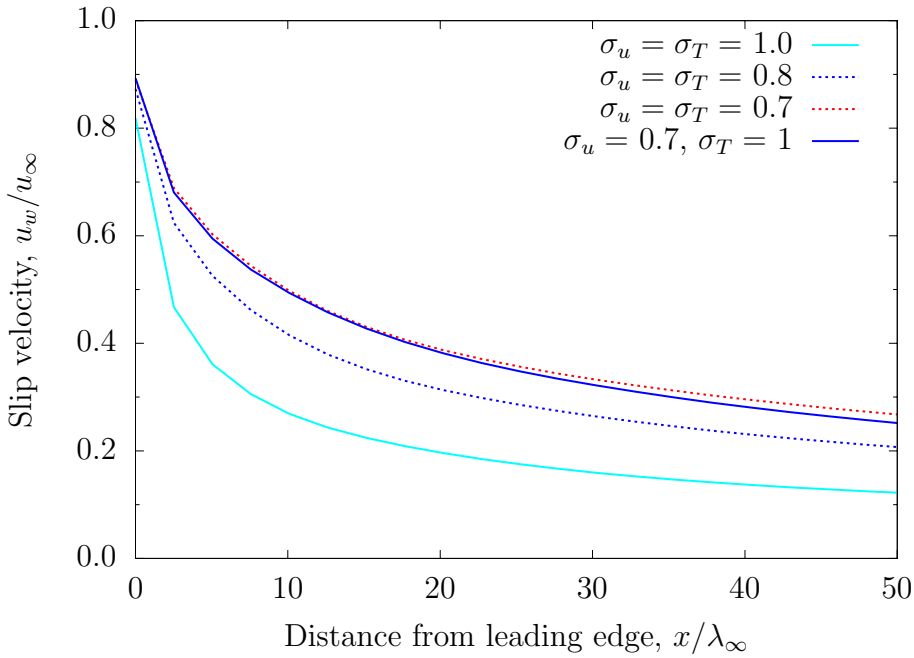

Figure 4.8: Metcalf *et al.*'s case [53] with Maxwell/Smoluchowski boundary conditions, the calculated slip velocity along the flat plate.

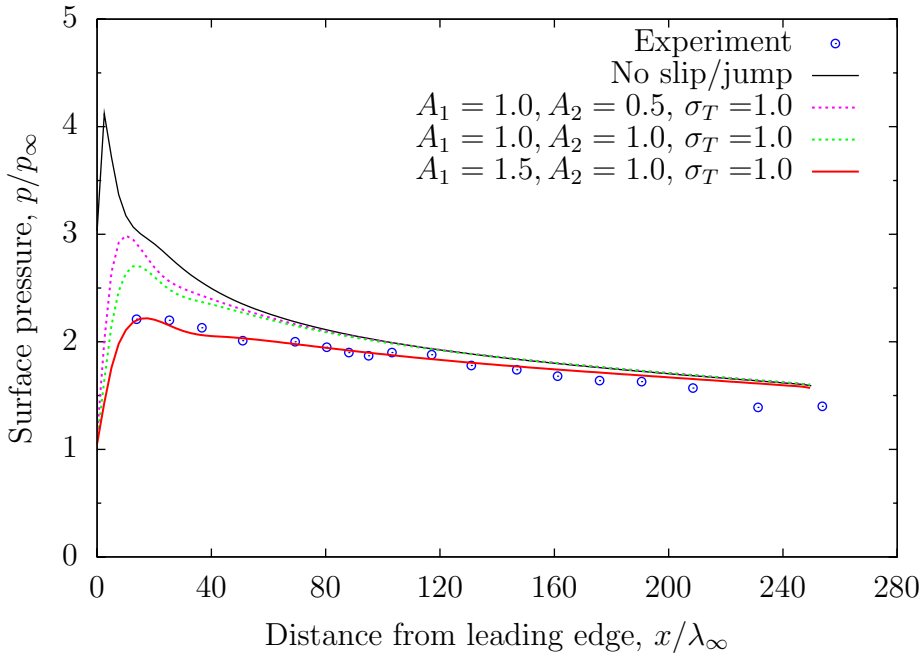

Figure 4.9: Metcalf *et al.*'s case [53] with second-order slip and Smoluchowski boundary conditions, the surface pressure distribution along the flat plate.

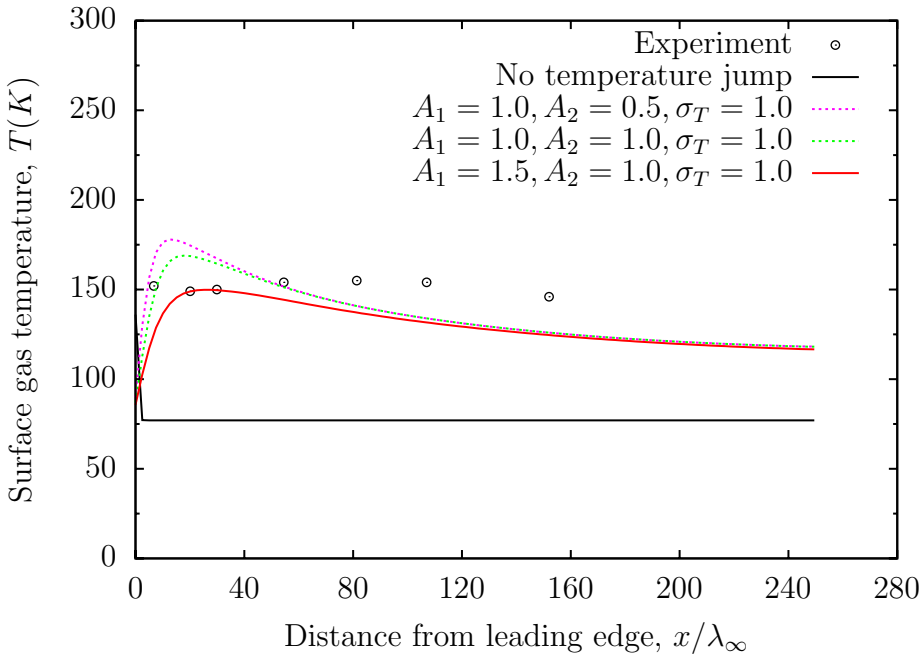

Figure 4.10: Metcalf *et al.*'s case [53] with second-order slip and Smoluchowski boundary conditions, the surface gas temperature along the flat plate.

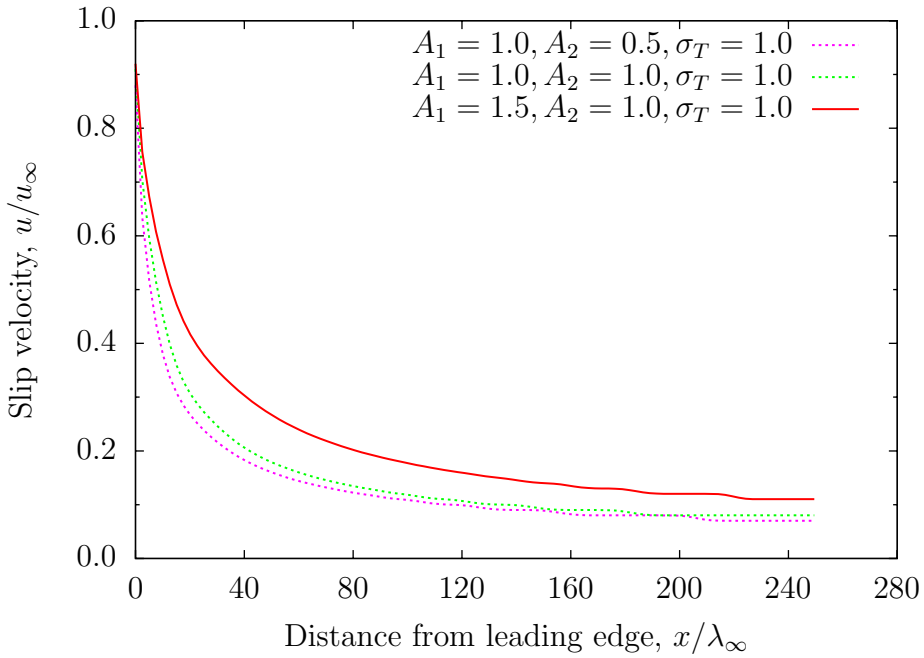

Figure 4.11: Metcalf *et al.*'s case [53] with second-order slip and Smoluchowski boundary conditions, the calculated slip velocity along the flat plate.

4.6.2 Vidal *et al.*'s case [54]

From this point the curves in the figures indicated by black, cyan and blue lines represent the results of the no slip/jump test, the results using $\sigma_u = \sigma_T = 1.0$, and the results using $\sigma_u = 0.7$ and $\sigma_T = 1.0$ in the Maxwell/Smoluchowski conditions, respectively. The red, green and the pink lines correspond to results using second-order slip/Smoluchowski conditions using the values $A_1 = 1.5, A_2 = 1.0$ and $\sigma_T = 1.0$, of results using the new conditions and of White's DSMC data, respectively.

In Vidal *et al.*'s case for surface pressure [54] shown in Figure 4.12, the results of the Maxwell/Smoluchowski conditions with $\sigma_u = 0.7$ and $\sigma_T = 1.0$; and the values $A_1 = 1.5$, $A_2 = 1.0$ and $\sigma_T = 1.0$ in the second-order slip/Smoluchowski conditions give good agreement with experimental data for $x/\lambda_\infty \geq 35$ (i.e. $Kn \leq 0.028$). The Maxwell/Smoluchowski conditions give better results than the second order/Smoluchowski conditions at the tip of the flat plate. However, the no slip/jump case overpredicts surface pressure.

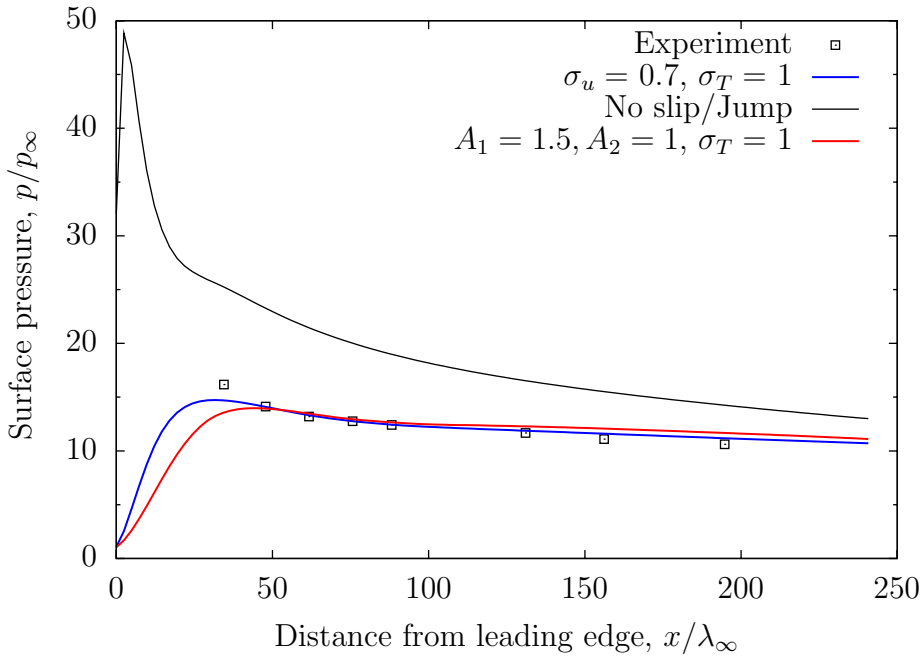

Figure 4.12: Vidal et al.'s case [54] with various boundary conditions, the surface pressure distribution along the flat plate.

4.6.3 Becker and Boylan's case [55]

Figures 4.13 and 4.14 compare the experimental data reported by Becker and Boylan [55] with the three previously described boundary conditions, with $\sigma_u = 0.7$ and $\sigma_T = 1.0$ in the Maxwell/Smoluchowski conditions, and the values $A_1 = 1.0$, $A_2 = 1.0$ and $\sigma_T = 1.0$ in the second-order/Smoluchowski conditions. It is seen that a) they both give good agreement with experimental data of surface pressure for $x/\lambda_\infty \geq 10$ (i.e. $Kn \leq 0.1$), b) they overpredict the slip velocity that is inferred by the experimentally measured surface pressure, and c) the results of the no slip/jump conditions massively overpredict surface pressure.

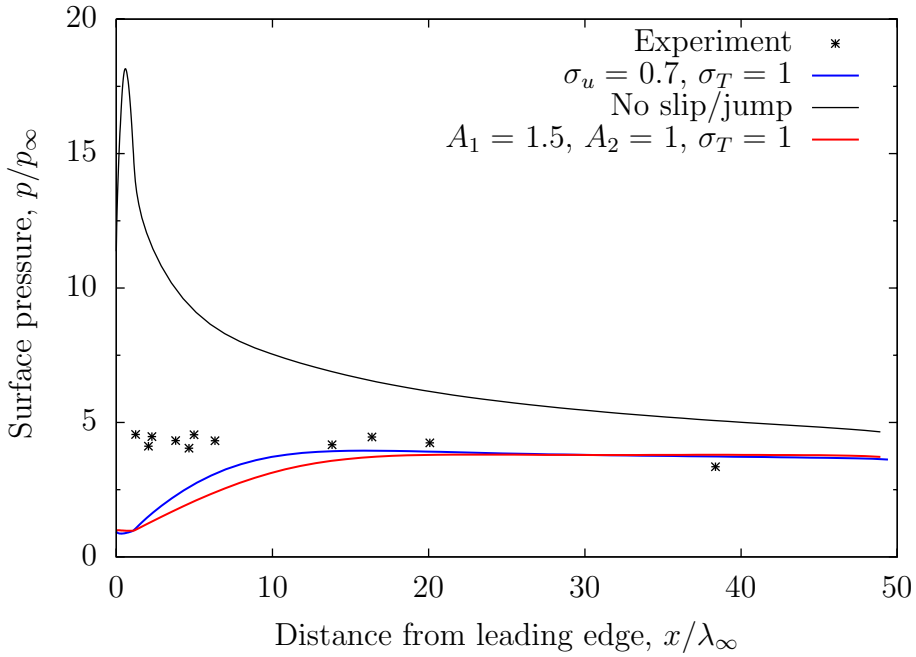

Figure 4.13: Becker and Boylan's case [55] with various boundary conditions, the surface pressure distribution along the flat plate.

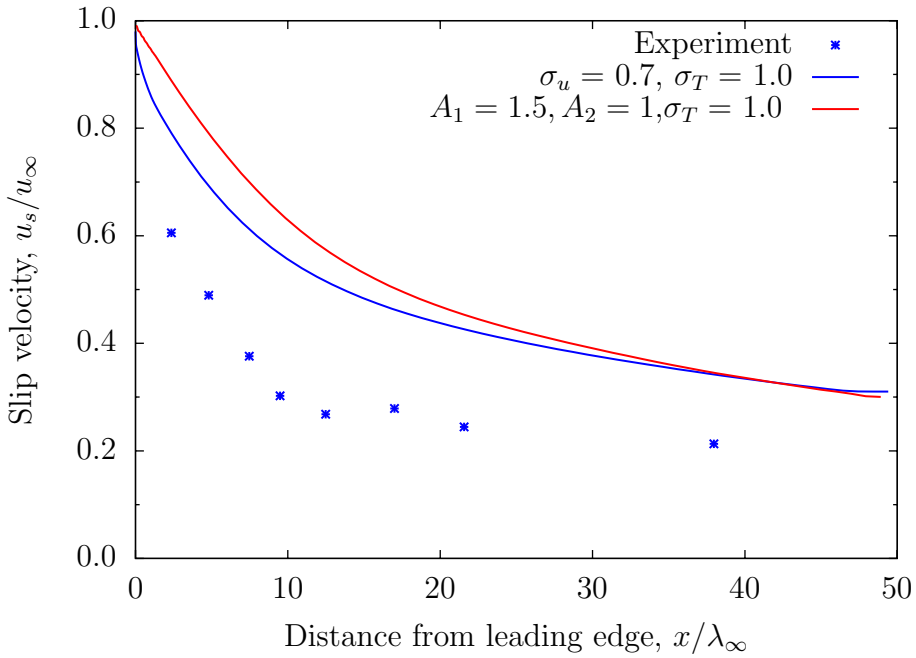

Figure 4.14: Becker and Boylan's case [55] with various boundary conditions, the slip velocity along the flat plate.

4.6.4 Metcalf *et al.*'s case (b), $T_w = 294$ K [53]

For the surface pressure, the Maxwell/Smoluchowski conditions with $\sigma_u = \sigma_T = 1.0$ generally do not give good agreement with experimental data, as seen in Figure 4.15. The results of the White DSMC data [60] with $\sigma_u = \sigma_T = 1.0$, CFD with the new boundary conditions, with the Maxwell/Smoluchowski conditions with $\sigma_u = 0.7$ and $\sigma_T = 1.0$, and with the second-order slip/Smoluchowski conditions with $A_1 = 1.5, A_2 = 1.0$ and $\sigma_T = 1.0$ are close together and give relatively good agreement with experimental data for $x/\lambda_\infty \geq 25$ (i.e. $Kn \leq 0.04$). However, the no slip/jump case overpredicts surface pressure.

Considering the surface temperature, the DSMC data [60] and the results with the Maxwell/Smoluchowski conditions with $\sigma_u = \sigma_T = 1.0$ do not give good agreement with experimental data towards the tip of the flat plate. By comparison, the results using the Maxwell/Smoluchowski conditions with $\sigma_u = 0.7$ and $\sigma_T = 1.0$, the second-order slip/Smoluchowski conditions with $A_1 = 1.5, A_2 = 1.0$ and $\sigma_T = 1.0$ and the new boundary conditions are close together and give good agreement with the experimental data, as seen in Figure 4.16. The gas temperature at the surface of the no-slip/jump test is equal to $T_w = 294$ K along the flat plate.

For slip velocity, the DSMC data are close to the results of the Maxwell/Smoluchowski conditions with $\sigma_u = \sigma_T = 1.0$. The results from these two cases are lower than the other CFD results, as seen in Figure 4.17. The results of the Maxwell/Smoluchowski conditions with $\sigma_u = 0.7$ and $\sigma_T = 1.0$ are close to the results using the new boundary conditions.

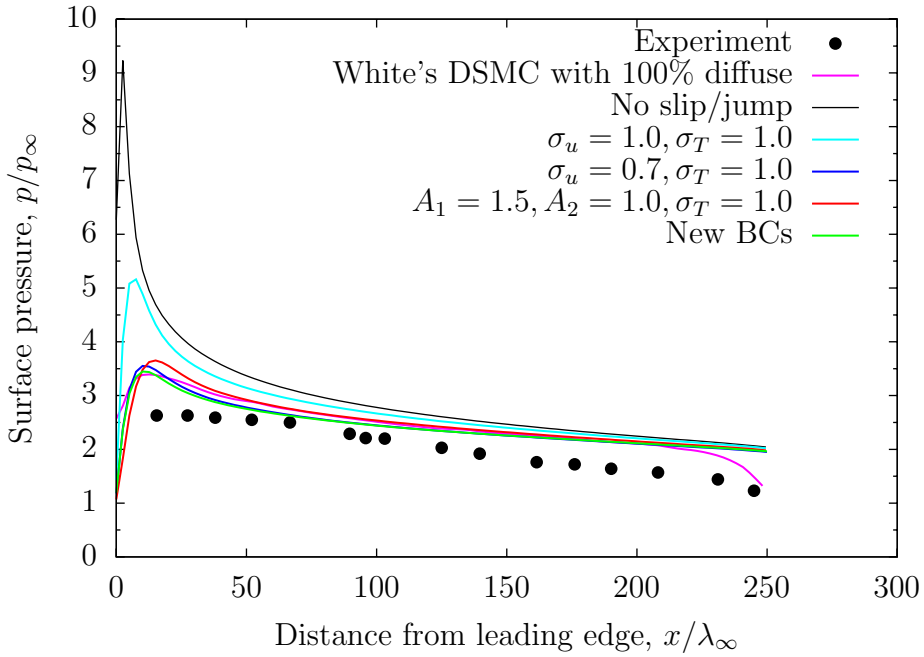

Figure 4.15: Metcalf *et al.*'s case [53] $T_w = 294K$, various boundary conditions, the surface pressure distribution along the flat plate.

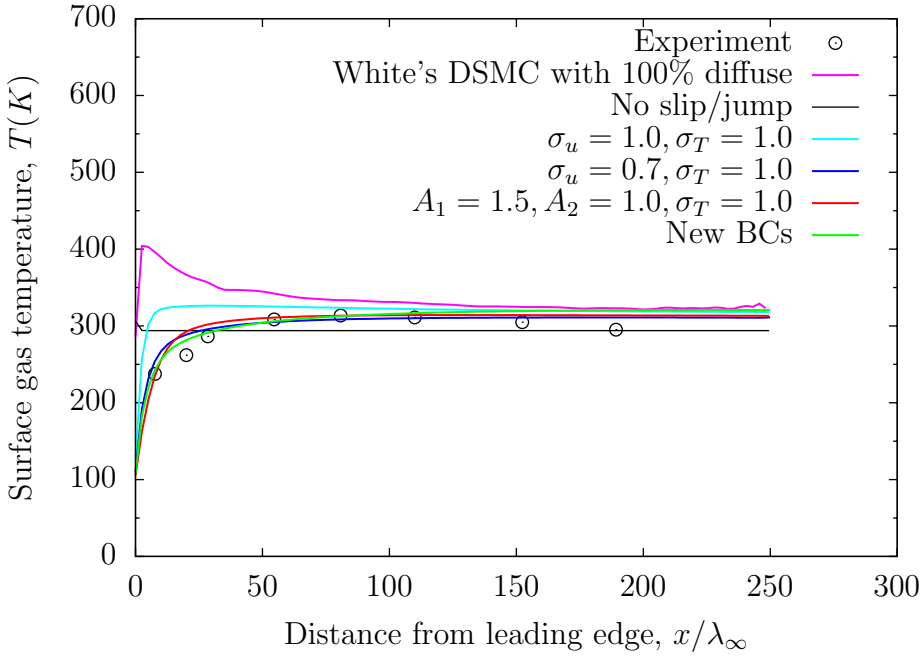

Figure 4.16: Metcalf *et al.*'s case [53] $T_w = 294K$, various boundary conditions, the surface gas temperature along the flat plate.

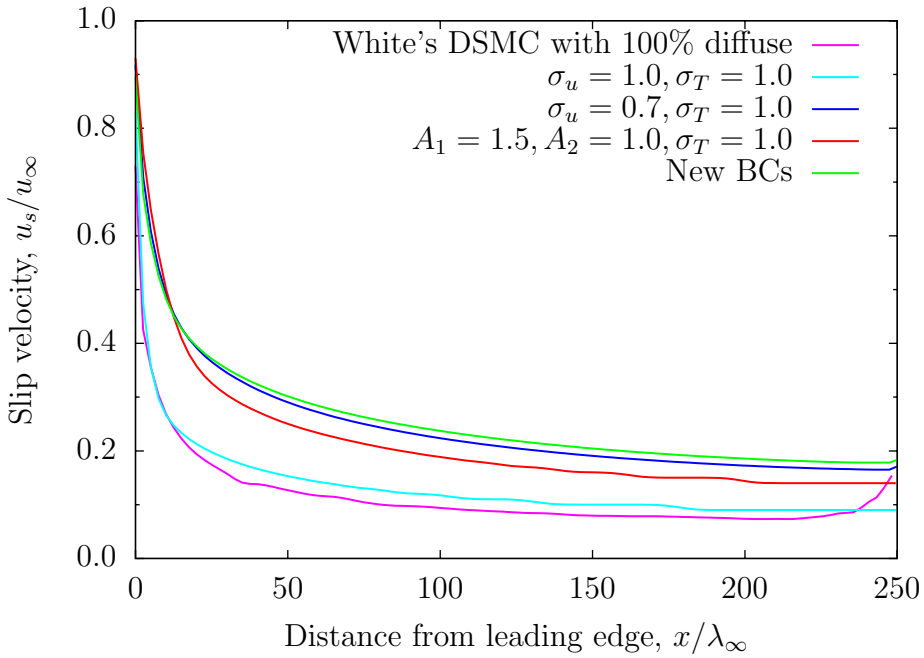

Figure 4.17: Metcalf *et al.*'s case [53] $T_w = 294K$, various boundary conditions, the computational slip velocity along the flat plate.

4.6.5 Becker's case [46]

In Becker's case for the surface pressure data, simulations are completed with different accommodation coefficient values: $\sigma_u = 0.7$ and $\sigma_T = 1.0$ in the Maxwell/Smoluchowski conditions, and the values $A_1 = 1.5$, $A_2 = 1.0$, and $\sigma_T = 1.0$ in the second order slip/Smoluchowski conditions give good agreement with experimental data for $x/\lambda_\infty \geq 18$ (i.e. $Kn \leq 0.055$), as seen in Figure 4.18. The results using the Maxwell/Smoluchowski conditions are better than those using the second-order slip/Smoluchowski conditions at the tip of the flat plate. The results using the new boundary conditions are a) in good agreement with experimental data, b) provide much better results than the Maxwell/Smoluchowski conditions with the values $\sigma_u = \sigma_T = 1.0$, and c) also close to the results using the Maxwell/Smoluchowski conditions with $\sigma_u = 0.7$ and $\sigma_T = 1.0$, and the second-order slip/Smoluchowski conditions with $A_1 = 1.5$, $A_2 = 1.0$ and $\sigma_T = 1.0$. On the other hand, the White DSMC data [60] with $\sigma_u = \sigma_T = 1.0$ do not give particularly good agreement with experimental data. The results of the no-slip/jump case strongly overpredict surface pressure, as seen in Figure 4.18.

As shown in Figure 4.19 for slip velocity, the White DSMC data do not give good agreement with experimental data and give the lowest slip value of any of the simulations used here. The values $\sigma_u = 0.7$ and $\sigma_T = 1.0$, and $A_1 = 1.5$, $A_2 = 1.0$ and $\sigma_T = 1.0$ give good agreement with experimental data. The Maxwell/Smoluchowski conditions with $\sigma_u = \sigma_T = 1.0$ undepredict the slip velocity while the new boundary conditions predict a higher slip velocity than the experimental data.

As seen in Figure 4.20 for the surface temperature, the predictions of the Maxwell/-Smoluchowski conditions with $\sigma_u = 0.7$ and $\sigma_T = 1.0$, and the second-order slip/Smoluchowski conditions with the values $A_1 = 1.5$, $A_2 = 1.0$, and $\sigma_T = 1.0$ are close together and lower than the results provided by the new boundary conditions. At the tip of the flat plate, a) there is a difference between the results of the Maxwell/Smoluchowski conditions with $\sigma_u = \sigma_T = 1.0$ and the other CFD results, and b) there is a relatively large difference between the DSMC data and the CFD results.

For completeness, the computed temperature field using the new boundary conditions is shown in Figure 4.21, which has a maximum temperature $T_{max} \approx 787$ K.

A comparison of velocity profiles in the surface-normal direction a) near the leading edge, x = 0.01 m, and b) near the trailing edge, x = 0.042 m, along the length of the flat plate $L = 0.055$ m, are presented in Figures 4.22 and 4.23. It is seen that there are differences between the DSMC and the CFD data in the Knudsen layer at the two locations. A near surface function such as that given in [59] might overcome this problem concerning hypersonic gas flows.

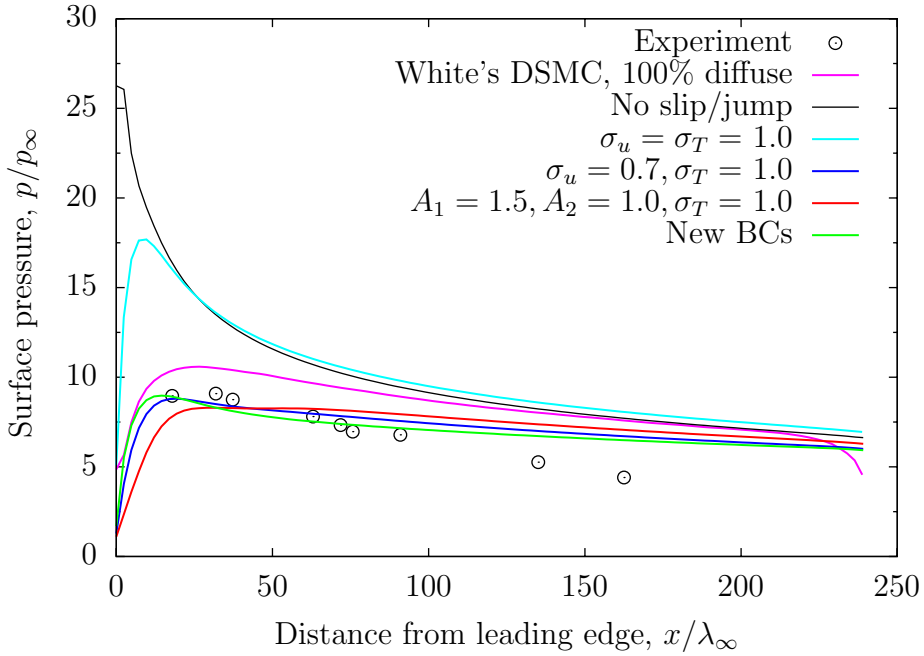

Figure 4.18: Becker's case [46] with various boundary conditions, the surface pressure distribution along the flat plate.

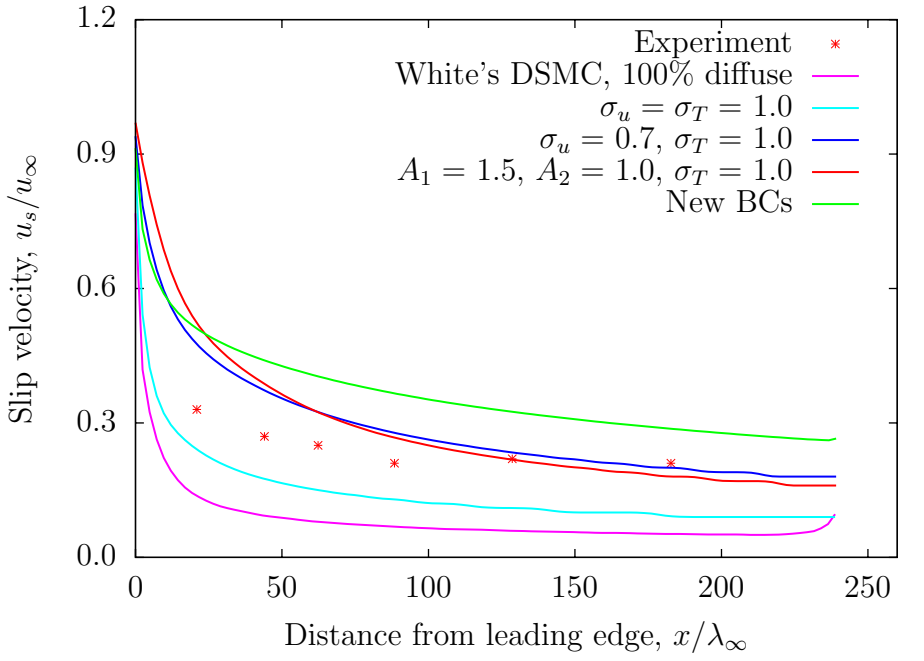

Figure 4.19: Becker's case [46] with various boundary conditions, the slip velocity along the flat plate.

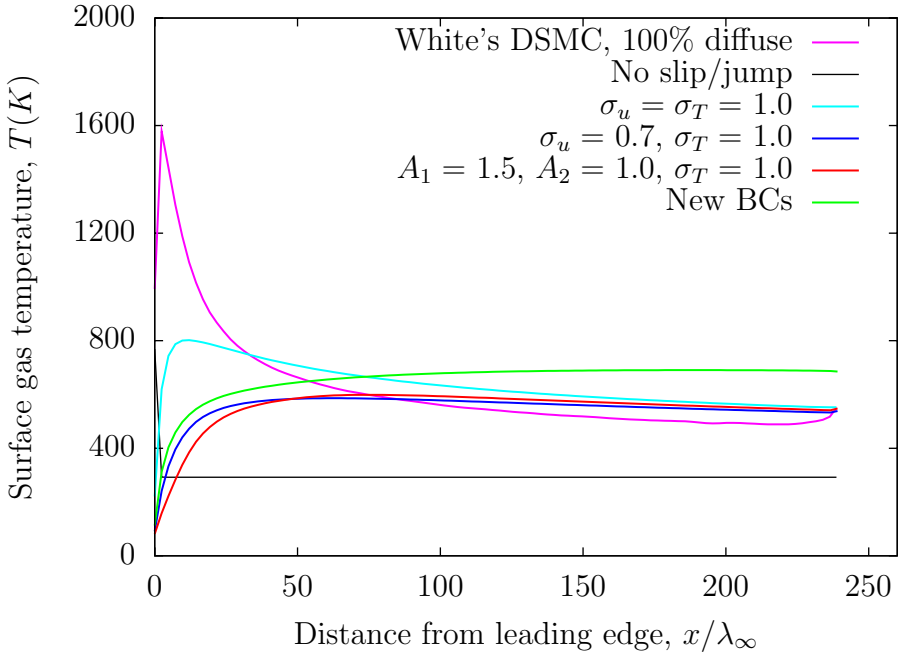

Figure 4.20: Becker's case [46] with various boundary conditions, the computational surface gas temperature along the flat plate.

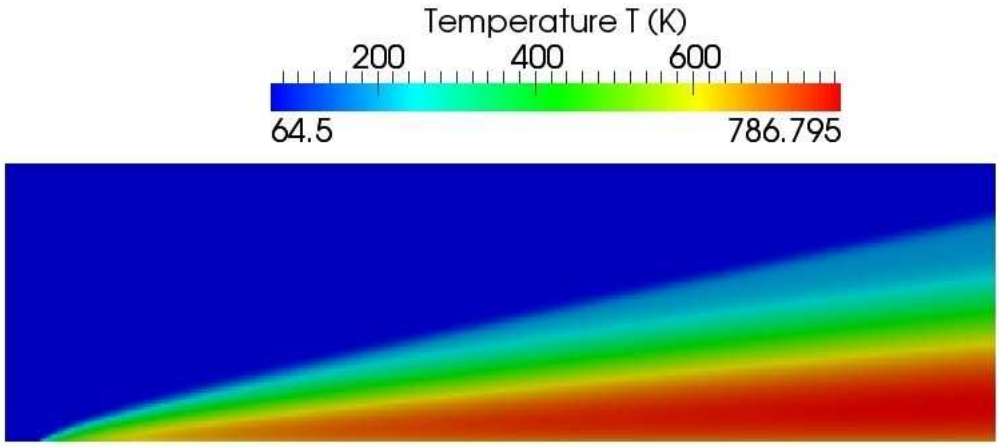

Figure 4.21: Becker's case [46] with the new boundary conditions, the temperature field.

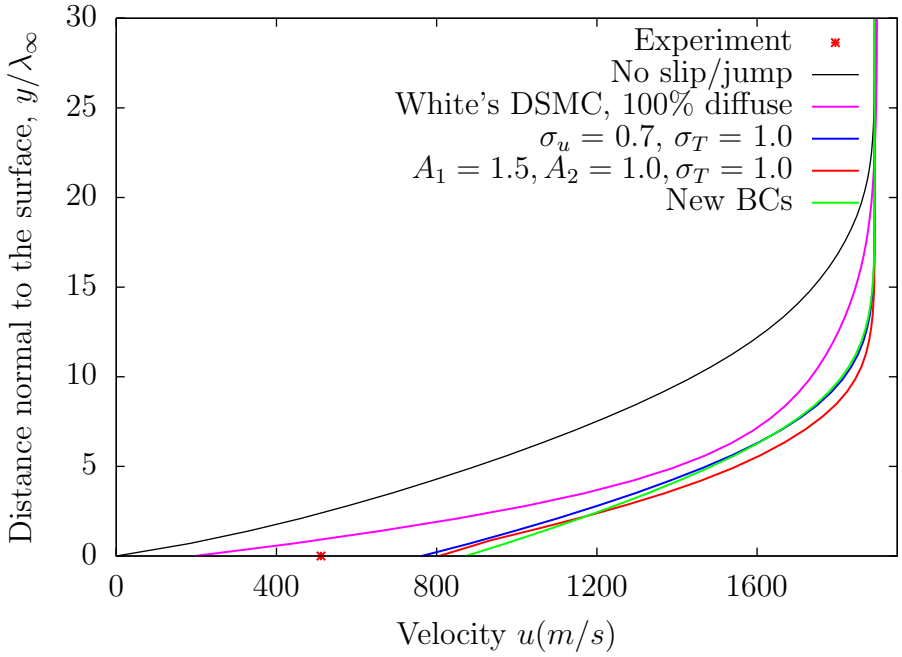

Figure 4.22: Becker's case [46] with various boundary conditions, the velocity distribution along the surface-normal line at x = 0.01 (m).

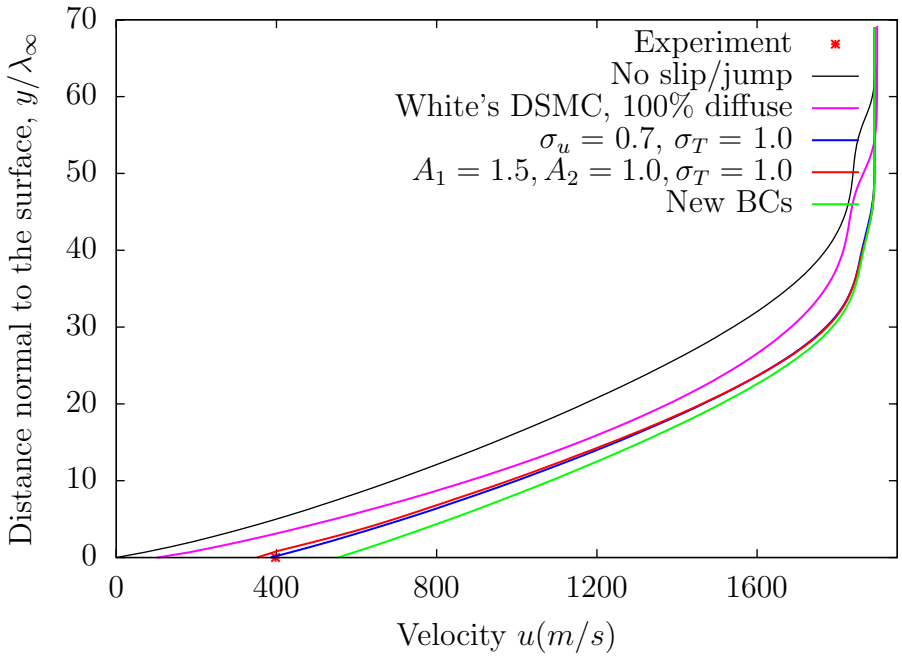

Figure 4.23: Becker's case [46] with various boundary conditions, the velocity distribution along the surface-normal line at x = 0.042 (m).

4.6.6 Lengrand *et al.*'s case [56]

In the case described by Lengrand *et al.*, the no slip/jump conditions over-predict surface pressure, as seen in Figure 4.24. The results using the new boundary conditions give a) good agreement with experimental data of surface pressure for $x/\lambda_\infty \geq 10$ (i.e. $Kn \leq 0.1$), b) much better results than the Maxwell/Smoluchowski conditions with $\sigma_u = \sigma_T = 1.0$ and c) good agreement with the results of the Maxwell/Smoluchowski conditions with $\sigma_u = 0.7$ and $\sigma_T = 1.0$ and the second order slip/Smoluchowski conditions with the values $A_1 = 1.5$, $A_2 = 1.0$ and $\sigma_T = 1.0$.

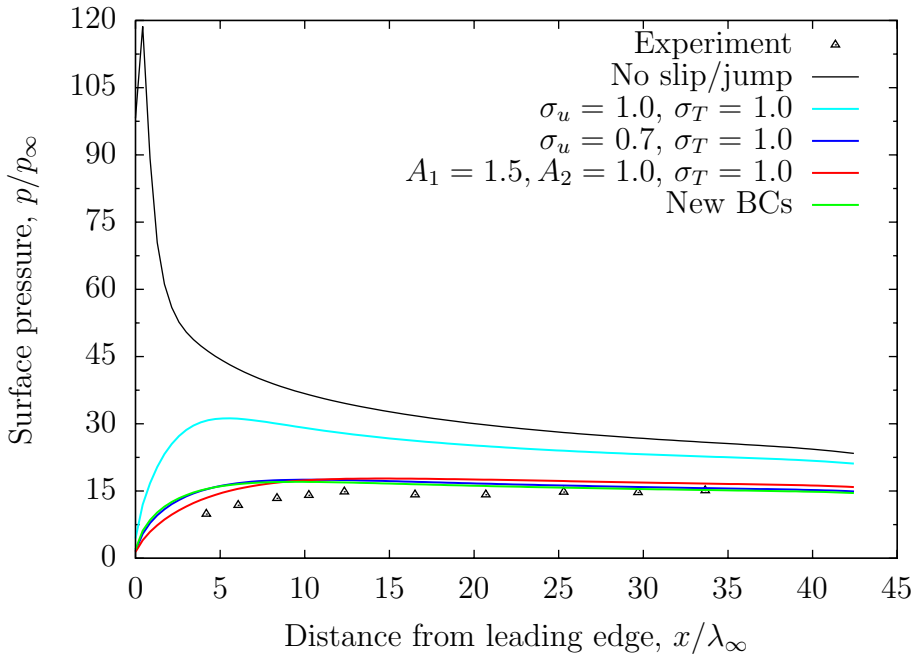

Figure 4.24: Lengrand *et al.*'s case [56] with various boundary conditions, the surface pressure distribution along the flat plate.

4.7 Summary and discussion

In this chapter, six flat plate cases were chosen for simulations with various working gases such as argon, nitrogen and air, various values of tangential σ_u and thermal σ_T accommodation coefficients in the Maxwell/Smoluchowski conditions, and vairous first A_1 and second A_2 order terms in the second order slip condition. For surface pressure, the values $\sigma_u = 0.7$ and $\sigma_T = 1.0$, and $A_1 = 1.5$, $A_2 = 1.0$ and $\sigma_T = 1.0$ give generally good agreement with experimental data for all cases up

to $Kn \leq 0.1$. The value σ_T only affects the surface pressure, but does not affect the slip velocity. The results obtained show that the slip/jump conditions with the Navier-Stoke-Fourier model are appropriate in the range $0.01 \leq Kn \leq 0.1$.

The new boundary conditions give good agreement with experimental data of surface pressure in Becker's, Lengrand *et al.*'s and Metcalf *et al.*'s ($T_w = 294$ K) cases [46, 53, 56]. For a diatomic gas (nitrogen), the calculated slip velocity and surface gas temperature from the new conditions agree with the results using the Maxwell/Smoluchowski conditions and the second-order slip/Smoluchowski conditions with their desired coefficients ($\sigma_u = 0.7$, $A_1 = 1.5$, $A_2 = 1.0$ and $\sigma_T = 1.0$) while the argon gas does not provide such good agreement.

Considering the surface temperature, there is a large difference between the DSMC data and the results of the CFD method at the tip of the flat plate in Becker's case [46] with argon as working gas. For nitrogen gas in Metcalf *et al.*'s ($T_w = 294$ K) [53], compared with experimental data, the results of the new boundary conditions, the Maxwell/Smoluchowski, and the second order slip/Smoluchowski conditions with their desired coefficients, are much better than the DSMC data.

From the results obtained so far, it is seen that the second order slip condition is not much better than the conventional Maxwell slip condition used with the Navier-Stokes-Fourier equations in simulating hypersonic gas flows. By comparison, the results of the no-slip/jump test are unacceptable for simulating hypersonic gas flows.

Comparing the experimental data of surface pressure and temperature in Becker's and Metcalf *et al.*'s ($T_w = 294$ K) cases [46, 53], the new boundary conditions gave better results than those using the Maxwell/Smoluchowski slip/jump conditions and the White DSMC data [60] with $\sigma_u = \sigma_T = 1.0$, instead of varying the values σ_u and σ_T to obtain reasonable agreement. In the following chapters, the new boundary conditions continue to be tested for other geometries and their simulation results are compared with those using the Maxwell/Smoluchowski conditions with $\sigma_u = 0.7$ and $\sigma_T = 1.0$, the Maxwell/Smoluchowski conditions and the Lofthouse DSMC data [51, 52] with $\sigma_u = \sigma_T = 1.0$.

Chapter 5

Simulations of a circular cylinder in cross-flow

5.1 Introduction

In the previous chapter, rarefied hypersonic flows over a sharp-leading-edge flat plate were investigated. This chapter presents rarefied hypersonic flow simulations about a blunt body, in particular, a circular cylinder in cross-flow. From the conclusions obtained in Chapter 4, the second-order slip condition developed for a planar surface is no longer investigated. The Maxwell/Smoluchowski slip/jump conditions, with the values $\sigma_u = 0.7$ and $\sigma_T = 1.0$ obtained from the numerical simulations of the flat-plate case, are tested here for all the circular cylinder cases. The Maxwell/Smoluchowski slip/jump conditions are also simulated with the values $\sigma_u = \sigma_T = 1.0$, to compare with the Lofthouse DSMC data ($\sigma_u = \sigma_T = 1.0$) given in [51, 52] and the CFD results using the new slip/jump boundary conditions. In the cylinder case, the curvature effect in the velocity slip conditions presented in Chapter 3, is tested to investigate how it affects the near-surface properties. The no slip/jump test is also performed. In the cylinder case, the Knudsen number, Kn, is calculated as follows:

$$Kn = \frac{\lambda}{D}, \tag{5.1}$$

where D is the diameter of the cylinder.

5.2 Experimental arrangement

The experimental arrangement given in [62] consists of the principal equipment: 1) a heat stagnation chamber and conical nozzle for producing flow at the desired test conditions, 2) measuring equipment such as pressure transducers, heat transfer gauges, thermocouples, optical lenses and electron beam guns, 3) instrumentation for data acquisition, such as a spectrometer, PC and monochromator, and 4) other equipment such as coolant pipes and pumps. The installation and operation of the experimental system are the same as in the flat plate case presented in Figure 4.1, with flat plate replaced by the circular cylinder.

The surface pressure in experiments was measured using inductive pressure transducers connected to pressure orifices located around the perimeter of the cylinder. The principles of these measurements are the same as in the flat plate case described in detail in Chapter 4.

5.3 The Direct Simulation Monte-Carlo cases

Several researchers have successfully computed the hypersonic flow around a cylinder using the DSMC method. In the numerical model for simulating the circular cylinder flow by Lofthouse *et al.* [51, 52], molecular collisions are treated by the variable hard sphere (VHS) model, and gas-surface interaction is treated by Maxwell's model with an accommodation coefficient of 1. The VHS model is consistent with a power law viscosity/temperature relationship. The viscosity is calculated through equations (3.33) and (3.34), with the working gas as argon, the temperature exponent $\omega = 0.734$, reference diameter $d_{ref} = 3.595\times\ 10^{-10}$ m and reference temperature $T_{ref} = 1000$ K taken from [51, 52]. Then, the thermal conductivity is calculated through equation (2.31).

The surface boundary conditions used in the DSMC simulations for a cylinder case are given by equations (3.29), (3.30), (3.31) and (3.32).

5.4 Boundary conditions

In the present CFD simulations, boundary conditions are applied on the surface of the cylinder for the flow variables (T, $\mathbf{u}$). The boundary condition for the

pressure p at the surface is zero normal gradient. At the inflow boundary, the freestream conditions are maintained throughout the computational process. At the outflow boundary, fluid is allowed to leave the computing region; this condition specifies that the normal gradients of the flow variables (p, T, $\mathbf{u}$) vanish at that boundary. At the bottom boundary in front of and behind the cylinder, a symmetry condition is applied to all flow variables. A schematic diagram of the boundary conditions applied in the cylinder cases is shown in Figure 5.1. The cylinder angle is presented by Φ, with $0° \leq \Phi \leq 180°$. The flow conditions for the four test cases investigated are given in Table 5.1.

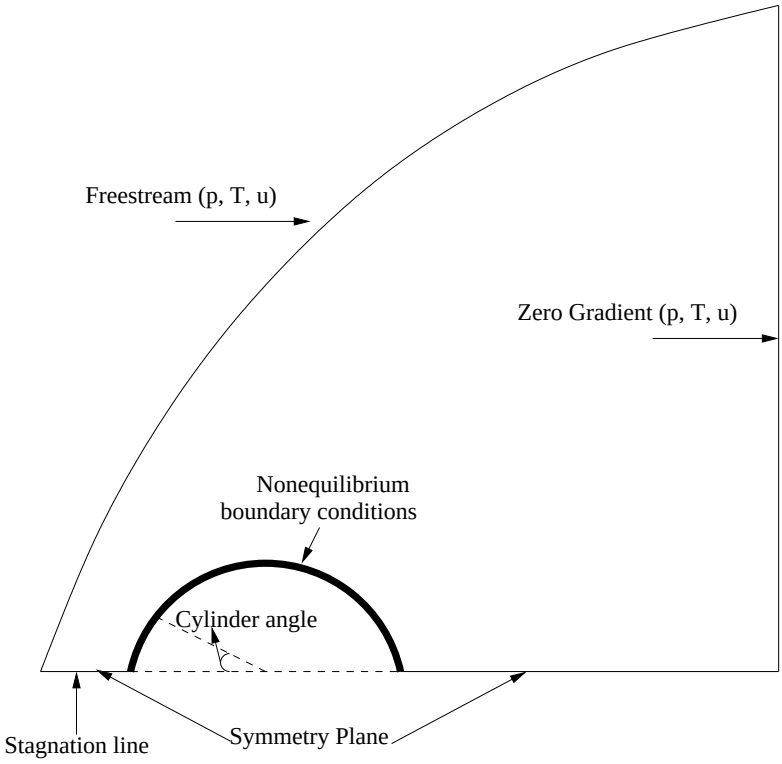

Figure 5.1: Numerical case arrangement for the cylinder in cross-flow.

Table 5.1: Flow conditions, Kn and diameters of the cases described in [51, 52, 62, 63].

	D (mm)	Ma	T_∞ (K)	p_∞ (Pa)	T_w (K)	Gas	Kn
DSMC [51, 52]	304.8	10	200	1.17	500	Argon	0.01
DSMC [51, 52]	304.8	10	200	0.047	500	Argon	0.25
Experiment [62]	76	6.47	241.5	627.5	278	Air	0.001
Experiment [63]	5.1	11.76	37.99	13.67	652.4	Air	0.0056

5.5 Numerical mesh

The computational mesh is constructed to wrap around the leading bow shock. For all the cases described in [51, 52, 62, 63], a mesh independence study was conducted. The final mesh encompassing the boundary layer has a linear grading in the surface-normal spacing over the number of cells near the surface. When a OpenFOAM nonuniform mesh grading is used, the cell sizes are calculated using a geometric progression. Along the length of grading cells l_c, if n_c cells are requested with a ratio of R_c between the last and first cells, the size of the smallest cell, Δy is given by [80]:

$$\Delta y = l_c \frac{r_c - 1}{\alpha_c r_c - 1}, \tag{5.2}$$

where r_c is the ratio between one cell size and the next which is given by [80]:

$$r_c = R_c^{\frac{1}{n_c - 1}}, \tag{5.3}$$

and

$$\alpha_c = \begin{cases} R_c & \text{for } R_c > 1 \\ 1 - {r_c}^{-n_c} + {r_c}^{-1} & \text{for } R_c < 1. \end{cases} \tag{5.4}$$

The smallest mesh sizes near the surface of the cases are shown in Table 5.2. A typical mesh of cells for cylinder simulations is shown in Figure 5.2.

Table 5.2: Linear grading of the mesh near the surface and total number of cells.

	Kn	n_c	l_c (mm)	Δx (mm)	Δy (mm)	Total cells
DSMC [51, 52]	0.01	25	100	2.40	$0.05 \rightarrow 0.25$	39 200
DSMC [51, 52]	0.25	50	100	2.40	$0.01 \rightarrow 2.5$	40 000
Experiment [62]	0.001	50	2.65	0.12	$0.0135 \rightarrow 0.135$	49 000
Experiment [63]	0.0056	25	0.31	0.08	$0.005 \rightarrow 0.025$	5000

5.6 Transport properties

A calorically perfect gas is considered, and the viscosity is calculated a) by Sutherland's law for experimental cases [62,63], and b) by the Power Law for the DSMC cases given in [51, 52]. The coefficient of thermal conductivity is then computed

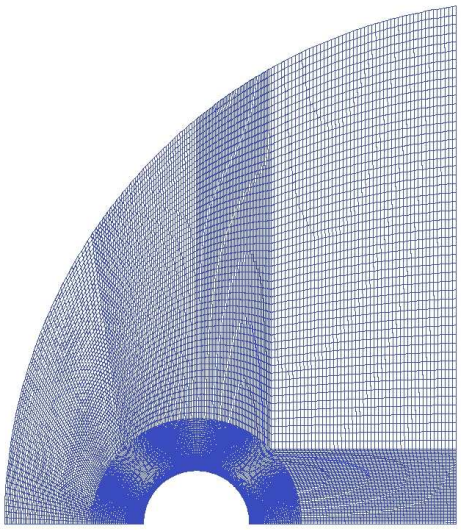

Figure 5.2: Computational mesh for the circular cylinder case, 40 000 cells.

through equation (2.31).

The Prandtl number, Pr, is assumed to be constant throughout the flow. The values $A_S = 1.46\times\ 10^{-6}$ Pa.s K$^{1/2}$, $T_S = 110.4$ K from Table 2.1 are adopted for Sutherland's equation (2.30) taken from Chapter 2. The values $A_P = 0.31\times\ 10^{-6}$ Pa.s K^s and $s = 0.734$ are adopted for the Power Law equation (2.29), where A_P is calculated equivalently from equations (3.33) and (3.34), with the values $\omega = 0.734$, $d_{ref} = 3.595\times\ 10^{-10}$ m, $T_{ref} = 1000$ K and $m = 6.63\times\ 10^{-26}$ kg given in [51, 52].

The values of R, γ and Pr of various working gases for calculation of the transport properties are taken from Table 4.5.

5.7 Simulation results

In the circular cylinder cases $Kn = 0.01, 0.0056$ and 0.25, the simulations are carried out for a half of cylinder ($0° \leq \Phi \leq 180°$) including forebody and the wake behind the cylinder. A wake region is a recirculating region, beginning from the separation point to the reattachment point, as shown seen in Figure 5.3 [64, 65]. At the separation point, then the flow starts to separate, which continues to flow downstream of the reattachment point, from that which turns back and

recirculates, as seen in Figure 5.3 [65]. For blunt bodies that are travelling at hypersonic speeds, the flow behind a bow shock in the stagnation region becomes subsonic and the temperature in this region is usually quite high. Then, the gas flow is often dominated by chemical reactions, such as dissociation, and it no longer behaves like a perfect gas [66,67,73]. Due to limited experimental data of the surface pressure in [62], the simulations of the cylinder case $Kn = 0.001$, are run for a quarter of cylinder, $0° \leq \Phi \leq 90°$.

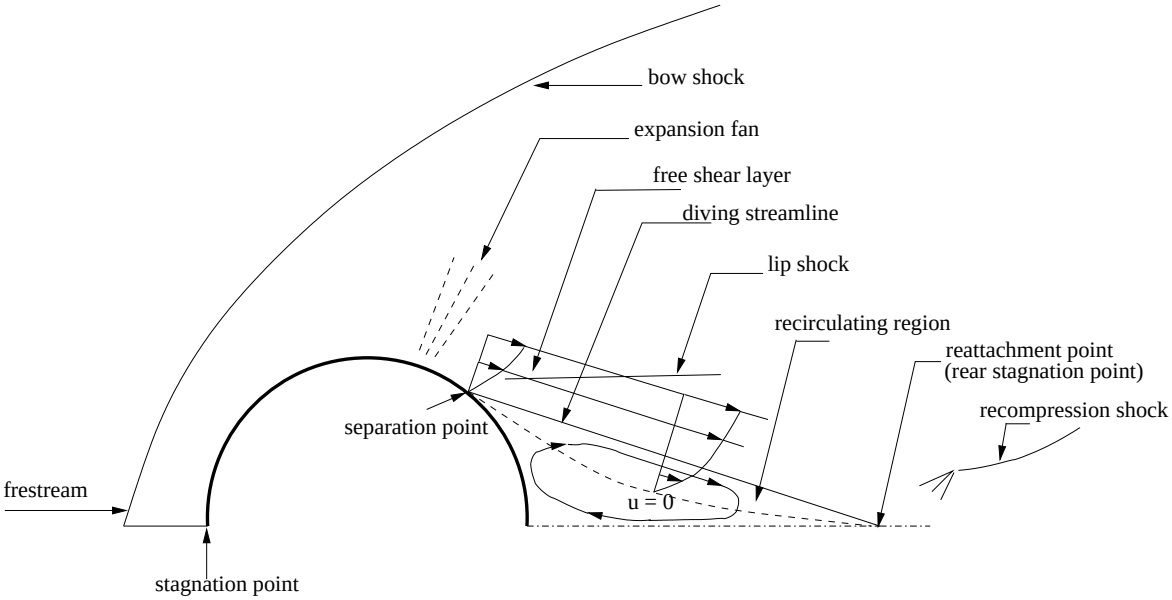

Figure 5.3: Schematic of the near wake behind a circular cylinder in cross-flow [65].

5.7.1 The DSMC cylinder case, $Kn = 0.01$

The no slip/jump conditions, the new slip/jump boundary conditions and the Maxwell/Smoluchowski conditions with the values $\sigma_u = 0.7$ and $\sigma_T = 1.0$, and $\sigma_u = \sigma_T = 1.0$ are tested here. All the slip boundary conditions are investigated with and without the curvature effect indicated by the term $\mathbf{\Pi}_{mc}$ in equations (3.11) and (3.37). In Figures 5.4 to 5.6, the thin lines represent the results without "curvature" and the thick lines the corresponding results with "curvature" effects.

Considering the surface pressure, all the CFD simulated results give good agreement with the DSMC data given in [51,52], as seen in Figure 5.4. However, all the

CFD tests predict a higher slip velocity than the DSMC data, as seen in Figure 5.5. The DSMC and CFD slip velocities increase gradually from $0° \leq \Phi \leq 135°$, reaching peak normalized values around the location $\Phi = 135°$ as follows: a) 0.21 and 0.23 using the Maxwell/Smoluchowski conditions ($\sigma_u = 0.7$ and $\sigma_T = 1.0$) with and without the curvature effect, respectively, b) 0.145 and 0.152 again using the Maxwell/Smoluchowski conditions ($\sigma_u = \sigma_T = 1.0$) with and without the curvature effect, respectively, c) 0.18 and 0.20 for the new conditions, with and without the curvature effect, respectively, and d) 0.09 for the DSMC data. For each slip condition in the CFD method, the curvature effect reduces the peak value of the slip velocity.

Considering the temperature jump, all the CFD results predict a higher temperature jump than the DSMC data for cylinder angles $0° \leq \Phi \leq 100°$, and the new conditions give the highest predictions, as seen in Figure 5.6. The gas flow begins to expand between $110° \leq \Phi \leq 130°$, and all the CFD temperature jumps decrease while the DSMC temperature jump increases. At the location of the separation point (around $\Phi = 130°$), the gas flow begins to enter the wake region. Then all the CFD temperature jumps rise towards $\Phi = 170°$ and give nearly constant finite values in $170° \leq \Phi \leq 180°$. However, the DSMC temperature jump decreases to the location $\Phi = 170°$ and is a nearly constant finite value between $170° \leq \Phi \leq 180°$. There are differences between the CFD temperature jumps and the DSMC temperature jump at the wake-surface. These differences may be explained by a) the inability of the laminar N–S–F solver to model the temperature jump at the wake-surface and b) the fact that the translational temperature jump in the DSMC method is calculated by the components of gas velocity and the slip velocity only, while the translational temperature jump in the CFD method is calculated by the normal gradient of gas temperature, and is independent of the gas velocity. The latter leads to the profile of the DSMC temperature jump being very similar to that for the slip velocity, as seen by comparison between Figures 5.5 and 5.6.

The curvature effect is important for predicting the slip velocity at the surface of the circular cylinder in cross-flow. However, the curvature effect in the slip conditions does not affect the temperature jump or the surface pressure, as seen in Figures 5.4 and 5.6.

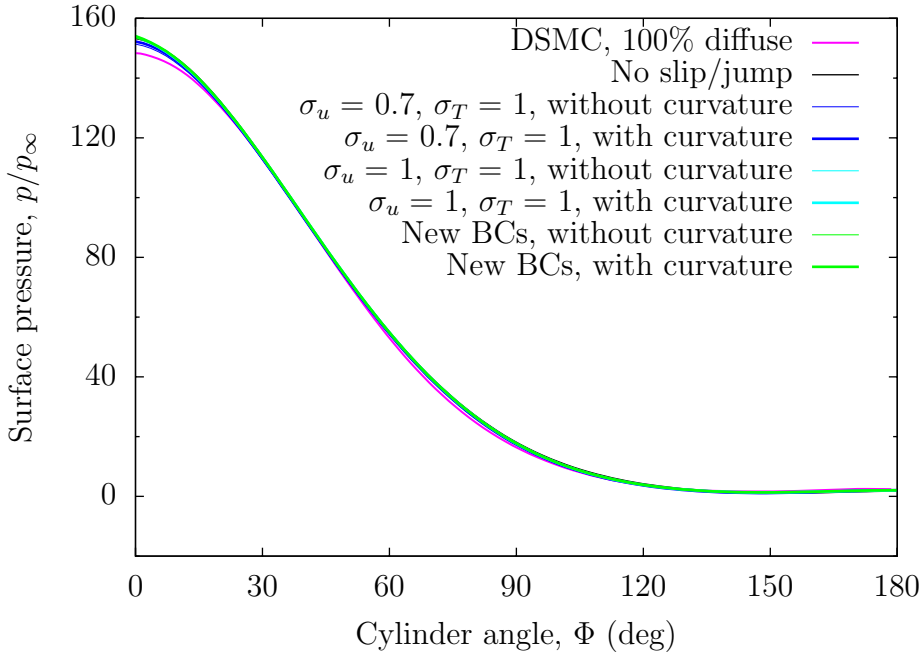

Figure 5.4: Surface pressure distribution around the cylinder surface, $Kn = 0.01$.

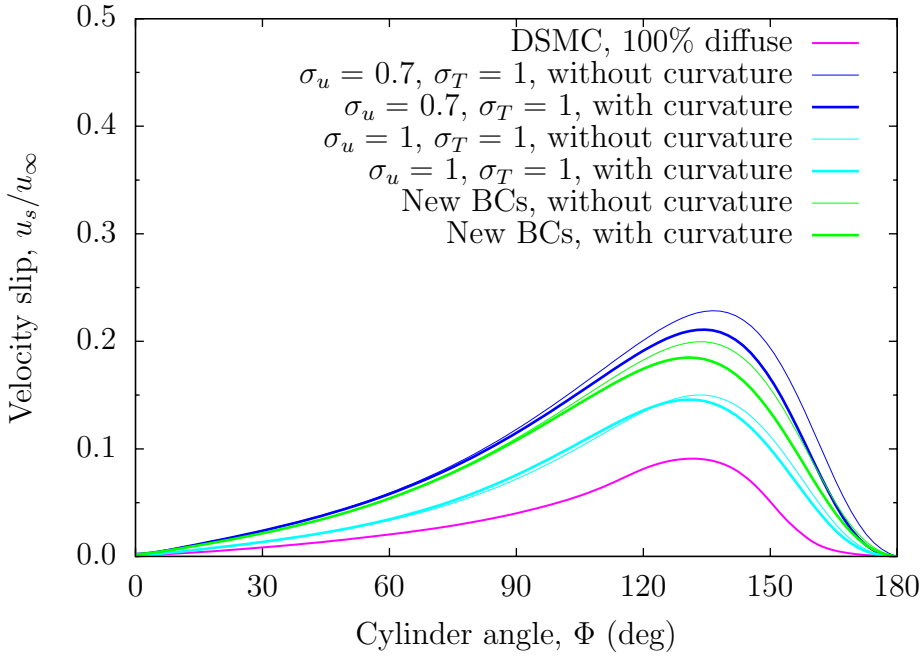

Figure 5.5: Computational slip velocity distribution around the cylinder surface, $Kn = 0.01$.

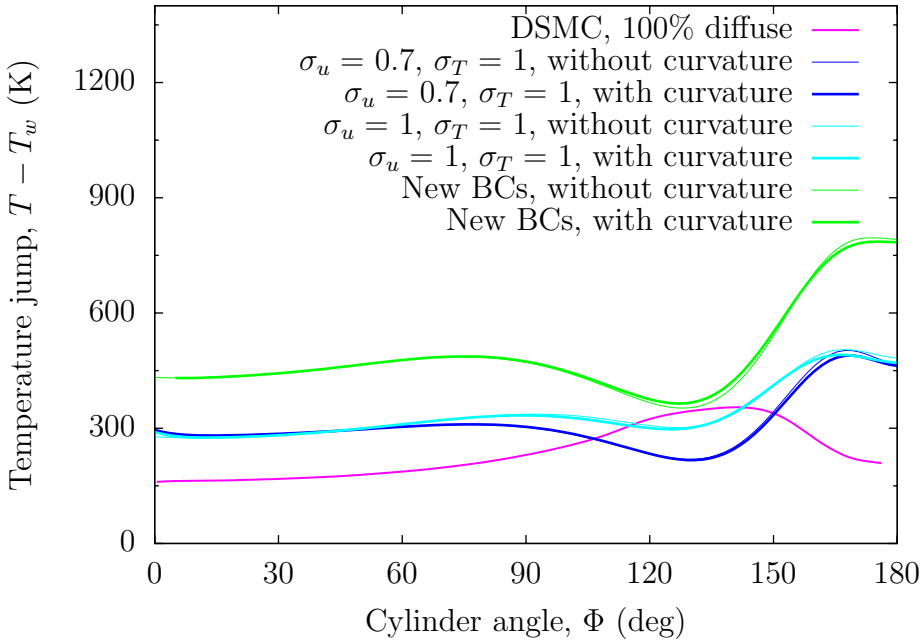

Figure 5.6: Computational temperature jump distribution around the cylinder surface, $Kn = 0.01$.

5.7.2 The DSMC cylinder case, $Kn = 0.25$

Figure 5.7 shows the DSMC and CFD simulation results for the surface pressure. It can be seen that there is no difference in using the Maxwell/Smoluchowski conditions with $\sigma_u = 0.7$ and $\sigma_T = 1.0$, and $\sigma_u = \sigma_T = 1.0$. For surface pressures at the stagnation point, the no slip/jump conditions give the highest normalized surface pressure of 172 while the new conditions predict lowest normalized pressure, 153. The normalized surface pressure at the stagnation point using the DSMC data and for the Maxwell/Smoluchowski condition are 161 and 165, respectively. In the region $0° \leq \Phi \leq 40°$, the Maxwell/Smoluchowski conditions and the no slip/jump conditions predict higher surface pressures than the DSMC data, while the new conditions predict values lower than those given by the DSMC data. As seen in Figure 5.7, for $\Phi = 40°$ to $\Phi = 180°$, the no slip/jump conditions and the new conditions are close to the DSMC data, while the Maxwell/Smoluchowski conditions are not.

Considering the simulations of the slip velocity, Figure 5.8, all the CFD slip velocities increase gradually from the location $\Phi = 0°$ to $\Phi = 95°$, and reach peak normalized values around the location $\Phi = 95°$, while the DSMC slip velocity

increases and reaches a peak normalized value at $\Phi = 130°$. The peak normalized values of slip velocity are a) 0.42 with the new conditions, b) 0.23 using the Maxwell/Smoluchowski conditions with $\sigma_u = 0.7$ and $\sigma_T = 1.0$, c) 0.20 for the Maxwell/Smoluchowski conditions with $\sigma_u = \sigma_T = 1.0$, and d) 0.17 for the DSMC data. After these reaching peak normalized values, the slip velocities of the CFD and the DSMC simulations decrease quickly to zero value. There are large differences between the DSMC slip velocity and CFD slip velocities at this large Knudsen number, $Kn = 0.25$, as seen in Figure 5.8.

When the temperature jumps are considered, Figure 5.9, the new conditions predict the highest temperature jump, 4730 K at the stagnation point. For other simulations, the temperature jumps at this point are a) 500 K using the DSMC data, b) 1540 K using the Maxwell/Smoluchowski conditions with $\sigma_u = \sigma_T = 1.0$, and c) 1625 K for the Maxwell/Smoluchowski conditions with $\sigma_u = 0.7$ and $\sigma_T = 1.0$. Therefore, there is not much difference between the temperature jumps for the Maxwell/Smoluchowski conditions using the values of $\sigma_u = 0.7$ and $\sigma_T = 1.0$, and of $\sigma_u = \sigma_T = 1.0$. However, there are large differences between the CFD temperature jumps and the DSMC temperature jump. In the wake region ($125° \leq \Phi \leq 180°$), the DSMC temperature jump decreases while that for the CFD increases gradually. At such a large Knudsen number as this case, the wake region is more rarefied leading to the breakdown of the continuum hypothesis in the N–S–F equations. The profile of the DSMC temperature jump in Figure 5.9 is similar to that for the DSMC slip velocity in Figure 5.8.

Figure 5.10 shows the simulation results for the velocity varying with distance normal to the cylinder surface, at $\Phi = 90°$. There are considerable differences between the CFD results and the DSMC data in the Knudsen layer.

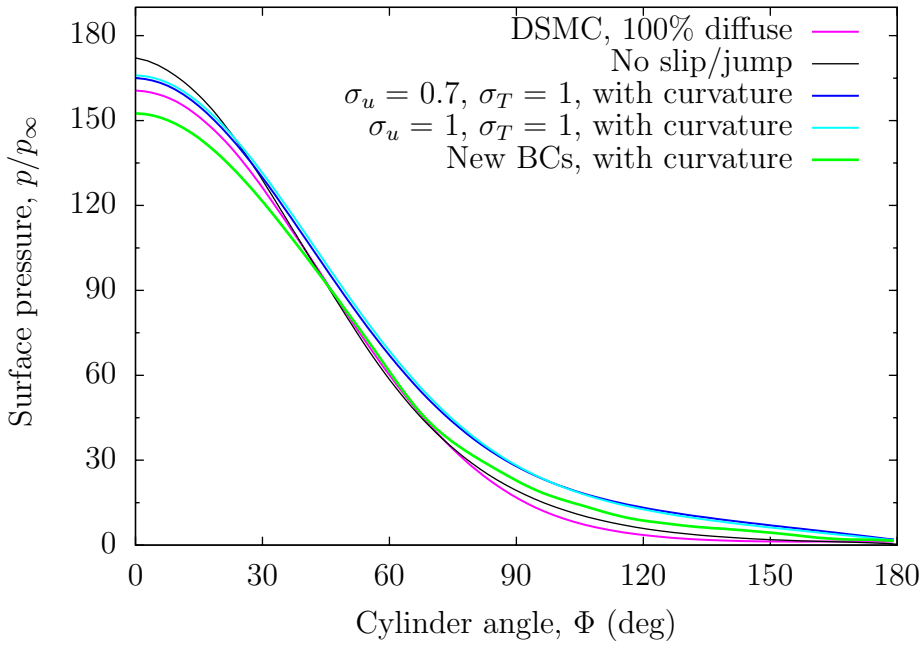

Figure 5.7: Surface pressure distribution around the cylinder surface, $Kn = 0.25$.

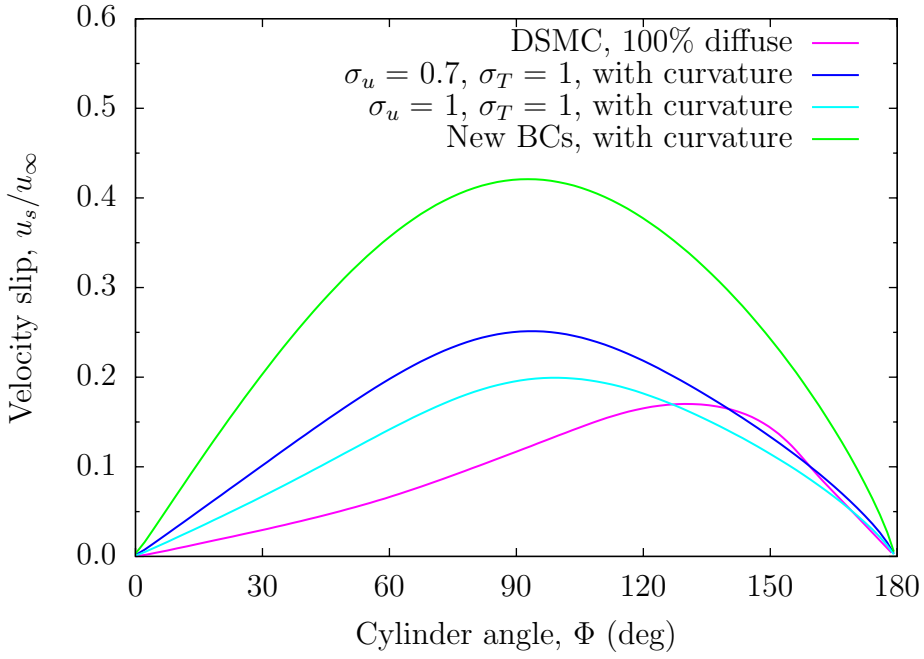

Figure 5.8: Computational slip velocity distribution around the cylinder surface, $Kn = 0.25$.

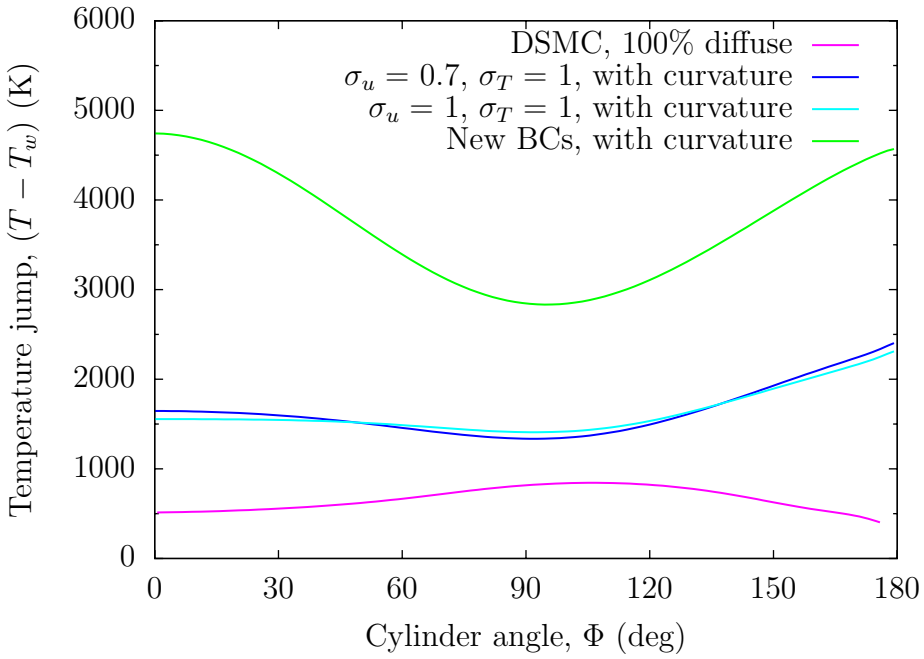

Figure 5.9: Computational temperature jump distribution around the cylinder surface, $Kn = 0.25$.

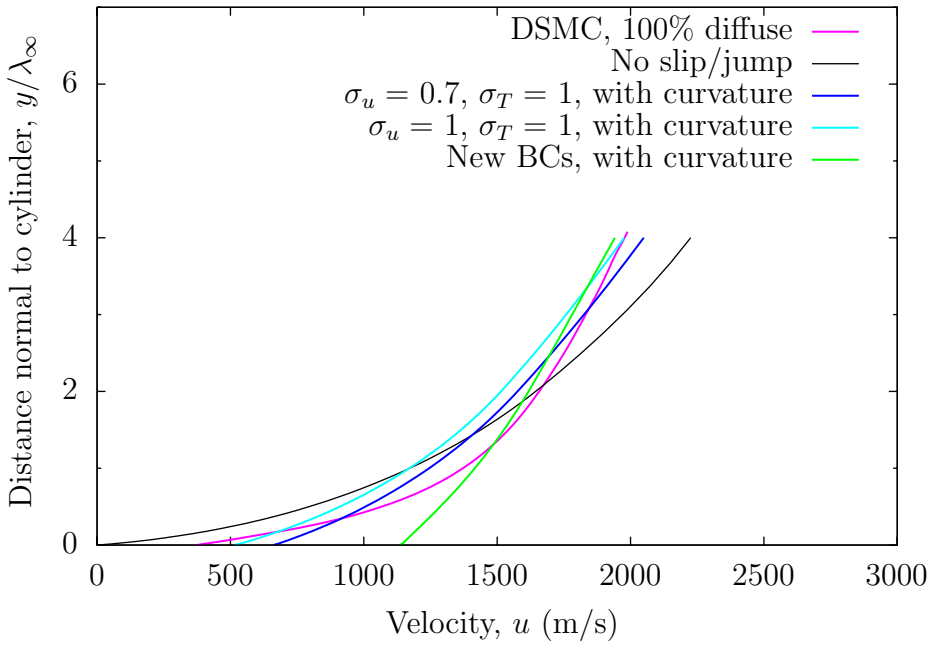

Figure 5.10: Computational velocity along a line normal to the surface at $\Phi = 90°$, $Kn = 0.25$.

5.7.3 Experimental cylinder case, $Kn = 0.0056$

Because the value of the heat of adsorption, D_e, for air is not available in the literature for the new boundary conditions, only the Maxwell conditions are tested with $\sigma_u = 0.7$ and $\sigma_u = 1.0$, and $\sigma_T = 1.0$ in the Smoluchowski jump condition. The no slip/jump condition test is also simulated. Due to the results obtained in Section 5.7.1, the slip conditions without the curvature effect were no longer investigated. At small Kn, all the simulation results show agreement with the experimental data of the surface pressure. However, at the forward stagnation point, $\Phi = 0°$, the simulation results predict slightly higher surface pressures than experimental data, as seen in Figure 5.11.

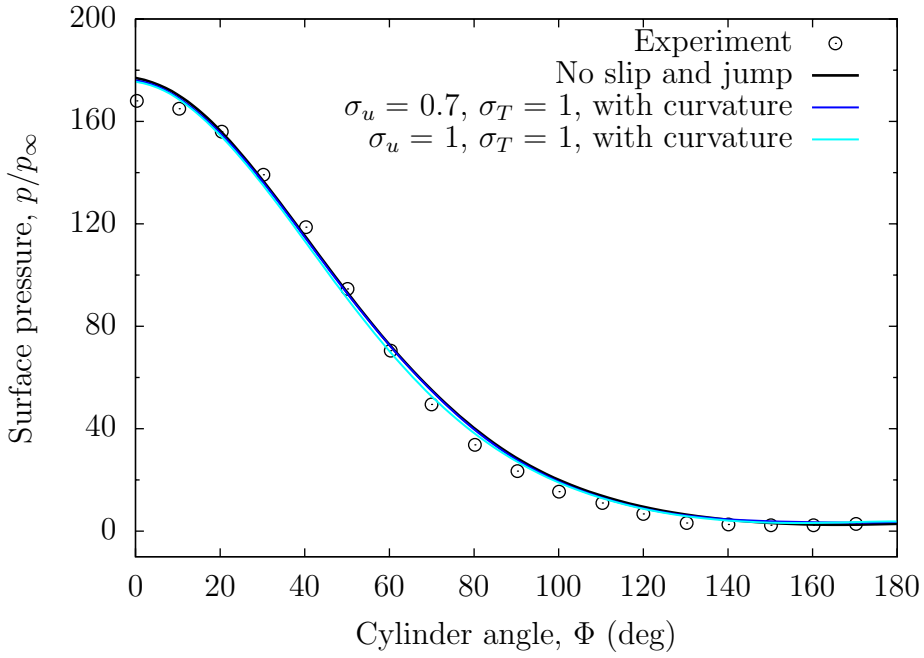

Figure 5.11: Surface pressure distribution around the cylinder surface, $Kn = 0.0056$.

5.7.4 Experimental cylinder case, $Kn = 0.001$

The same simulations were carried out for a smaller Kn value. All the simulation results again give reasonably good agreement with experimental data for the pressure along the cylinder surface, as seen in Figure 5.12. The bow shock predicted by the Maxwell/Smoluchowski conditions with the values $\sigma_u = 0.7$ and $\sigma_T = 1.0$ are somewhat thicker than the bow shock seen in experiment, as shown in Figure 5.13.

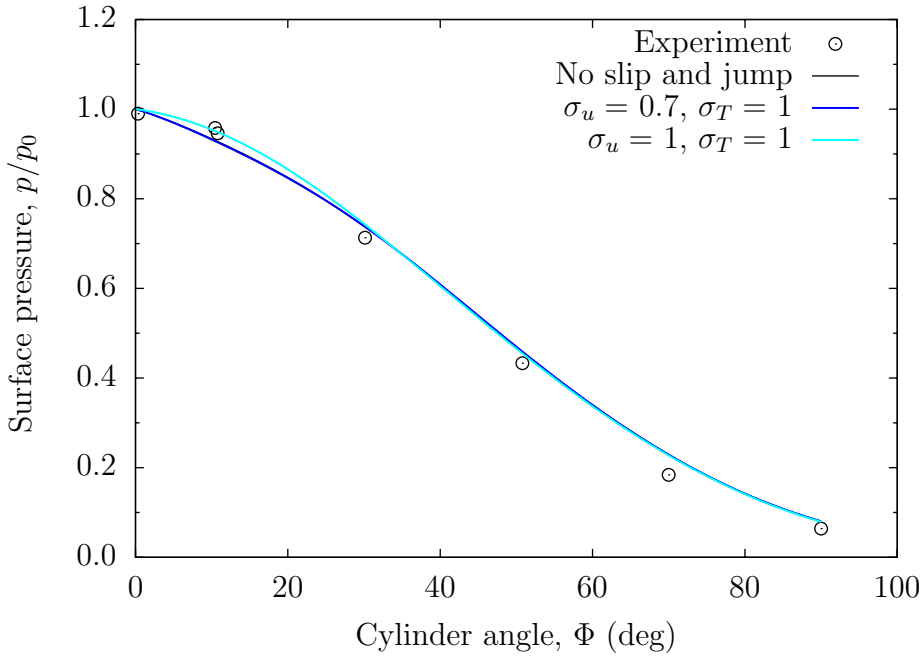

Figure 5.12: Surface pressure distribution along the cylinder, $Kn = 0.001$.

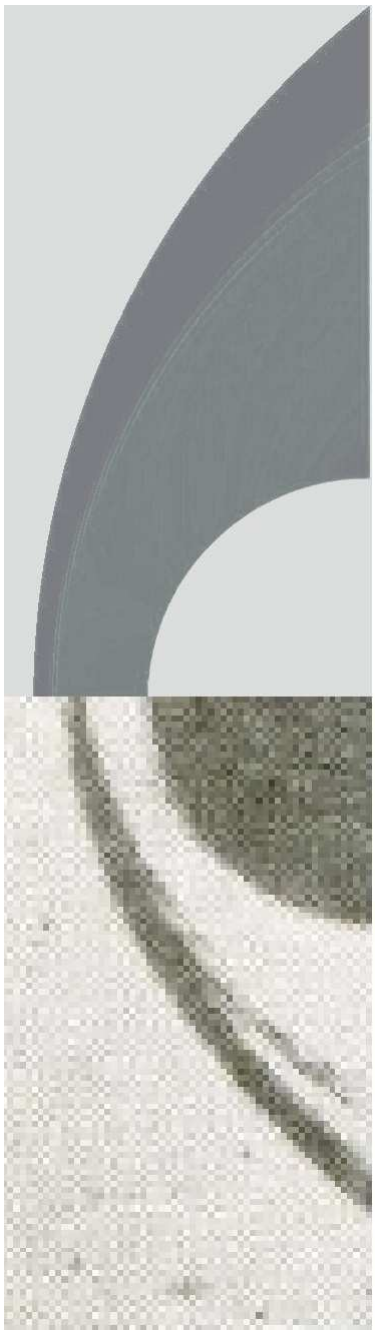

Figure 5.13: Comparison of the bow shocks between the numerical simulations with $\sigma_u = 0.7$ and $\sigma_T = 1.0$ and experiment. Top is the density field calculated by CFD, and the bottom is the experimental result.

5.8 Summary and discussion

In this chapter, four simulations for a circular cylinder in cross-flow ($Kn = 0.001$, 0.0056, 0.01 and 0.25) are reported using the Maxwell/Somoluchowski boundary conditions and the new conditions. The CFD results obtained were compared with experimental data and DSMC data. There is a good agreement for surface pressure between the DSMC data, the experimental data and the CFD results in the cases where $Kn = 0.001, 0.0056$ and 0.01. A reduction in the value of σ_u leads to an increase in the slip velocity. In this case, the curvature effect is important for predicting the slip velocity, but does not affect the surface pressure or the surface gas temperature. There are large differences in the predictions of surface quantities between the DSMC data and the CFD results for the case where $Kn = 0.25$. From the results obtained in the cases where $Kn = 0.01$ and 0.25, the simulations of the temperature jump at the wake-surface and of the slip velocity in the Knudsen layer leave scope for substantial further work and improvement.

Chapter 6

Simulations of flow past a sharp wedge and a blunt cone

6.1 Introduction

In the two previous chapters, external rarefied hypersonic flows sharp-leading-edge and blunt geometries were studied. In this chapter, flows past a sharp wedge and a blunt cone are investigated, with various slip/jump and no slip/jump conditions applied, in which the blunt cone is the practical hypersonic vehicle shape. The Maxwell/Smoluchowski conditions are tested with the values $\sigma_u = 0.7$ and $\sigma_T = 1.0$, and $\sigma_u = \sigma_T = 1.0$. The simulation results are compared with experimental data of surface pressure given in [70, 71] and the Lofthouse DSMC data ($\sigma_u = \sigma_T = 1.0$) taken from [51, 52]. The curvature effect in the slip conditions is also investigated. The Knudsen number, Kn, is calculated for the wedge and the blunt cone as follows:

$$Kn = \frac{\lambda}{H}, \tag{6.1}$$

where H is the length of the base of either the wedge or the blunt cone.

An analysis of the relative effect of thermal creep on a satellite-on-a-chip is presented by an analytical solution.

6.2 Experimental arrangement and the DSMC cases

The experimental arrangement for the wedge and the blunt cone cases is the same as for the flat plate and the circular cylinder cases presented in the previous chapters. The measurement of surface pressure requires the pressure transducers connected to pressure orifices located at the surface of the wedge and the blunt cone, as described in Chapter 4. A typical experiment set-up for the blunt cone case is shown in Figure 6.1.

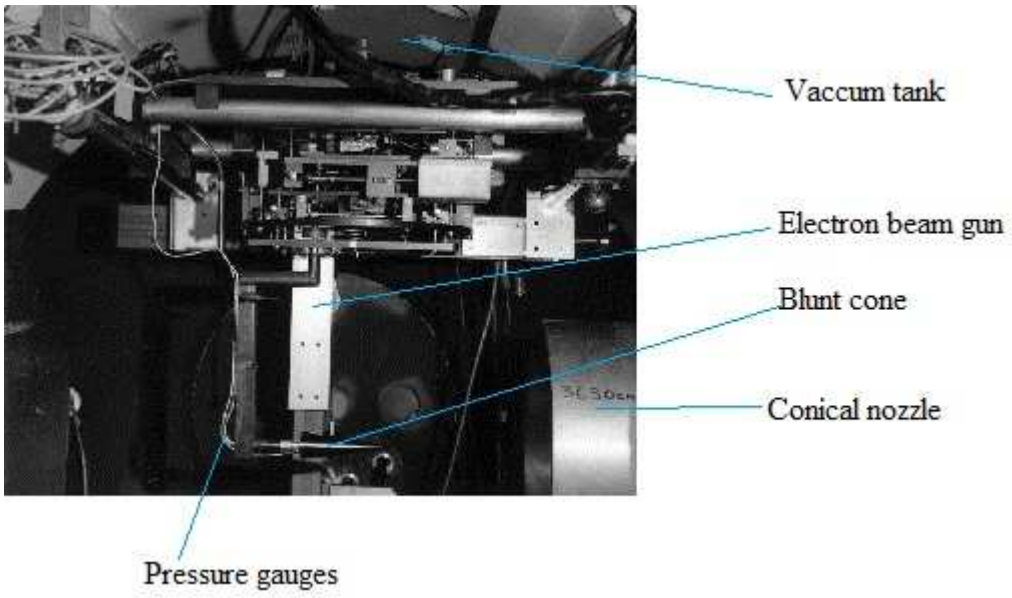

Figure 6.1: Experimental set-up for the blunt cone case [71].

The DSMC cases described in [51, 52] are explored with the same freestream flow conditions, Kn, and numerical model as in of the circular cylinder cases presented in Chapter 5. The geometries and dimensions of the wedge and the blunt cone are shown in Figure 6.2 and Table 6.1. The freestream flow conditions, the working gases, surface temperatures, and Kn for these cases are shown in Tables 6.2 and 6.3.

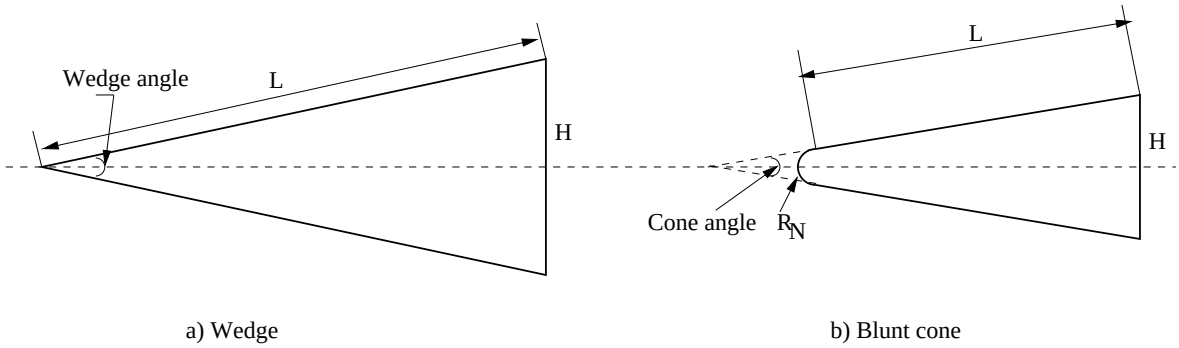

Figure 6.2: Geometries of the wedge and the blunt cone, where L is the length of the top surface, H is the height of the base, and R_N is the radius of curvature of the nose of the blunt cone.

Table 6.1: Geometrical dimensions of the wedges and the blunt cone.

	L (mm)	H (mm)	Angle (deg.)	R_N (mm)
Wedge of experimental case [70]	90.0	46.4	30	0
Wedge of the DSMC cases [51, 52]	877.64	304.8	20	0
Blunt cone [71]	137.25	42.16	16	2

Table 6.2: Freestream flow conditions of the wedge and the blunt cone cases.

	p_∞ (Pa)	T_∞ (K)	Ma
Wedge of experimental case [70]	0.76	17	24.2
Wedge of the DSMC case [51, 52]	1.17	200	10
Wedge of the DSMC case [51, 52]	0.047	200	10
Blunt cone [71]	5.39	57.5	9.81

6.3 Boundary conditions

Various nonequilibrium boundary conditions are applied on the surface of the sharp wedge and the blunt cone for the flow variables (T, $\mathbf{u}$). The boundary condition for the pressure p at the surfaces is zero normal gradient. At the inflow boundary, the freestream conditions are maintained throughout the computational process. At the top boundary and the outflow boundary, fluid is allowed to leave the computing region. This condition specifies that the normal gradients of the flow variables (p, T, $\mathbf{u}$) vanish at these boundaries. At the bottom boundary, in front of and behind the sharp wedge, a symmetry boundary condition is applied to all flow variables. For the two-dimensional axi-symmetric blunt cone

Table 6.3: The surface temperatures, the working gases and Kn in the various sharp wedge and the blunt cone cases.

	T_{wall} (K)	Gas	Kn
Wedge of experimental case [70]	294	Nitrogen	0.002
Wedge of the DSMC case [51, 52]	500	Argon	0.010
Wedge of the DSMC case [51, 52]	500	Argon	0.250
Blunt cone [71]	298	Nitrogen	0.0026

case, the geometry is specified as a wedge of one cell thickness running along the plane of symmetry. A schematic diagram of the boundary conditions applied in the two-dimesional sharp wedge and blunt cone cases is shown in Figures 6.3 and 6.4.

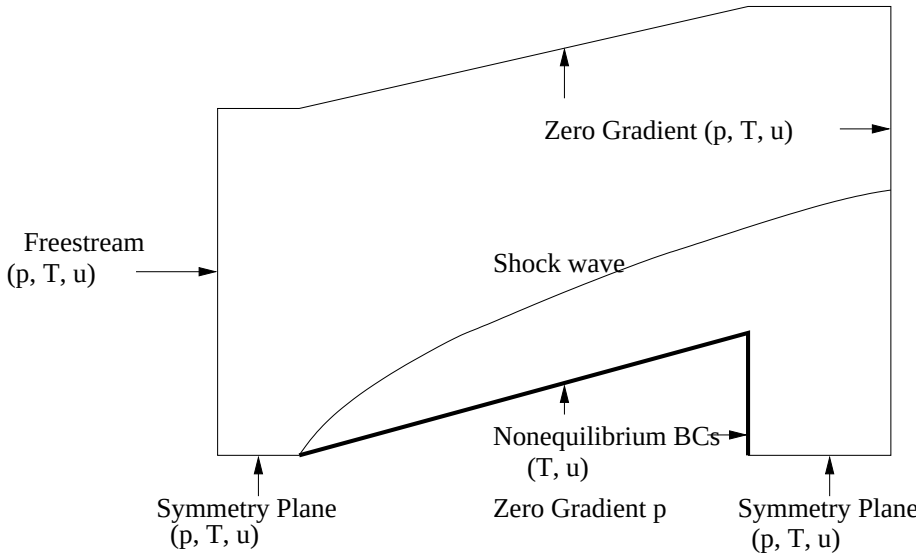

Figure 6.3: Numerical case arrangement for the sharp wedge case.

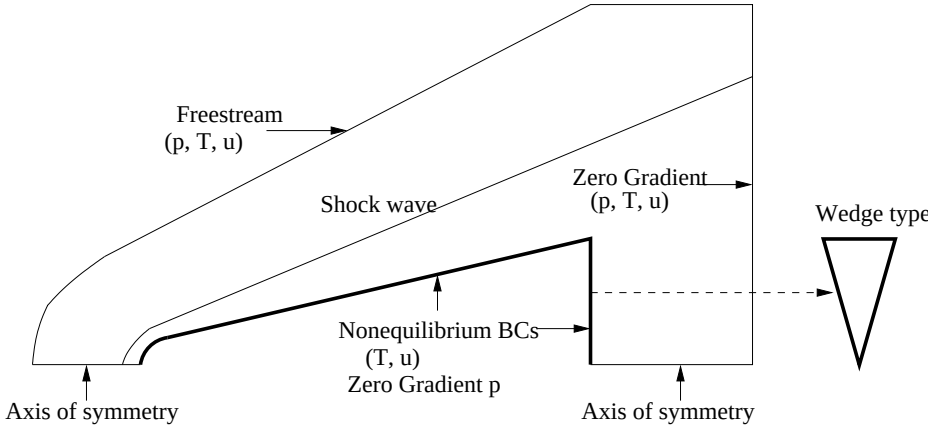

Figure 6.4: Numerical case arrangement for the blunt cone case.

6.4 Numerical mesh

The computational mesh is constructed to wrap around the shocks. For all the sharp wedge and the blunt cone cases described in [51, 52, 70, 71], mesh independence studies were conducted. The final mesh encompassing the boundary layer has a linear grading a) in the surface-parallel spacing for the wedge case, and b) in the surface-normal spacing at the nose for the blunt cone case, over the numbers of cells near the surface. As presented in Section 5.5, the values of n_c and l_c, and the smallest mesh sizes (Δx and Δy) near the surfaces of the sharp wedge and at the nose of the blunt cone, for all cases are shown in Table 6.4. Typical meshes of cells for the sharp wedge and the blunt cone simulations are shown in Figures 6.5, 6.6 and 6.7.

Table 6.4: Smallest cell size of the mesh near the surface.

Case	Kn	n_c	l_c (mm)	Δx (mm)	Δy (mm)	Total cells
Wedge [70]	0.002	75	15	1.0	$0.05 \rightarrow 0.5$	20 100
Wedge [51, 52]	0.01	120	50	2.2	$0.10 \rightarrow 1.0$	88 000
Wedge [51, 52]	0.25	100	100	5.85	$0.03 \rightarrow 5.0$	77 100
Cone [71]	0.0026	30	2.5	$0.026 \rightarrow 0.26$	0.2	5300

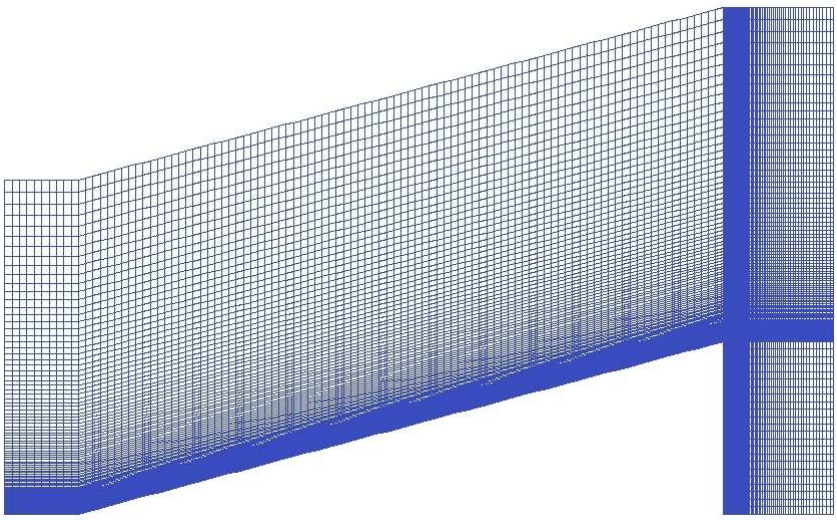

Figure 6.5: Computational mesh for the sharp wedge case, 77 100 cells.

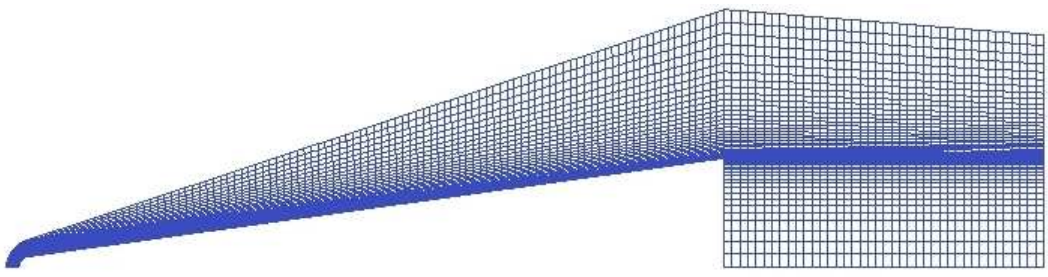

Figure 6.6: Computational mesh for the blunt cone case, 5300 cells.

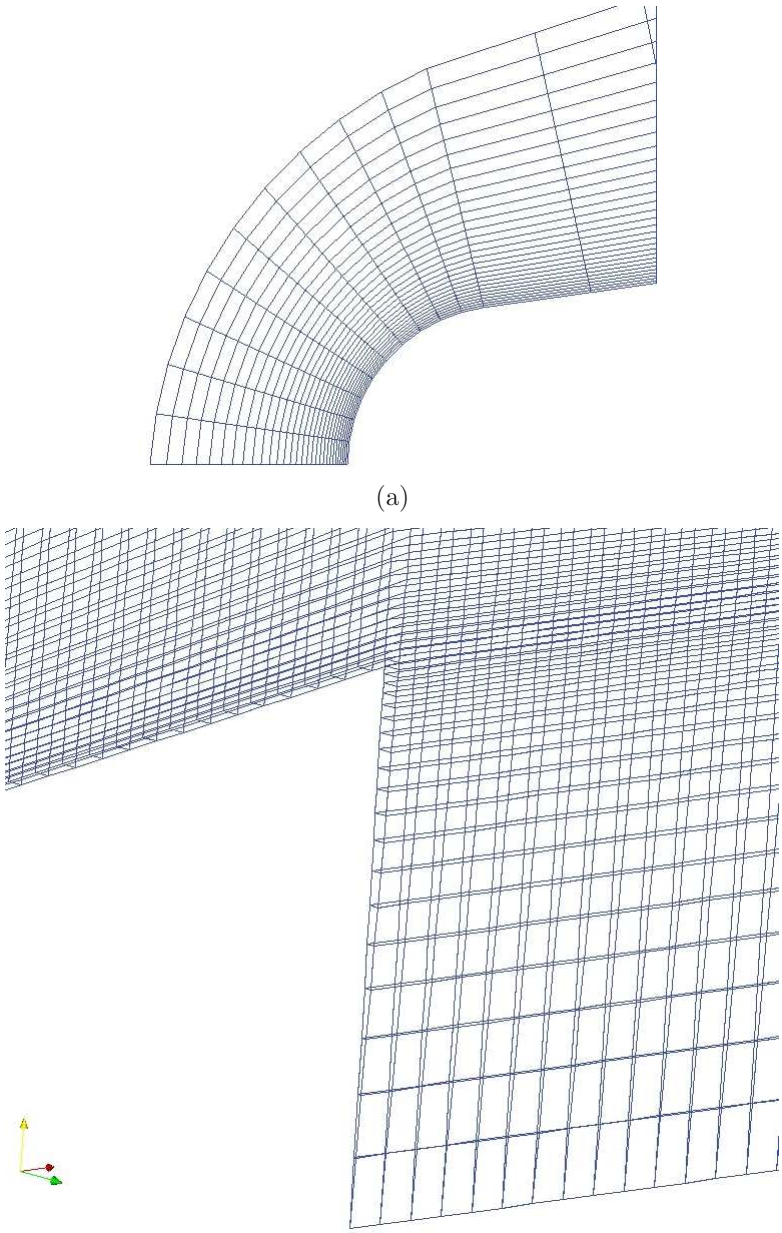

(a)

(b)

Figure 6.7: a) Mesh at the nose of the blunt cone and b) a partial side view of the mesh for simulation of the blunt cone case, showing the axi-symmetric wedge arrangement.

6.5 Transport properties

A calorically perfect gas is considered and the viscosity is calculated a) by Sutherland's law for the experimental cases [70, 71], and b) by the Power Law for the DSMC cases given in [51, 52]. The coefficient of thermal conductivity is then computed from equation (2.31).

The Prandtl number, Pr, is assumed to be constant throughout the flow. The values $A_S = 1.41\times\ 10^{-6}$ Pa.s K$^{1/2}$, $T_S = 111.0$ K from Table 2.1 are adopted for Sutherland's equation (2.30) in Chapter 2. The values $A_P = 0.31\times\ 10^{-6}$ Pa.s K^s and $s = 0.734$ are adopted for the Power Law equation (2.29) also in Chapter 2, where A_P is equivalently calculated from equations (3.33) and (3.34) with the values $\omega = 0.734$, $d_{ref} = 3.595\times\ 10^{-10}$ m, $T_{ref} = 1000$ K and $m = 6.63\times\ 10^{-26}$ kg using in the DSMC simulations in [51, 52].

The values of R, γ and Pr of various working gases used for calculation of the transport properties are given as before in Table 4.5.

6.6 Simulation results

In the sharp wedge and the blunt cone cases, a wake region is a recirculating region adjacent to the base bounded on either side by the flow which has separated from the body [64]. For the wake behind slender bodies, such as wedges and cones, the temperature changes are relatively small [68, 69].

For the sharp wedge cases, the results of the surface properties in each case are plotted as a function of the distance, S, along the wedge surface, normalized by the length, L, of the top surface. Therefore $S/L = 1$ is the location of the wedge shoulder and the beginning of the wake.

6.6.1 Experimental sharp wedge case Kn = 0.002 [70]

In this wedge case, the curvature effect in the slip conditions indicated by the term $\mathbf{\Pi}_{mc}$ in equations (3.11) and (3.37) are investigated for all tests, to assess how it affects these in simulations of hypersonic gas flow.

Considering the surface pressures, Figure 6.8 shows the new BCs give results in reasonable agreement with experimental data . The results when using the value $\sigma_u = 0.7$ in the Maxwell slip condition are close to the results of the new BCs at the leading edge. The no slip/jump conditions overpredict the surface pressure at the leading edge, as in the flat plate cases. All simulated results are close together in the wake-surface ($1 \leq S/L \leq 1.2$), as seen in Figure 6.8. The curvature effect of slip conditions does not affect the surface pressure.

Figure 6.9 shows that the surface gas temperatures are highest at the leading edge with the peak temperature of a) about 545 K for the new conditions with and without the curvature effect, b) about 540 K when $\sigma_u = \sigma_T = 1$ in the Maxwell/Smoluchowski conditions with and without the curvature effect, and c) about 460 K when $\sigma_u = 0.7, \sigma_T = 1$ in the Maxwell/Smoluchowski conditions with and without the curvature effect. Past the leading edge, the gas temperatures gradually decrease to an almost constant value along the surface. The results of the new conditions are 21% higher than results using the Maxwell/Smoluchowski conditions in the region ($0.2 \leq S/L \leq 0.95$), as seen in Figure 6.9. The curvature effect in the slip conditions does not affect the surface gas temperature.

Considering the slip velocity in Figure 6.10, all tests predict a peak normalized slip velocity at the leading edge of a) about 0.79 for the new conditions with and without the curvature effect, b) about 0.60 when using $\sigma_u = \sigma_T = 1$ with and without curvature, and c) about 0.75 and 0.77 when using $\sigma_u = 0.7$, $\sigma_T = 1$ with and without curvature effect, respectively. Past the leading edge, the slip velocity very quickly reduces to a nearly constant finite value until the wedge shoulder. The curvature effect in the slip conditions has a slight effect about 5% in the slip velocity around the wedge shoulder for the test using the value of $\sigma_u = 0.7$ in the Maxwell condition, and the other two pairs of curves overlap, as seen in Figure 6.11. On the surface of the base of the wedge, the slip velocities of all tests are close together.

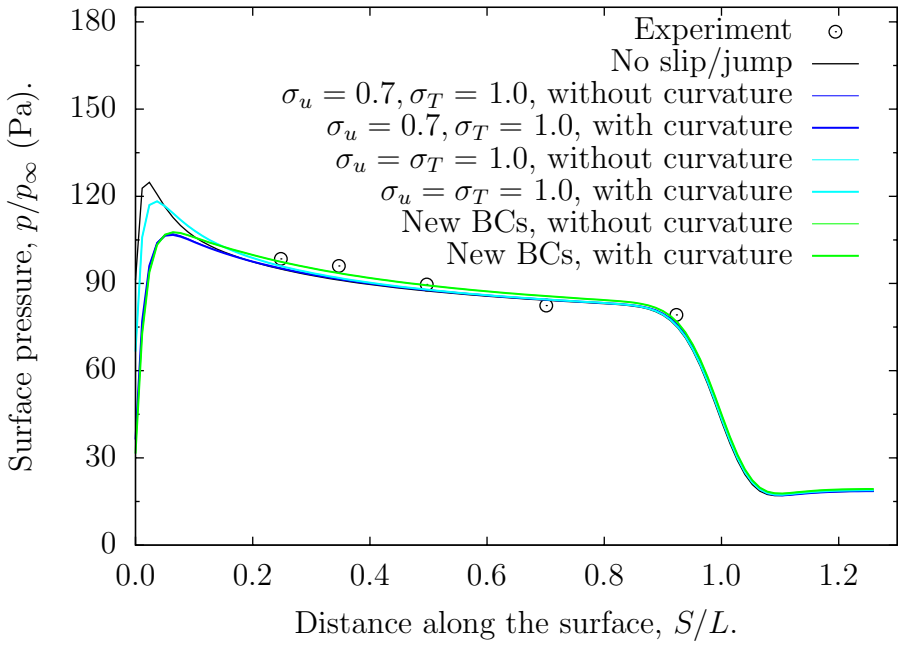

Figure 6.8: Pressure distribution along the wedge surface.

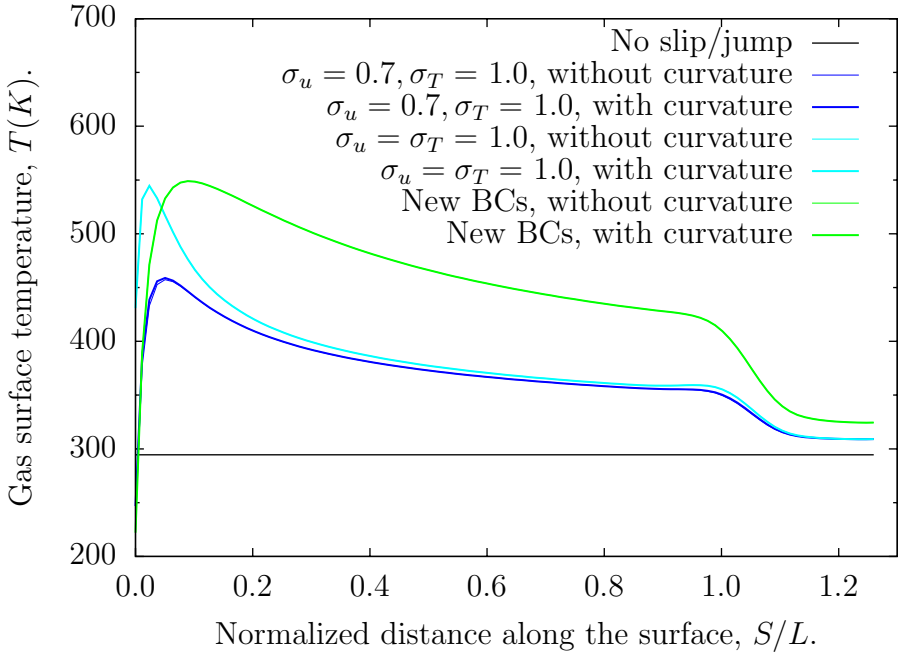

Figure 6.9: Gas surface temperature distribution along the wedge surface, $Kn = 0.002$.

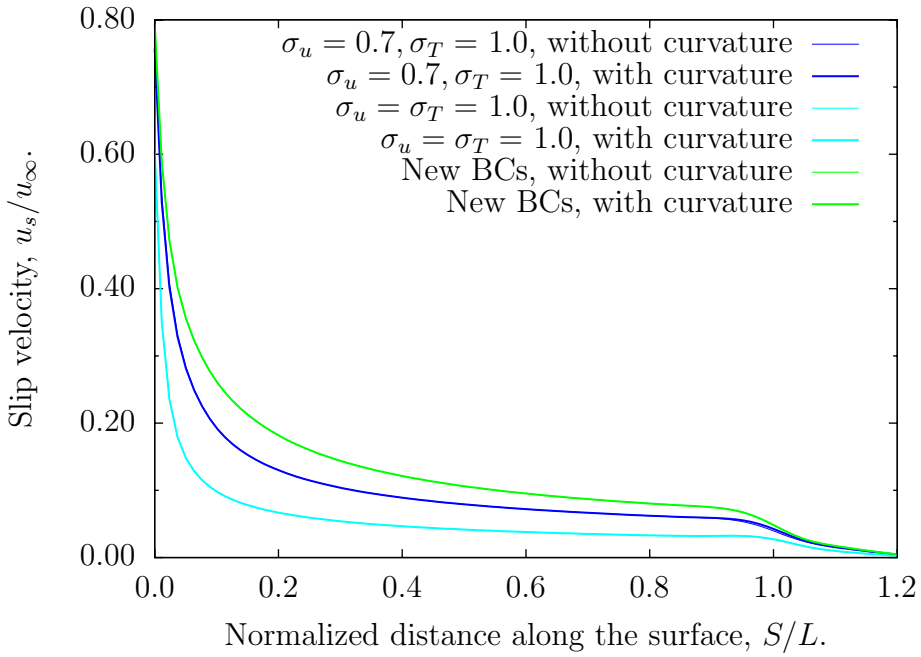

Figure 6.10: Slip velocity distribution along the wedge surface, $Kn = 0.002$.

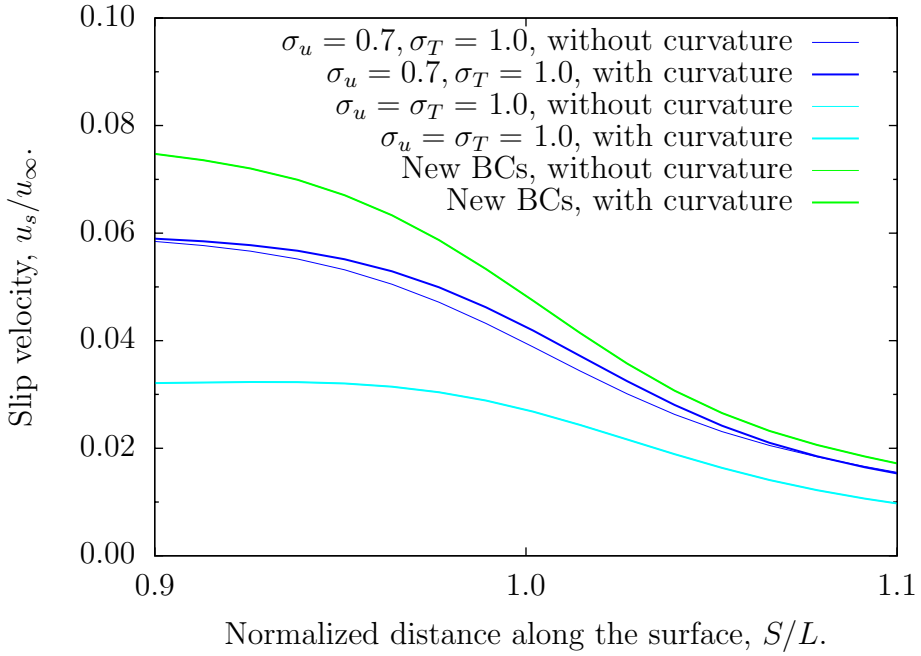

Figure 6.11: Slip velocity distribution along the surface towards the trailing edge of the wedge, $Kn = 0.002$.

6.6.2 The DSMC sharp wedge case Kn = 0.01 [51, 52]

In this case, simulations are run with the curvature effect in the slip conditions. The curvature effect seems not to strongly affect the surface quantities in the previous case. Therefore, only one more simulation without the curvature effect is carried out for the new conditions.

Considering the surface pressures in Figure 6.12, the results with the new conditions give good agreement with the DSMC data before the wedge shoulder. The no-slip/jump simulation and the test results with $\sigma_u = \sigma_T = 1$ in the Maxwell/Smoluchowski conditions overpredict the surface pressures at the leading edge. In the region, $1.0 \leq S/L \leq 1.17$ all CFD results are closed together and there is a slight difference with the DSMC data, as seen in the figure.

The temperature jumps in all the CFD results and the DSMC data are highest at the leading edge, as seen in Figure 6.13, with a peak temperature jump of a) about 750 K when using $\sigma_u = 0.7$ and $\sigma_T = 1$ in the Maxwell/Smoluchowski conditions, b) about 1150 K with the new conditions with and without curvature, c) about 1250 K when using $\sigma_u = \sigma_T = 1$ in the Maxwell/Smoluchowski conditions, and d) about 2129 K for the DSMC test. In Figure 6.13, past the leading edge, the temperature jumps gradually decrease along the surface and in addition, show a slight bump around the wedge shoulder. In the region $0.1 \leq S/L \leq 0.95$ the new conditions predict higher temperature jump than those given by the Maxwell/Smoluchowski conditions and the DSMC data. In the region $1.0 \leq S/L \leq 1.17$, all CFD results are close to the DSMC data.

Figure 6.14 shows that, at the leading edge, all the CFD results and the DSMC data show a peak normalized slip velocity of a) about 0.89 when using $\sigma_u = 0.7$ and $\sigma_T = 1$ in the Maxwell/Smoluchowski conditions , b) about 0.79 for the new conditions with and without curvature, c) about 0.68 when using $\sigma_u = \sigma_T = 1$ in the Maxwell/Smoluchowski conditions, and d) about 0.25 for the DSMC test. Past the leading edge, the slip velocities very quickly reduce to a nearly constant finite value until the wedge shoulder, after the shoulder the DSMC data are lower than all the CFD results. The slip velocities when using $\sigma_u = 0.7$ and $\sigma_T = 1$ in the Maxwell/Smoluchowski conditions and for the new conditions are close together and they are higher than both the slip velocities of the test with

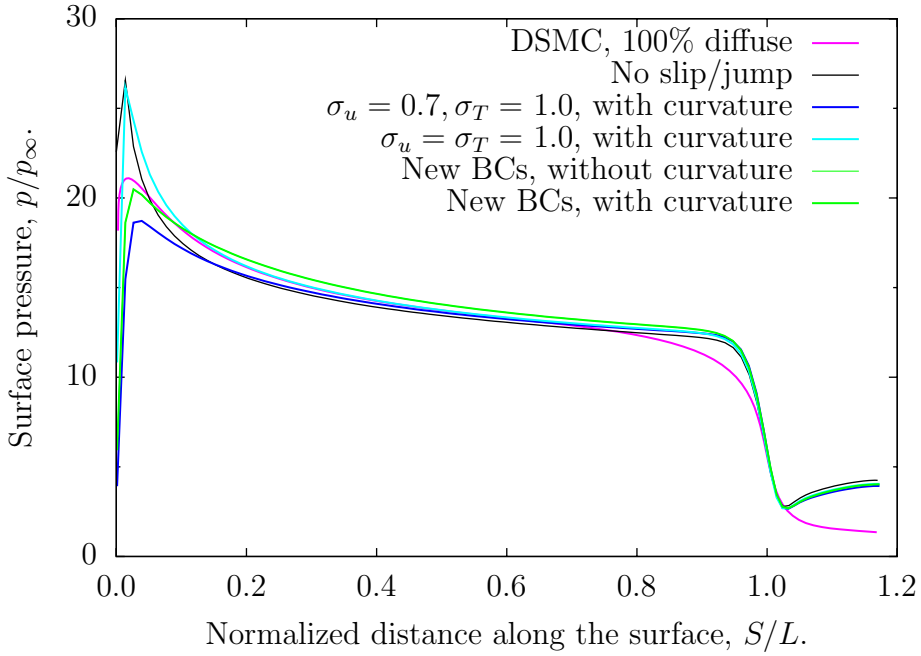

Figure 6.12: Pressure distribution along the wedge surface, $Kn = 0.01$.

$\sigma_u = \sigma_T = 1$ in the Maxwell/Smoluchowski conditions and the DSMC data until the wedge shoulder position is reached. On the surface of the base of the wedge ($1.0 \leq S/L \leq 1.17$), all the CFD results are close to the DSMC data, as seen in Figure 6.14.

The results of the tests of the new conditions show that the curvature effect does not affect the surface pressure, the temperature jump or the slip velocity, as seen in Figures 6.12, 6.13, and 6.14.

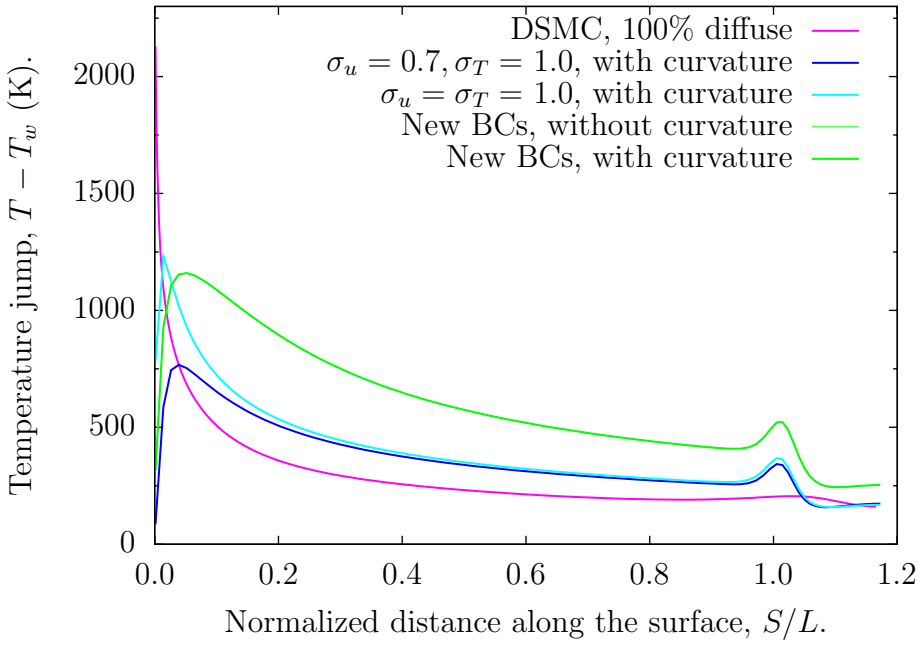

Figure 6.13: Temperature jump distribution along the wedge surface, $Kn = 0.01$.

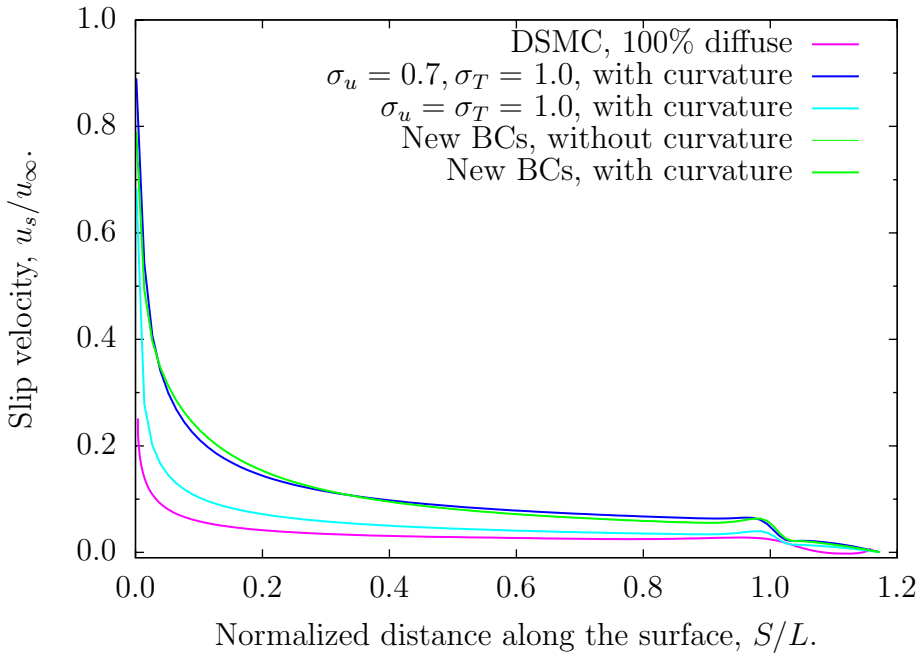

Figure 6.14: Slip velocity distribution along the wedge surface, $Kn = 0.01$.

6.6.3 The DSMC sharp wedge case, Kn = 0.25 [51, 52]

In the results obtained for the two previous wedge cases, the no slip/jump conditions overpredicted the surface pressures at the leading edge and therefore these conditions were no longer investigated. All subsequent tests on the wedge case were undertaken with the curvature effect in the slip conditions for $Kn = 0.25$.

Considering the surface pressure and the slip velocity, there are large differences between all the CFD results and the DSMC data until the location $S/L = 1.06$, as seen in Figures 6.15, 6.17. All the CFD results predict a large spike in the surface pressure at the wedge shoulder, $S/L = 1$, as the flow begins to expand into the wake region. There are also large differences in the temperature jumps between the CFD results and the DSMC data along the wedge surface, as seen in Figure 6.16.

All the CFD results obtained here show that the N–S–F equations fail in the simulation of this hypersonic gas flow at large Kn, as explained in Section 2.2.

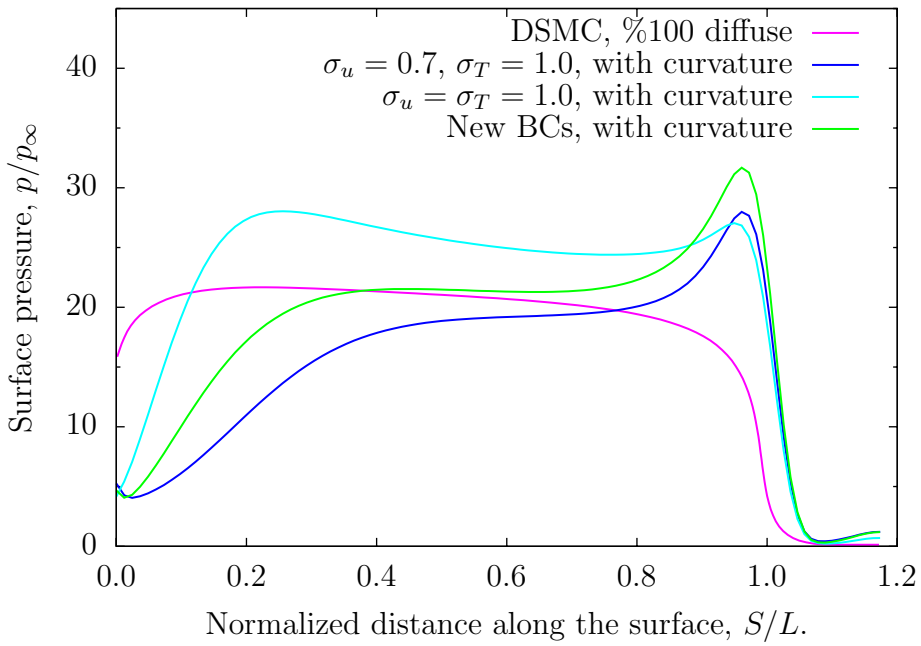

Figure 6.15: Pressure distribution along the wedge surface, $Kn = 0.25$.

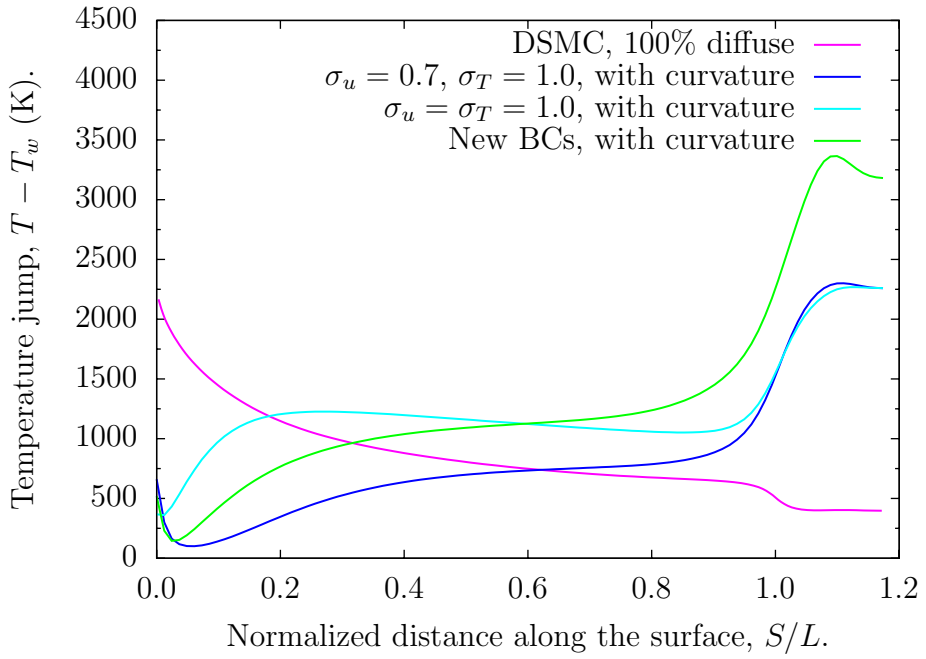

Figure 6.16: Temperature jump distribution along the wedge surface, $Kn = 0.25$.

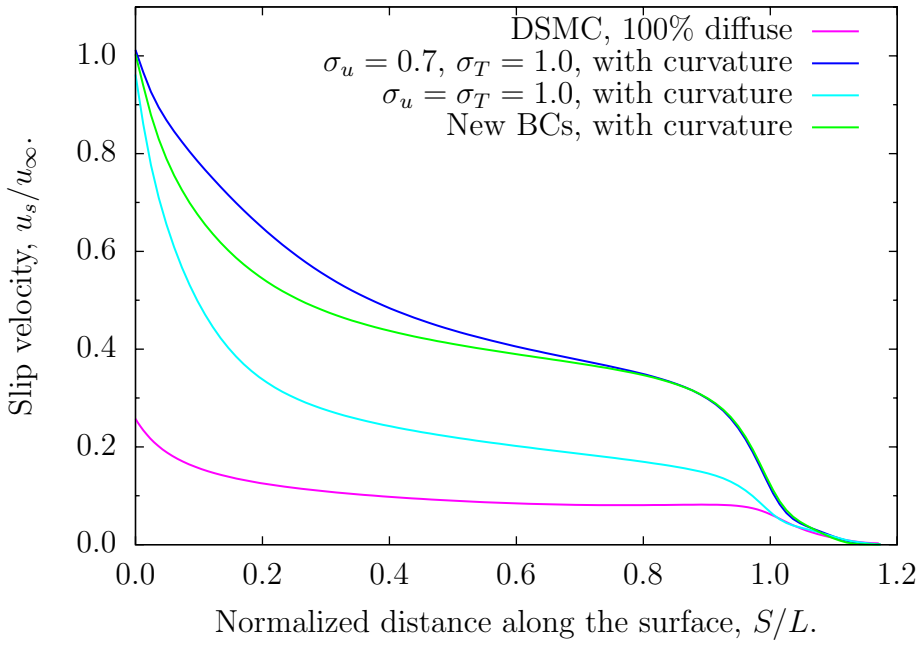

Figure 6.17: Slip velocity distribution along the wedge surface, $Kn = 0.25$.

6.6.4 Blunt cone case Kn = 0.0026 [71]

The simulation results of surface properties are plotted as a function of the distance, S, along the blunt cone surface, normalized by the nose radius, R_N. In this case, $S/R_N = 68.5$ is the location of the cone shoulder and the beginning of the wake of the flow. The three boundary condition models with and without the curvature effect, and the no-slip/jump model are tested for the blunt cone configuration.

The experiment in [71] studied the interaction of jets issuing from a vehicle in low density hypersonic flow. A conic jet interaction model was developed and tested with, and without the jet. The centre of the jet is near the cone base, $S/R_N = 65$. The pressure transducers to measure the surface pressures around the jet are installed in the region $36 \leq S/R_N \leq 63$. The experimental data of pressure distribution of the test without the jet are chosen to compare with all the CFD results.

Considering the surface pressure results in Figure 6.18, all the CFD results are close together and predict peak normalized pressures from 22.8 to 23.0 at the leading edge. Past the leading edge, the surface pressures very quickly reduce to a nearly constant finite value until the cone shoulder. All simulation results give good agreement with the experimental data in the region $36 \leq S/R_N \leq 63$. On the surface of the base of the cone ($68.5 \leq S/R_N \leq 79$), the simulation pressures are close to zero, as seen in Figure 6.18. The curvature effect does not affect the surface pressure or the surface gas temperature (see Figure 6.19). At the leading edge, the surface gas temperatures are highest, with a peak temperature of a) about 650 K for the new conditions, and b) about 460 K for the tests using the Maxwell/Smoluchowski conditions. Past the leading edge, the surface gas temperatures reduce along the surface and a slight bump is found around the cone shoulder, as seen in Figure 6.19. The new boundary conditions predict higher surface gas temperatures than the Maxwell/Smoluchowski conditions.

At the leading edge the slip velocities reach a peak normalized value and then decrease along the cone surface, see Figure 6.20. The peak slip normalized velocities are a) about 0.34 for the new boundary conditions, b) 0.29 when using $\sigma_u = 0.7$ and $\sigma_T = 1$ with the Maxwell/Smoluchowski conditions , and c) about 0.18 when

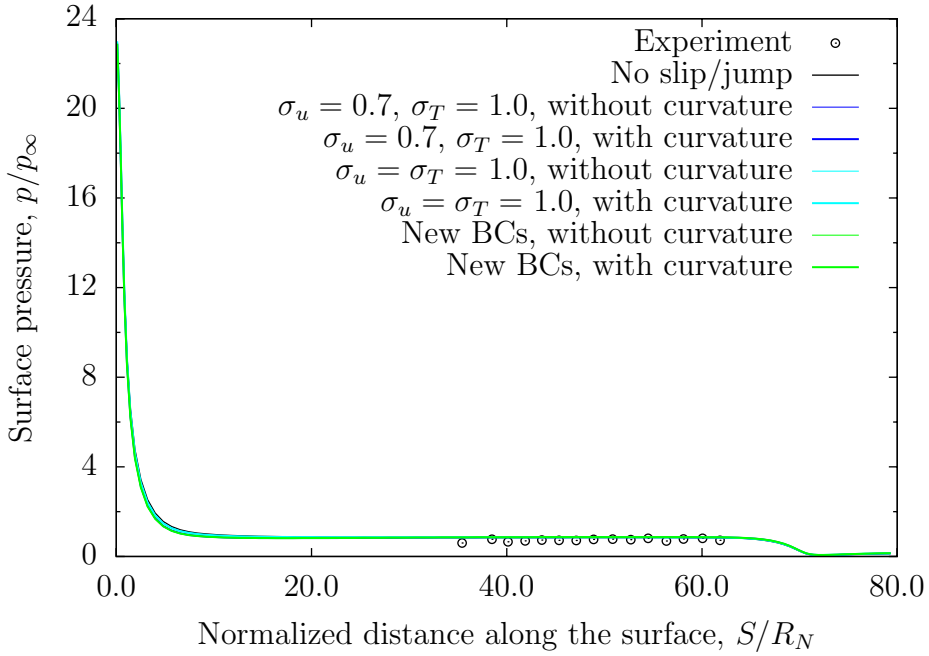

Figure 6.18: Pressure distribution along the blunt cone surface.

using $\sigma_u = \sigma_T = 1$ in the Maxwell/Smoluchowski conditions. The new boundary conditions predict a higher slip velocity than do the Maxwell/Smoluchowski conditions until the location $S/R_N = 75$. In addition, the Maxwell slip results are affected by the curvature effect around the cone shoulder, as seen in Figure 6.20.

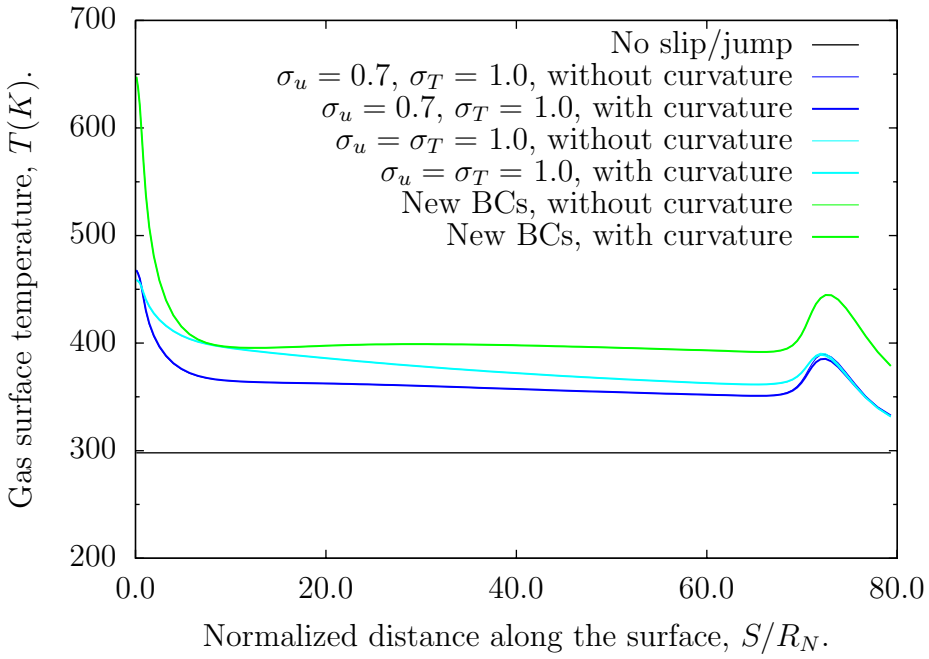

Figure 6.19: Gas surface temperature distribution along the blunt cone surface.

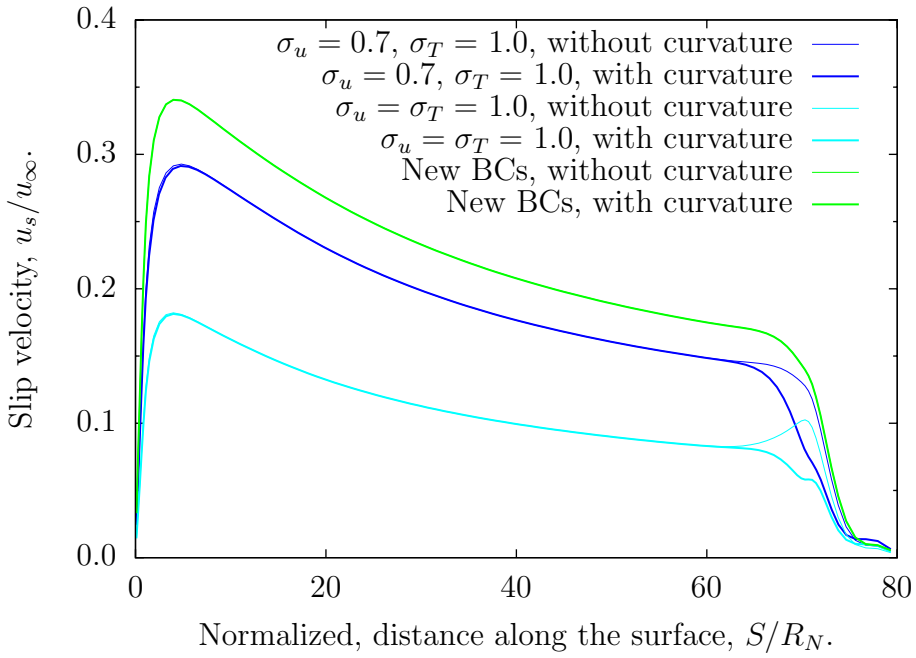

Figure 6.20: Slip velocity distribution along the blunt cone surface.

6.7 Thermal creep effect for a satellite-on-a-chip

So far, all the CFD simulations have been carried out assuming isothermal surfaces. In this section an analysis of the relative effect of thermal creep on a satellite-on-a-chip (chipsat) is presented by an analytical solution. A chipsat is a very small satellite with a mass between 1 and 100g, and is fabricated onto a single chip. The chipsat normally orbits at altitudes from 500 km to 1000 km, which is the free molecular flow regime. The energy absorbed from the Sun on one side of the chipsat is different to the energy absorbed from the Earth on the other side. This difference in temperature creates a temperature gradient across the chipsat surface. Gas molecules on the surface move from the cold region of the surface towards the hot region. This motion will induce a tangential momentum to the surface, known as thermal momentum creep, $\frac{3}{4}\frac{\mu}{\rho}\frac{\mathbf{S}\cdot\nabla T}{T}$, in equation (3.11). So, a thermal creep force, F_{creep}, on the surface from the hot side towards the cold side is calculated through [81]:

$$\boldsymbol{\tau}_{creep} = \frac{F_{creep}}{A_{cross}} = \frac{\mu}{\lambda}\frac{3}{4}\frac{\mu}{\rho}\frac{\mathbf{S}\cdot\nabla T}{T}, \tag{6.2}$$

where $\boldsymbol{\tau}_{creep}$ is the thermal creep shear stress, and A_{cross} is the cross-sectional area of the surface normal to the direction of motion.

In the present work a chipsat with dimensions (1 cm $\times$ 1 cm $\times$ 0.0025 cm) is considered, and the chipsat material is silicon. Depending on the chipsat surface normal to the direction of motion, there are two thermal creep effects for two different configurations, called cases I, and II, as seen in Figure 6.21. The working gas is air, and the Sutherland law, equation (2.30), is used for calculating the viscosity. The freestream flow conditions for the two cases at different altitudes are given in Table 6.5.

As seen in the schematic in Figure 6.21 for both cases, the left side of the chipsat surface receives direct solar energy from the Sun, E_{sun} (W), and the right side receives the energy from the Albedo, E_{Albedo} (W), and the Earth's infrared radiation, E_{IR} (W). The Earth is constantly losing heat as part of its energy cycle. About $30 \pm 5\%$ of the solar energy that arrives at the top of the atmosphere is reflected back to the space, known as the Albedo energy. The chipsat also emits radiation, E_e (W), and has the dissipated energy, $E_{dissipated}$ (W). A general energy

Table 6.5: Flow conditions of the chipsat at various altitudes [81, 84].

Altitude (km)	ρ_∞ (kg/m^3)	T_∞ (K)	u_∞ (m/s)
100	5.30×10^{-7}	195.08	7840
150	2.07×10^{-9}	634.39	7810
200	2.79×10^{-10}	854.56	7780
250	7.25×10^{-11}	941.33	7750
300	2.42×10^{-11}	976.01	7730
350	9.52×10^{-12}	990.06	7700
400	3.73×10^{-12}	995.83	7670
450	1.59×10^{-12}	998.22	7640
500	6.97×10^{-13}	999.24	7610
550	3.18×10^{-13}	999.67	7590
600	1.45×10^{-13}	999.85	7560
650	7.25×10^{-14}	999.93	7530
700	3.61×10^{-14}	999.97	7500
750	2.06×10^{-14}	999.99	7480
800	1.17×10^{-14}	999.99	7450
850	7.83×10^{-15}	1000.0	7430
900	5.25×10^{-15}	1000.0	7400
950	3.98×10^{-15}	1000.0	7380
1000	3.02×10^{-15}	1000.0	7350

balance equation for the chipsat is shown below,

$$E_{absorbed} + E_{dissipated} - E_e = 0. \tag{6.3}$$

The temperature gradients across the chipsat surface are calculated by solving this energy balance equation [83, 85], and the results of the temperature gradients of two cases at various altitudes are shown in Figure 6.22. The temperature gradients increase with increasing altitudes in both cases. The temperature gradients in case II are higher than those in case I.

Then, the thermal creep forces are calculated by equation (6.2) in the two cases, and may be compared with the drag forces, F_D, computed as,

$$F_D = 0.5\rho u^2 A_{ref} C_D, \tag{6.4}$$

where C_D is the drag coefficient, with $C_D = 2.1$ for the chipsat geometry [84], and A_{ref} is the reference area (i.e. a plane perpendicular to the direction of motion).

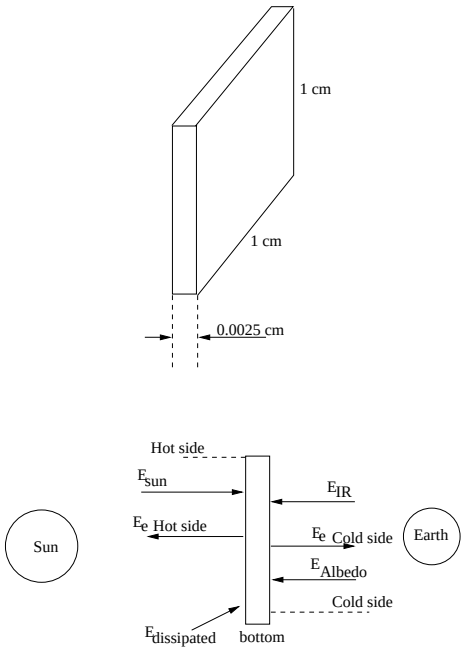

Figure 6.21: Geometry and energy balances for the chipsat for its orbit in two different configurations.

The thermal creep forces and the drag forces in the two cases at different altitudes are presented in Figure 6.23. The drag forces in the two cases decrease quickly with increasing altitudes, while the creep forces increase slightly with increasing altitudes. At altitudes from 100 km to 550 km the creep forces are less than the drag forces for both cases. However, the creep forces are greater than the drag forces at altitudes from 550 km to 1000 km, where the chipsat normally travels. These results show the importance of the thermal creep effect for a complete understanding of the dynamics and accurate prediction of the orbit of certain satellites.

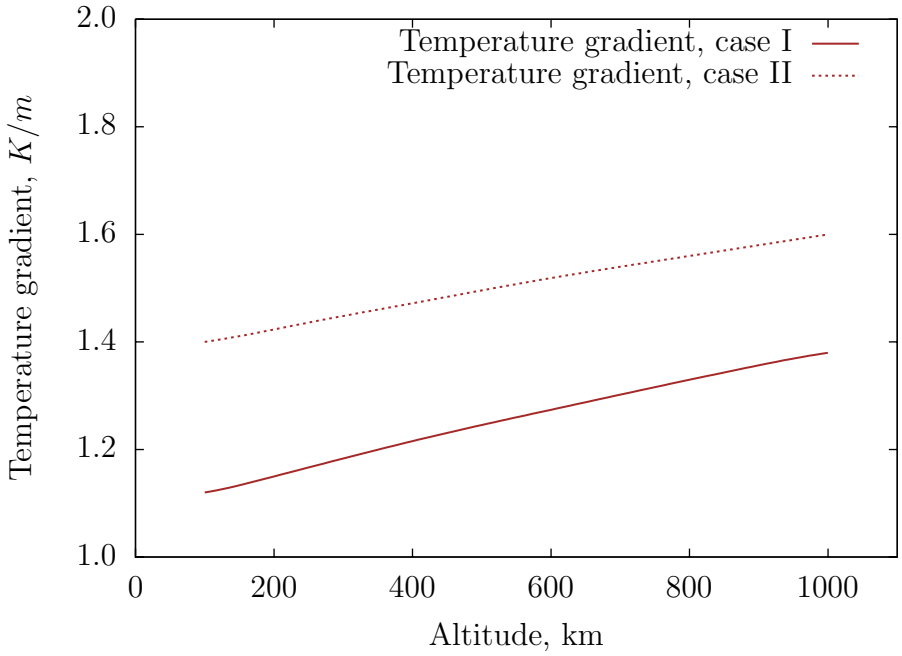

Figure 6.22: Calculated temperature gradient across the chipsat surface in the two cases at various orbit altitudes.

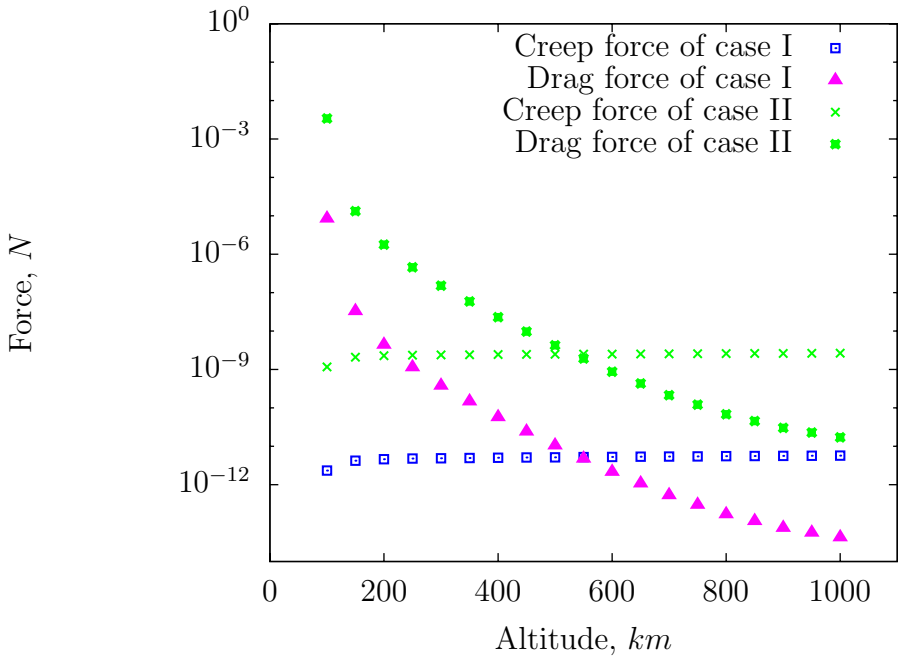

Figure 6.23: Calculated thermal creep and drag forces in the two cases at various orbit altitudes.

6.8 Summary and discussion

From the results obtained in this chapter, it is clear that the no slip/jump model is unacceptable for simulating hypersonic gas flows. The new boundary conditions give reasonably good agreement for the surface pressure when comparing with DSMC and experimental data for both the wedge cases ($Kn = 0.002$ and 0.01) and the blunt cone case. Using $\sigma_u = 0.7$ and $\sigma_T = 1$ with the Maxwell/Smoluchowski conditions also gives good predictions for surface pressure. Furthermore, the curvature effect does not appear to affect the surface pressure or gas surface temperature; it just affects the slip velocity around the wedge shoulder and the cone shoulder.

A smaller value of σ_u in the Maxwell slip condition leads to a decrease in the surface gas temperature and an increase in the slip velocity along the surface. Reducing σ_u also decreases the surface pressure at the sharp leading edge, to reasonable agreement with the DSMC data and experimental data in Figures 6.8, 6.12, 6.15.

It is seen that the DSMC profile of the temperature jump is very similar to that for the slip velocity, because the temperature jump is calculated as a function of velocity, as presented in Chapter 3. For the sharp wedge cases near the leading edge, the DSMC method predicts much higher gas temperature than the CFD method. There is a large difference between the CFD results and the DSMC data at large Kn number. This shows that the N–S–F equations themselves fail at large Kn because the assumptions of a continuum-fluid flow are not preserved. It has also been shown that the thermal creep can be an important consideration in the design of future micro spacecraft.

Chapter 7

Conclusions and future work

7.1 Conclusions

In this thesis, various slip/jump boundary conditions have been presented and investigated for their usefulness in the simulation of hypersonic flows of air, argon and nitrogen over both sharp and blunt bodies. The Knudsen numbers have varied from 0.001 to 0.25, and characterize the extent of translational nonequilibrium of the rarefied gas flows.

For sharp geometries, such as the sharp-leading-edge flat plate and the sharp wedge, the new boundary conditions derived in the thesis give reasonable predictions, compared to both experimental and DSMC data for surface pressure [46, 53–56,60] and gas surface temperature [53]. However, the Maxwell/Smoluchowski conditions give good predictions of the surface pressures if the values $\sigma_u = 0.7$ and $\sigma_T = 1.0$ are used. Together with the Smoluchowski jump condition with the value $\sigma_T = 1.0$, the second order slip condition with the coefficients $A_1 = 1.5$ and $A_2 = 1.0$ predicts well the surface pressures, compared with experimental and DMSC data, in the flat plate cases.

However, the simulation results in this thesis show that using the second-order slip condition is not much better than using the conventional Maxwell slip condition with the N–S–F equations.

The reduction of the value σ_u in the Maxwell slip condition decreased the gas surface temperature and increased the slip velocity along the surfaces. Overall,

the new boundary conditions developed here predicted a higher slip velocity and a higher gas temperature than do the Maxwell/Smoluchowski conditions and the second-order slip/Smoluchowski conditions. For the sharp wedge case, the curvature effect in the slip boundary conditions does not affect the surface pressure or the gas surface temperature predictions. However, it does affect the slip velocity at the wedge shoulder. In the wedge case with $Kn = 0.25$, the simulation results have shown that the N–S–F equations fail at large Knudsen number, as the hypothesis of the continuum-fluid is broken. For sharp leading edge geometries, the DSMC model predicted a much higher temperature than the CFD method.

Considering blunt geometries, such as the cylinder and the blunt cone, the Maxwell/ Smoluchowski conditions with values of $\sigma_u = 0.7$ and $\sigma_T = 1.0$, and $\sigma_u = \sigma_T = 1.0$ and the new boundary conditions all gave good predictions for the surface pressures of the circular cylinder when $Kn = 0.001, 0.0056$ and 0.01, and for the blunt cone case, compared with the DSMC and experimental data. The new boundary conditions predicted higher temperatures than the Maxwell/Smoluchoski conditions did. The curvature effect only affected the slip velocity in the circular cylinder cases and the blunt cone case at the cone shoulder. In the cylinder cases, the DSMC temperature jump profiles were similar to those for the DSMC slip velocity. On the wake-surface, there is a difference for predictions of the temperature jump of the cylinder case between the CFD results and the DSMC data. A reduction of in σ_u, in the Maxwell slip condition also decreased the gas temperature and increased the slip velocity along the surfaces. There were also differences in predictions of the surface quantities between the CFD results and the DSMC data in the circular cylinder case when $Kn = 0.25$.

This comprehensive investigation points to the first important conclusion. Regardless of the chosen simulation geometries, the no slip/jump boundary conditions are unacceptable for simulating hypersonic gas flows. The no slip/jump conditions overpredict the surface pressures at a sharp-leading-edge and the stagnation points of blunt bodies. There is also a difference in the velocity profile through the Knudsen layer between the DSMC data and the CFD results. The boundary condition tests show that the Langmuir conditions cannot be used in simulating hypersonic gas flows, as they are not fully compatible with the fluid dynamic situation.

From the simulation results obtained, we can conclude the new boundary conditions based on a combination of the Langmuir adsorption isotherm and Maxwell/ Smoluchowski conditions give reasonably good predictions for surface pressures, which would then lead to reasonably accurate predictions of drag. The new conditions, however, predict higher surface gas temperatures than either the Maxwell/S-moluchoski conditions or the second-order slip/Smoluchowski conditions.

In the design of space vehicles, a precise prediction of gas surface temperature, though desirable, may not be essential, in that the thermal protection will be designed to withstand higher temperatures than are absolutely necessary. However, accurate prediction of drag, as obtained through surface pressure distribution, is important for a complete understanding of flight vehicle dynamics and accurate prediction of the vehicle's trajectory. The thermal creep effect is also important for the dynamics and the accurate prediction of the orbit of certain satellites.

7.2 Contributions

The outcomes of the present work provide contributions concerning the usefulness of certain surface boundary conditions in simulating hypersonic gas flows:

1. New, more realistic boundary conditions are proposed by combining the Langmuir adsorption isotherm with the Maxwell/Smoluchowski conditions. These address the problem of the values of free parameters such as the tangential momentum, σ_u, and the thermal, σ_T, accommodation coefficients in the first order slip/jump conditions. These new boundary conditions give better predictions of the surface pressure in sharp-leading-edge geometries.

2. The results obtained in this thesis indicate different options for the slip/jump conditions in simulating hypersonic gas flows. The choice can be one of the following options:

a) using the new boundary conditions proposed in this thesis.

b) using the Maxwell/Smoluchowski conditions with the values $\sigma_u = 0.7$ and $\sigma_T = 1.0$.

c) using the second slip/Smoluchowski conditions with the values $A_1 = 1.5$, $A_2 = 1.0$ and $\sigma_T = 1.0$. This should only be used in a planar surface simulation.

7.3 Future work

In this section, future work is suggested to improve the capability of the N–S–F model to simulate hypersonic gas flows.

It is seen that none of the nonequilibrium boundary conditions tested in this thesis give very good full-field predictions. Even using the new boundary conditions developed in this thesis, there is still a difference of the velocity profile through the Knudsen layer between the DSMC method and the CFD method. To overcome this problem, a modification of the viscosity in the Knudsen layer with a surface function was proposed in reference [59]. This new surface function was evaluated for isothermal micro-flows. Using this surface function for non-isothermal flow and hypersonic rarefied gas flows should be considered, to provide a possible improvement.

The two-temperature model (translational/rotational and vibrational temperatures) described in [72] should be implemented into the N–S–F solver, so that it can predict the rotational and vibrational temperatures for diatomic and polyatomic gases at higher temperatures (i.e. greater than 4000 K [1]).

This research has been restricted to a perfect gas model only. Thus, the real gas models need to be studied and implemented into the solver so that it can model real hypersonic gas flows. The present work just considers thermal nonequilibrium. At the higher temperatures that often occur in hypersonic gas flows, chemical reactions become important (dissociation and recombination). Further research into chemical reactions are necessary to model them as accurately as possible. The effects of chemical nonequilibrium and catalysis on the surface of the hypersonic vehicle should then be studied. It is necessary to consider any relations between vibrational energy activation and dissociation rates.

References

[1] J. D. Anderson, Hypersonic and High Temperature Gas Dynamics, *AIAA Press*, 2007.

[2] J. S. Greathouse, B. S. Kirk, R. P. Lillard, T. H. Truong, P. Robinson and C. J. Cerimele, Crew exploration vehicle (CEV) crew module shape selcetion analysis and CEV aeroscience project overview. *AIAA paper*, 2007-0603, 2007.

[3] J. J. Bertin and R. M. Cummings, Critical hypersonic aerothermodynamic phenomena, *Annual Review of Fluid Mechanics*, Vol. 38, pp. 129–157, 2006.

[4] P. Papadopoulos, E. Venkatapathy, D. Prabhu, M. P. Loomis and D. Olynick, Current grid-generation strategies and future requirements in hypersonic vehicle design, analysis and testing, *Applied Mathematical Modelling*, Vol. 23, pp. 705–735, 1999.

[5] J. C. Maxwell, On stresses in rarefied gases arising from inequalities of temperature, *Philosophical Transactions of the Royal Society*, Part 1, Vol. 170, pp. 231–256, 1879.

[6] M. von Smoluchowski, Über wärmeleitung in verdünnten gasen, *Annalen der Physik und Chemie*, Vol. 64, pp. 101–130, 1898.

[7] T. Gökçen and R. W. MacCormack, Nonequilibrium effects for hypersonic transitional flows using continuum approach, *AIAA paper*, No. 1989–0461, 1989.

[8] D. A. Lockerby, J. M. Reese, D. R. Emerson and R. W. Barber, Velocity boundary condition at solid walls in rarefied gas calculations, *Physical Review E*, Vol. 70, 017303, 2004.

[9] R. S. Myong, Gaseous slip models based on the Langmuir adsorption isotherm, *Physics of Fluids*, Vol.16, pp. 104–117, 2004.

[10] R. S. Myong, J. M. Reese, R. W. Barber, and D. R. Emerson, Velocity slip in microscale cylindrical Couette flow: the Langmuir model, *Physics of Fluids*, Vol. 17, 087105, 2005.

[11] A. Q. Zade, M. Renksizbulut and J. Friedman, Boundary conditions for multi-component slip-flows based on the kinetic theory of gases, *Proceedings of the 6th International ASME Conference on Nanochannels, Microchannels and Minichannels*, pp. 1–21, 2008.

[12] S. Shen, G. Chen, R. M. Crone and M. Anaya-Dufresne, A kinetic theory based first order slip boundary condition for gas flow, *Physics of Fluids*, Vol. 19, 086101, 2007.

[13] D. A. Lockerby, J. M. Reese and M. A. Gallis, A wall-function approach to incorporating Knudsen-layer effects in gas micro flow simulations, *Proceedings of the 24th International Symposium on Rarefied Gas Dynamics*, pp. 731–736, 2004.

[14] W. G. Vincenti and C. H. Kruger Jr., Introduction to Physical Gas Dynamics, *Krieger, Florida*, 1965.

[15] R. G. Deissler, An analysis of second order slip flow and temperature jump boundary conditions for rarefied gases, *International Journal of Heat and Mass Transfer*, Vol. 7, pp. 681–694, 1964.

[16] N. G Hadjiconstantinou, Comment on Cercignani's second order slip coefficient, *Physics of Fluids*, Vol. 15, pp. 2352–2354, 2003.

[17] C. Cercignani, Mathematical Methods in Kinetic Theory, *Plenum, New York*, 1969.

[18] R. Schamberg, The fundamental differential equations and the boundary conditions for high speed slip-flow, and their application to several specific problems, Ph.D thesis, *California Institute of technology*, 1947.

[19] H. Struchtrup, Macroscopic Transport Equations for Rarefied Gas Flows, *Springer*, 2005.

[20] J. C. Tannehill and G. R. Eisler, Numerical computation of the hypersonic leading edge problem using the Burnett equations, *Physics of Fluids*, Vol.19, pp. 9–15, 1976.

[21] R. Gatignol, Kinetic theory boundary conditions for discrete velocity gases, *Physics of Fluids*, Vol.20, pp. 2022–2030, 1977.

[22] G. N. Patterson, Molecular Flow of Gases, *Wiley, New York* , 1956.

[23] E. H. Kennard, Kinetic Theory of Gases, *McGraw-Hill Book Company Inc*, 1938.

[24] S. Chapman, and T. G. Cowling, The Mathematical Theory of Non-Uniform Gases, 3rd edition, *Cambridge University Press*, 1970.

[25] T. I. Gombosi, Gaskinetic Theory, *Cambridge University Press*, 1994.

[26] G. A. Bird, Molecular Gas Dynamics and the Direct Simulation of Gas Flows, *Oxford: Clarendon*, 1994.

[27] P. L. Bhatnagar, E. P. Gross and M. Krook, A model for collision processes in gases I. small amplitude processes in charged and neutral one-component systems, *Physical Review*, Vol 94, No. 3, pp. 511–525, 1954.

[28] D. Burnett, The distribution of molecular veocities and the mean motion in a non-uniform gas, *Proceedings of the London Mathematical Society*, Vol. 40, pp. 382 – 435, 1935.

[29] P. S. Prasanth and J. K. Kakkassery, Direct simulation Monte-Carlo (DSMC): A numerical method for transition-regime flows – A review, *Journal of Indian Institute of Science*, Vol. 86, pp. 169 – 192, 2006.

[30] C. J. Greenshields, H. G. Weller, L. Gasparini, and J. M. Reese, Non-oscillatory central schemes for high speed viscous flows, *International Journal for Numerical Methods in Fluids*, Vol. 23, pp. 1–21, 2010.

[31] A. Kurganov and E. Tadmor, New high-resolution central schemes for non-linear conservation laws and convection-diffusion equations, *Journal of Computational Physics*, Vol. 160, pp. 241–282, 2001.

[32] A. Kurganov, S. Noelle and G. Petrova, Semi-discrete central-upwind schemes for hyperbolic conservation laws and Hamilton-Jacobi equations, *SIAM Journal on Scientific Computing*, Vol. 23, pp. 707–740, 2001.

[33] P. L. Roe, Characteristic-based schemes for the Euler equations, *Annual Review of Fluid Mechanics*, Vol. 18, pp. 337 – 365, 1986.

[34] B. van Leer, Towards the ultimate conservative difference scheme, II: monotonicity and conservation combined in a second order scheme, *Journal of Computational Physics*, Vol. 17, pp. 361 – 370, 1974.

[35] www.opencfd.co.uk/openfoam/, 2009.

[36] W. Wang and I. D. Boyd, Hybrid DSMC-CFD simulations of hypersonic flow over sharp and blunted bodies, *The 36th AIAA Thermophysics Conference*, AIAA 2003–3644, 2003.

[37] C. J. Greenshields, and J. M. Reese, The structure of shock waves as a test of Brenner's modifications to the Navier-Stokes equations, *Journal of Fluid of Mechanics*, Vol. 580, pp. 407 – 429, 2007.

[38] C. R. Lilley, and M.N. Macrossan, DSMC calculations of shock structure with various viscosity laws, *Proceedings of the 23rd International Symposium on Rarefied Gas Dynamics*, Whistler, Canada, pp. 663, 2002.

[39] http://www.Imnoeng.com/Flow/GasViscosity.htm, 2008.

[40] R. C. Weast, Chemical Rubber Company (CRC), CRC Handbook of Chemistry and Physics, *CRC Press Inc*, Florida, USA, 1984.

[41] Crane Company, Flow of fluid through valves, fittings and pipes, Technical Paper No. 410, 1988.

[42] D. K. Bhattacharya, and B. C. Eu, Nonlinear transport processes and fluid dynamics: effects of thermoviscous coupling and nonlinear transport coefficients on plane Couette flow of Lennard-Jones fluids, *Physical Review A*, Vol. 35, No. 2, pp. 821 – 836, 1987.

[43] H. Choi, D. H. Lee, and D. Lee, Complex microscale flow simulations using langmuir slip condition, *Numerical Heat Transfer*, Part A, Vol. 48, pp. 407 – 425, 2005.

[44] R. S. Myong, D. A. Lockerby, and J. M. Reese, The effect of slip on microscale heat transfer: an extended Graetz problem, *International Journal of Heat and Mass Transfer*, Vol. 49, pp. 2502 – 2513, 2006.

[45] S. Dushman, Scientific Foundations of Vacuum Techniques, *Wiley, New York*, 1962.

[46] M. Becker, Flat plate flow field and surface measurements from merged layer into transition regime, *Proceedings of the 7th International Symposium on Rarefied Gas Dynamics*, pp. 515 – 528, 1969.

[47] R. I. Masel, Principles of Adsorption and Reaction on Solid Surfaces, *John Wiley & Sons, New York*, 1996.

[48] J. Tóth, Adsorption: Theory, Modeling and Analysis, *Surfactant Science Series*, Vol. 107, 2001.

[49] C. J. Greenshields, private communication, 2008.

[50] A. Lofthouse, L. C. Scalabrin, and I. D. Boyd, Velocity slip and temperature jump in hypersonic aerothermodynamics, *AIAA paper*, No.2007 – 208, 2007.

[51] A. Lofthouse, L. C. Scalabrin, and I. D. Boyd, Velocity slip and temperature jump in hypersonic aerothermodynamics, *Journal of Thermophysics and Heat Transfer*, Vol.22, No. 1, pp. 38 – 49, 2008.

[52] A. J. Lofthouse, Nonequilibrium hypersonic aerothermodynamics using the direct simulation Monte Carlo and Navier-Stokes models, *Ph.D Thesis, University of Michigan*, 2008.

[53] S. C. Metcalf, D. C. Lillicrap, and C. J. Berry, A study of the effect of surface temperature on the shock-layer development over sharp-edge shapes in low-Reynolds-number high-speed flow, *Proceedings of the 7th International Symposium on Rarefied Gas Dynamics*, pp 619 – 634, 1969.

[54] R. J. Vidal, T. C. Golian, and J. A. Bartz, An experimental study of hypersonic low density viscous effects on a sharp flat plate, *AIAA paper*, No.63 – 435, 1963.

[55] M. Becker, and D. E. Boylan, Experimental flow fied investigations near the sharp leading edge of a cooled flat plate in a hypervelocity, low density flow,

Proceedings of the 5th International Symposium on Rarefied Gas Dynamics, pp. 993 – 1014, 1967.

[56] J. C. Lengrand, J. Allegre, A. Chpoun, and M. Raffin, Rarefied hypersonic flow over a sharp flat plate: numerical and experimental results, *Proceedings of the 18th International Symposium on Rarefied Gas Dynamics*, pp. 276 – 284, 1992.

[57] N. Tsuboi, and Y. Matsumoto, Experimental and numerical study of hypersonic rarefied gas flow flat plates, *AIAA Journal*, Vol.43 No.6, pp. 1243 – 1255, 2005.

[58] B. Cordero, V. Gmez, A. E. Platero-Prats, M. Revs, J. Echeverra, E. Cremades, F. Barragn and S. Alvarez, Covalent radii revisited. *Dalton Transactions*, pp. 2832–2838, 2008.

[59] D. A. Lockerby, J. M. Reese, and M. A. Gallis, Capturing the Knudsen layer in continuum fluid models of nonequilibrium gas flows, *AIAA Journal*, Vol. 43, No. 6, pp. 1391 – 1393, 2005.

[60] C. White, private communication, 2009.

[61] G. A. Bird, Definition of mean free path for real gases, *Physics of Fluids*, Vol. 26, No.11, pp 3222 – 3223, 1958.

[62] A. R. Wieting and M. S. Holden, Experimental shock-wave interference heating on a cylinder at Mach 6 and 8, *AIAA Journal*, Vol. 27, pp. 1557 – 1565, 1989.

[63] G. M Gregorek, and K. D. Korkan, An experimental observation of the Mach and Reynolds-number independence of cylinder in hypersonic flow, *AIAA Journal*, Vol. 1, pp. 210 - 211, 1962.

[64] S. A. Berger, Laminar Wakes, *Elsevier, New York*, 1971.

[65] G. Park, S. L. Gai and A. J. Neely, Laminar near wake of a circular cylinder at hypersonic speeds, *AIAA Journal*, Vol. 48, pp. 236 – 248, 2010.

[66] L. Lees, Laminar heat transfer over blunt-nosed bodies at hypersonic flight speeds, *Jet propulsion*, Vol. 26, No. 4, pp. 259 – 269, 1956.

[67] J. A. Fay and F. R. Riddell, Theory of stagnation point heat transfer in dissociated air, *Journal of the Aerospace Sciences*, Vol.25, No. 2, pp. 73 – 85, 1958.

[68] E. P. Muntz and E. J. Softley, A study of laminar near wakes, *AIAA Journal*, Vol. 4, pp. 961 – 968, 1966.

[69] E. M. Murman, Experimental studies of a laminar hypersonic cone wake, *AIAA Journal*, Vol. 7, pp. 1724 – 1730, 1969.

[70] W. J. McCroskey, S. M. Bogdnoff and A. P. Genchi, Leading edge flow studies of sharp bodies in rarefied hypersonic flows, *Proceedings of the 5th International Symposium on Rarefied Gas Dynamics*, pp. 1047–1066, 1967.

[71] K. Warburton, Control jets in low density flow, *Ph.D Thesis, University of Oxford*, 1999.

[72] C. Park, Nonequilibrium Hypersonic Aerothermodynamics, *John Wiley & Sons*, 1990.

[73] J. N. Moss, R. A. Mitcheltree, V. K. Dogra and R. G. Wilmoth, Direct simulation Monte Carlo and Navier-Stokes simulatons of blunt body wake flows, *AIAA Journal*, Vol.32, No.7, 1994.

[74] I. D. Boyd, Hybrid particle-continuum methods for nonequilibrium gas and plasma flows, *Proceedings of the 27th International Symposium on Rarefied Gas Dynamics*, In press, 2010.

[75] T. E. Schwartzentruber, L. C.Scalabrin, and I.D. Boyd, Hybrid Particle-Continuum Sim- ulations of Non-Equilibrium Hypersonic Blunt Body Flows, *AIAA paper 2006-3602*, 2006.

[76] K. Yun, R. K. Agarwal and R. Balakrishman, Hypersonic flow computations in the continuum-transition regime using the augmented Burnett and BGK-Burnett equations. *The Proceedings of the 16th International Conference on Numerical Methods in Fluid Dynamics*, Lecture Notes in Physics, Vol. 515, pp. 560 – 565, 1998.

[77] R. S. Myong, A computational method for Eu's generalized hydrodynamic equations of rarefied and microscale gasdynamics, *Journal of Computational Physics*, Vol. 168, pp. 47 – 72, 2001.

[78] G. B. Macpherson, private communication, 2010.

[79] N. T. P. Le, C. J. Greenshields and J. M. Reese, Evaluation of nonequilibrium boundary conditions for hypersonic rarefied gas flows, *Proceedings of the 3rd EUropean Conference for AeroSpace Sciences*, EUCASS2009-86, 2009.

[80] OpenFOAM User Guide, version 1.6, 2010.

[81] L. B. Loeb, The Kinetic Theory of Gases, *Dover Publications Inc., New York*, 1961.

[82] US standard atmosphere, *United States Air Force*, 1976.

[83] J. Wertz, and W. Larson, Space Mission Analysis and Design, *Microcosm Press*, 1999.

[84] D. A. Vallado, Fundamentals of Astrodynamics and Applications, *Space Technology Library, New York*, 2007.

[85] A. Marr, Internal report, *Department of Mechanical Engineering, University of Strathclyde*, 2010.